Université de Neuchâtel

Institut de Microtechnique

Polymer multilayer photonic micro- and nanostructures with tailored spectral properties

Thèse

Présentée à la faculté des sciences
pour obtenir le grade de docteur ès sciences
par

Sylvain Jaquet

Neuchâtel , septembre 2007

Université de Neuchâtel

FACULTE DES SCIENCES
Secrétariat-Décanat de la faculté
- Rue Emile-Argand 11
- CP 158
- CH-2009 Neuchâtel

IMPRIMATUR POUR LA THESE

Polymer multilayer photonic micro- and nanostructures with tailored spectral properties

Sylvain JAQUET

UNIVERSITE DE NEUCHATEL

FACULTE DES SCIENCES

La Faculté des sciences de l'Université de Neuchâtel,
sur le rapport des membres du jury

MM. H.P. Herzig (directeur de thèse),
T. Scharf, F. Flory (Marseille F) et
A. Stuck (CSEM Zürich)

autorise l'impression de la présente thèse.

Neuchâtel, le 11 octobre 2007

doyen :
T. Ward

UNIVERSITE DE NEUCHATEL
FACULTE DES SCIENCES
Secrétariat-décanat de la faculté
Rue Emile-Argand 11 - CP 158
CH-2009 Neuchâtel

■ Téléphone : +41 32 718 21 00 ■ Fax : +41 32 718 21 03 ■ E-mail : secretariat.sciences@unine.ch ■ www.unine.ch/sciences

Abstract

Amazing and beautiful optical effects are present in Nature. Some examples are the iridescent colors produced by peacocks, butterflies and beetles. While the simulations of some of these structures have already been realized, only a few elements have been fabricated. We are interested to understand and to reproduce some of these amazing optical properties. Applications such as security or decorative elements in different fields like jewelery or horology can be imagined. SEM pictures of the structure of these animals show a frequent combination of periodic or pseudo-periodic elements such as interference filters, multilayer reflectors, microlenses and gratings. The different elements combine angular and spectral effects. This combination enables strong optical effects for a large range of viewing angles and spectra. Different technologies such as standard photolithography, recording of interference patterns, transfer of photoresist structures in glass substrates, replications, hot embossing and spin-coating were used to fabricate a variety of optical elements. The fabricated elements were produced with polymer materials because of their ease of use, and the possibility to build multilevel structures with replication methods. A drawback is the small refractive index difference possible between polymers and compared to air.

In the first part, different combinations of polymer micro- and nano-optical elements such as corrugated gratings, multilayer Bragg reflectors, microlens arrays, micro-prisms arrays and diffusers were successfully fabricated. Poly(vinyl alcohol) and poly (N-vinycarbazole) with refractive indices of 1.56 and 1.72, respectively, at a wavelength of 500 nm were used to fabricate the polymer multilayer reflectors. The micro-optical elements used were: microlenses with diameter between 32 μm and 250 μm and around 20 μm height; prisms with 50 μm period and 25 μm height. The angularly dependent reflectivity of the different fabricated elements was studied. Thanks to the close combination of diffractive, refractive and reflective micro- and nano-optical elements, non-standard artificial visual color effects were produced. The fabricated elements were modeled with different tools according to the dimensions of the different optical elements. Ray tracing analysis was used in the case with micro-optical elements while the Fourier modal method permitted simulation of the interaction of the light with the periodic nano-structures. The specific effects of the variation of the different parameters were highlighted, the basic principles and the limitation of the polymer technology were identified.

In the second part, the optical modeling tools and the fabrication technologies developed were used to model and fabricate polymer light emitting diodes in a distributed feedback regime. The optical properties of the different layers were modeled and the physical dimensions of elements with active conductive polymers me-LPPP and F8 were calculated, fabricated and tested. The sensitive dimensions and parameters were underlined.

Polymer materials permitted rapid fabrication of complex and innovative optical elements with very simple technologies like spin-coating and replication methods. These technologies allow the combination of nano-optical elements with dimensions of the order of a hundred nanometers with micro-optical elements with dimension of the order of about ten to one hundred microns.

Keywords: polymer multilayer reflector, iridescent color, interference filter, replication technique, microlens array, structured OLED, polymer laser, DFB laser.

Contents

1 Introduction **9**
- 1.1 Motivation . . . 9
- 1.2 Color "production" . . . 10
- 1.3 Optical elements toolbox . . . 11

2 Theory and modeling tools **15**
- 2.1 Diffraction theory . . . 15
- 2.2 Rigorous theory: the Fourier modal method . . . 20
- 2.3 Limitations and validity of the numerical method . . . 23
- 2.4 Ray tracing . . . 24
- 2.5 Reflection spectrum and human color perception . . . 24

3 Fabrication **27**
- 3.1 Deposition of Bragg multilayer reflectors . . . 27
- 3.2 Grating fabrication . . . 28
- 3.3 Microlens fabrication . . . 30
- 3.4 Replication of micro-optics elements . . . 31
  - Replication in a UV-curing polymer . . . 31
  - Hot embossing . . . 33

4 Multilayer Bragg reflector **35**
- 4.1 Perfect Bragg reflector characteristics . . . 35
- 4.2 Measurement setup . . . 37
- 4.3 Specular reflection measurement . . . 38
- 4.4 Bragg reflector microcavity . . . 40
- 4.5 Bragg reflector with dye doped microcavity layer . . . 45

5 Resonant grating structures for visual color effects **49**
- 5.1 Introduction . . . 50
- 5.2 Principle . . . 50
- 5.3 Samples characteristics . . . 52
- 5.4 Measurement setup . . . 54
- 5.5 Observer-like optical measurement . . . 55
- 5.6 Specular reflection measurement . . . 60
- 5.7 Parameters influence on reflection in simulation . . . 64

5.8 Outlook 66

6 Interference stacks with micro-structured surfaces 67
6.1 Measurement setup 67
6.2 Characterization of the multilayer Bragg reflectors 68
6.3 Convex microlenses on multilayer Bragg reflectors 68
6.4 Concave microlenses on multilayer Bragg reflectors 78
6.5 Micro prisms on multilayer Bragg reflectors 82
6.6 Diffuser on multilayer Bragg reflectors 85

7 Organic light emitting diode on structured substrate 87
7.1 Modeling 91
7.2 Practical work 105
7.3 Optical pumping 108
7.4 Electrical pumping 115

8 Conclusion 117

Chapter 1

Introduction

1.1 Motivation

This thesis work deals principally with thin organic optical layers combined in different ways with replicated micro- and nano-optical elements. Active and passive elements were studied.

In the first part, we modeled, fabricated and characterized different passive optical elements to produce eye sensitive structural visual color effects for application in security elements. The use of these holographic security elements is well known on bank notes or credit cards, but other decorative applications in different fields like jewelery or horology can be thought. Different attempts to produce innovative and non-usual color effects by using micro- and nano-optical elements were sought. First, visual color effects have been produced by adding different microlens array to polymer multilayer Bragg reflectors. Various microlens shapes and sizes were tested. Inverted microlenses (concave microlenses) and microprism arrays were also tested (chapter 6). In the same manner, gratings with various period and height have been added on top of polymer multilayer Bragg mirror. It is known that combinations of gratings and multilayers can generate optical filters [28]. We will show that with polymers, that means with a relatively low refractive index difference, the combination of spectral reflection and grating coupling and decoupling give surprising effects (chapter 5). Based on butterfly wing structures that are well known to produce iridescent reflection, diverse structures were modeled and some of them were fabricated to produce similar color effects (chapter 5). We also inserted a thicker layer, without and with dyes, between two polymer multilayer Bragg reflectors in order to produce microcavities (chapter 4).

The second part is dedicated to active systems. We modeled, fabricated and characterized different optical elements with active layers made from photo- and electroluminescent material. We studied the different layers of an organic light emitting diode (OLED) on a grating. The goal was to find the geometrical parameters to obtain distributed feedback (DFB) operating regions (chapter 7).

1.2 Color "production"

Production of colored samples in nature can be separated in different categories, depending of the physical process involved. Generally we can separate them into two main categories. Color produced by structural effects, i.e. interference and dispersion and color produced by pigments, i.e. selective absorption. Pigment absorption of transmitted or reflected light generally do not give very pure and shiny reflected color due to large absorption spectra and diffusing properties of the pigments. The visual effect is not angular dependent [8]. The structural effects are generally largely angular dependent (observation and illumination). They can be separated in four main categories, depending on the size of the structure compared to the wavelength of the incident light:

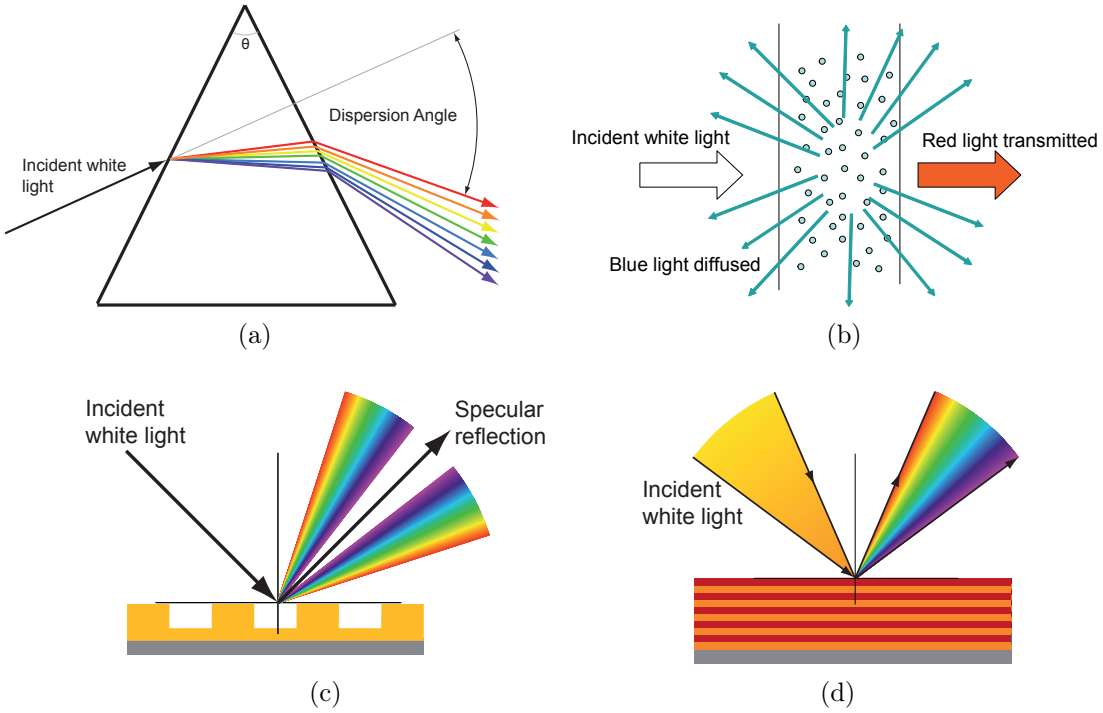

Figure 1.1: Illustration of: (a) light dispersion in a prism; (b) the effect of diffusion of light by particles with dimension less or of the order of the wavelength of the incident light; (c) the angular dependence of the dispersion of grating orders; (d) the angular dependence of reflection for a multilayer Bragg reflector.

- Refraction by structures large compared to the wavelength of the incident light. Figure 1.1(a) shows the prism effect. For small angles, the angle of the transmitted light is $\propto (n_{Prism} - n_{air}) \cdot \Theta_{Prism}$, with $n_{Prism} = n(\lambda)$ giving rise to light dispersion.

- Diffusion by particles with dimension less or of the order of the wavelength of the incident light (see Fig. 1.1(b)). The diffusion is $\propto 1/\lambda^4$, the blue light is then more diffused than the rest of the visible spectrum.

- Diffraction by a periodical structure like a grating (see Fig. 1.1(c)). The diffraction angle is $\propto m\frac{\lambda}{\Lambda}$, with Λ the period of the structure and m the grating order. The red

light is more diffracted than the rest of the visible spectrum.

- Destructive or constructive interferences by a thin layer or a multilayer stack like a multilayer Bragg reflector (see Fig. 1.1(d)).

This classification permits to explain the metallic and iridescent color of some insects [8].

1.3 Optical elements toolbox

The goal was to combine the potentially high reflectivity of multilayer Bragg reflectors, that show only specular reflection, to micro- and nano-optical elements with strong angular dispersion to get light from the sample at any angle of observation.
At our disposition were various micro-optical elements with different optical properties. Firstly, we can separate them in two categories: diffractive (grating) and refractive elements (microlenses, microprisms). A second distinction can be done concerning their spectral and angular dispersion properties. We resume these properties in Table 1.1.

Optical elements	**Angular selectivity**	**Spectral selectivity**
Grating	discrete diffraction orders	high
Bragg multilayer	specular reflection	high
Microlens	refraction in a range of angles	low
Microprim	refraction in a single angle	low

Table 1.1: Angular and spectral selectivity of the different micro-optical elements used in this work.

One can imagine to fabricate elements with various combinations giving rise to optical effects. Figure 1.8 gives an overview of the combinations that might be useful and were therefore studied in this work. Some of them have been already fabricated with other technology and have found various applications in optics, for example for high resolution optical filters by combining multilayer and grating [28].

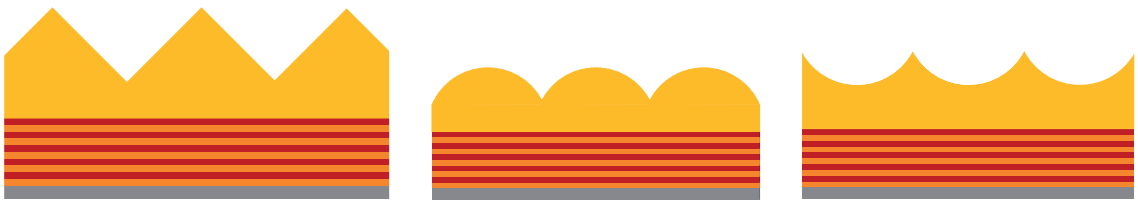

(a) (b) (c)

Figure 1.2: Illustrations of optical elements combining a multilayer polymer Bragg reflector with different replicated microstructures such: (a) a microprism array; (b) a microlens array; (c) a concave microlens array.

We first thought to combine a multilayer polymer Bragg reflector with different refractive microstructures on top. Figure 1.2 illustrates microprism arrays, microlenses and concave microlenses replicated on top of the multilayer structure. In these case, we can adjust different

parameters such as microlenses diameter and curvature, but also the reflection wavelength and efficiency of the multilayer Bragg mirror. As illustrated in Fig. 1.3, we also imagined to have the polymer multilayer Bragg reflector on top of the microstructures, i.e. a reflector or a filter coated directly on the micro-optical element. This gives potentially reflection at very

(a) (b)

Figure 1.3: Illustration of a multilayer reflector coated on: (a) a microlens array, (b) a concave microlens array.

large angles for microlenses. For a multilayer structure deposited on concave microlenses, the reflection can also give rise to some polarization effects. Depending where the light is reflected inside the concave structure, if the angle of incidence is close to the Brewster angle, one can observe a selective reflection. Since a spin coating technique was used to form the layers of the Bragg mirror, it was difficult to fabricate such a sample with large number of layers with this technology.

The second idea was a combination of a multilayer Bragg reflector and a corrugated grating.

(a) (b)

Figure 1.4: Illustrations of a combination of a multilayer Bragg reflector and a corrugated grating with: (a) a thick layer between grating and multilayer; (b) a thin layer between grating and multilayer.

This gives a lot of different possible samples. We restricted our efforts on replicated grating on top of a Bragg mirror (see Fig. 1.4). Here one can play with different parameters, such as the grating period to control the number of diffraction orders, the grating depth for the diffraction efficiency and also the thickness of the layer (waveguide) between grating and Bragg mirror that will give rise to some interference in the reflection. Other possibilities to combine a multilayer Bragg reflector and a corrugated grating can be reached by hot embossing the multilayer reflector with a grating pattern or etching the grating in the multilayer reflector. These combinations are illustrated in Figs. 1.5(a) and 1.5(b), respectively.

An alternative that combines multilayer reflectors and gratings has been reported in [14], giving the so called Aztec structures because the structure looks like an Aztec pyramid. Such a structure is illustrated in Fig. 1.6(a). The same fabrication technique could give rise to a structure illustrated in Fig. 1.6(b) similar to the famous structure of the Morpho Butterfly

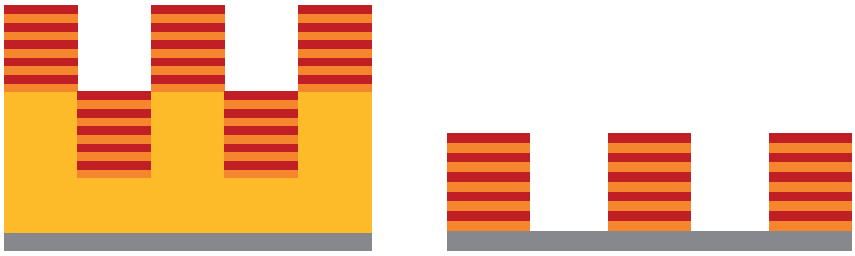

(a) (b)

Figure 1.5: Illustration of a combination of a multilayer Bragg reflector and a corrugated grating. (a) The grating is etched inside the multilayer reflector. (b) The grating shape is embossed inside the multilayer structure.

that is known to have high reflection efficiency for a selected part of the visible and a wide range of incident angle [8].

(a) (b)

Figure 1.6: (a) Illustration of a combination of a reflector and grating that has been reported in [14], giving the so called Aztec structures since the structure looks like an Aztec pyramid .(b) An equivalent fabrication technique can produce structure similar to the famous structure of the Morpho Butterfly. This structure is known to have high reflection efficiency for a selected part of the visible and a wide range of incident angle [8].

Finally, a planar waveguide with thickness $d = (\lambda/2n)$ for a single optical mode or $d > (\lambda/2n)$ for multiple modes can used in different configuration. Inserted between two Bragg reflector, one creates a microcavity. Such a structure is illustrated in Fig. 1.7. It changes the global reflection properties from the perfectly periodic multilayer structure. With an active waveguide, this structure can produce a distributed Bragg reflector laser (DBR).

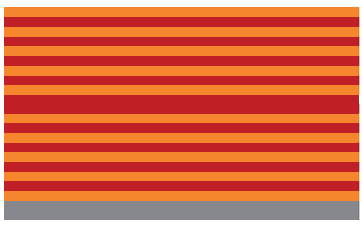

Figure 1.7: A waveguide is inserted between two Bragg reflector and create a microcavity. The reflection properties of the multilayer Bragg mirror are modified.

To resume, the different element are classified in Table 1.8.

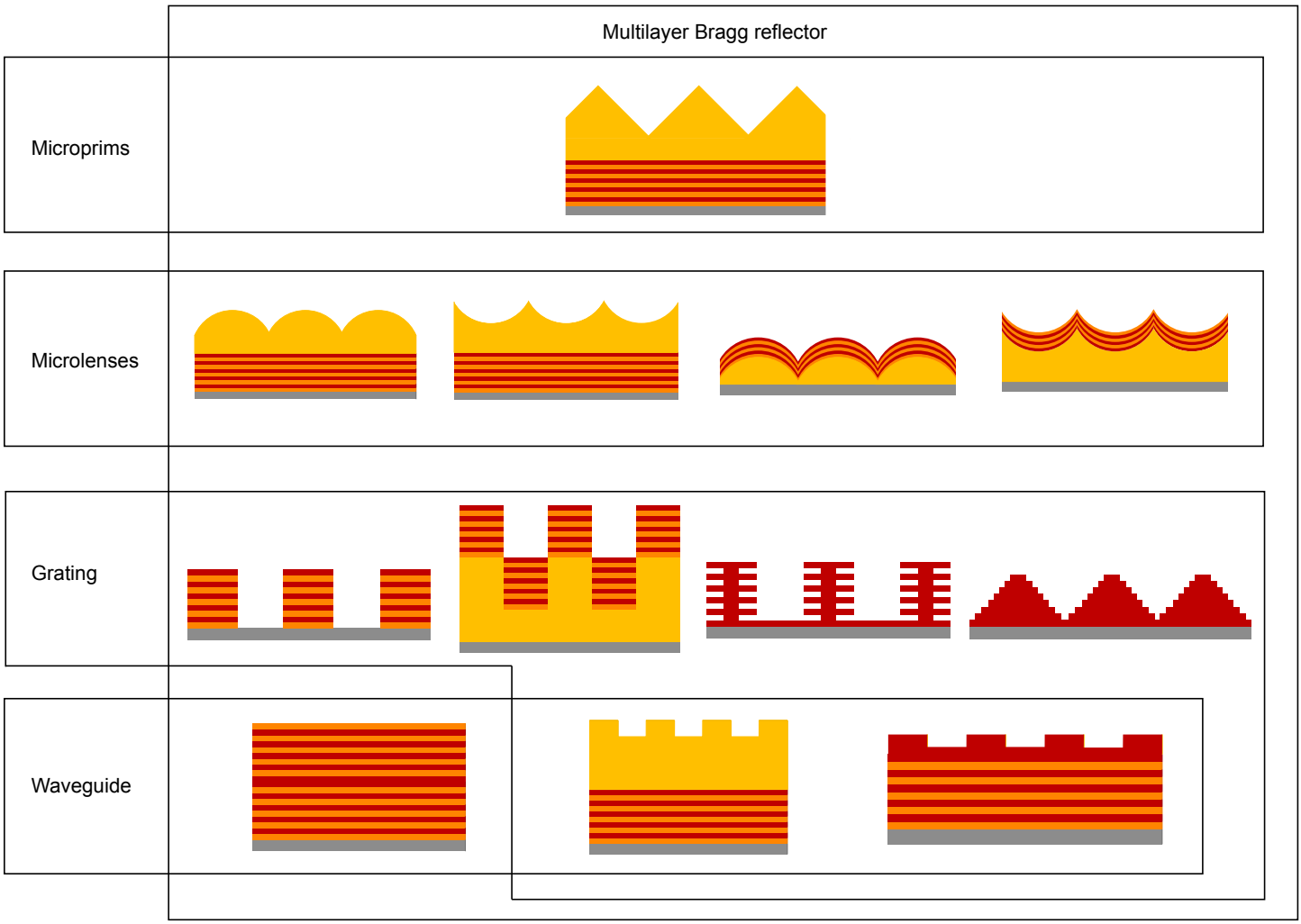

Figure 1.8: Schematic overview of the studied samples that combine multilayer Bragg reflector, microprisms, microlenses, gratings and waveguides.

Chapter 2

Theory and modeling tools

In this chapter, the different modeling methods used in this work will be presented. Due to the different size scales of the optical elements treated, the modeling tools had to be adapted for each case. For micro-optical elements (microlenses, microprisms, etc.), with typical dimensions from 20 to 200 μm, a ray tracing method has been used and diffractive effects are neglected. For periodic gratings, with typical size between some hundreds of nanometers to 1.5 microns, that means of the order of the wavelength of the light, an exact electromagnetic numerical method was used.
A short reminder of basic electromagnetic theory is shown. The textbooks [48] and [50] were used as reference books in electromagnetic theory applied to optics. A brief description of the exact electromagnetic numerical method used is also given. A complete description of this method can be found in the literature [25, 44]. The references [44] and [10], written by a former member of the group, were used as an outline to write this theoretical part.

2.1 Diffraction theory

The Maxwell equations describe the behavior of electromagnetic fields and their interactions with matter.

$$\boldsymbol{\nabla} \times \mathbf{E} + \frac{\partial \mathbf{B}}{\partial t} = 0 \tag{2.1}$$

$$\boldsymbol{\nabla} \times \mathbf{H} - \frac{\partial \mathbf{D}}{\partial t} = \mathbf{j} \tag{2.2}$$

$$\boldsymbol{\nabla} \cdot \mathbf{D} = \rho \tag{2.3}$$

$$\boldsymbol{\nabla} \cdot \mathbf{B} = 0 \tag{2.4}$$

with $\mathbf{E}$ being the electric field (in volts per meter) and $\mathbf{H}$ the magnetic field (in amperes per meter). $\mathbf{D}$ and $\mathbf{B}$ are the electric displacement (in coulombs per square meter) and magnetic induction (in webers per square meter), respectively. These quantities are introduced to take into account the effect between matter and the electromagnetic field. ρ and $\mathbf{j}$ are the electric charge density (coulombs per cubic meter) and the electric current density (in amperes per

square meter), respectively.
The constitutive equations (or material equations) are given by

$$\mathbf{D} = \epsilon\,\mathbf{E} = \epsilon_0\,\mathbf{E} + \mathbf{P} \tag{2.5}$$

and

$$\mathbf{B} = \mu\,\mathbf{H} = \mu_0\,\mathbf{H} + \mathbf{M} \tag{2.6}$$

with ϵ being the electric permittivity and μ the magnetic permeability. $\mathbf{P}$ and $\mathbf{M}$ are the electric and magnetic polarizations, respectively.
The constant $\epsilon_0 = 8.854 \cdot 10^{-12}\,As/Vm$ is the permittivity of the vacuum and $\mu_0 = 4\pi \cdot 10^{-7}\,Vs/Am$ the permeability of the vacuum. At interface discontinuities, the field properties are described by the following equations, called boundary conditions:

$$\mathbf{n}_{12} \cdot (\mathbf{D}_2 - \mathbf{D}_1) = \rho_S \tag{2.7}$$

$$\mathbf{n}_{12} \times (\mathbf{H}_2 - \mathbf{H}_1) = \mathbf{j}_S \tag{2.8}$$

$$\mathbf{n}_{12} \times (\mathbf{E}_2 - \mathbf{E}_1) = 0 \tag{2.9}$$

$$\mathbf{n}_{12} \cdot (\mathbf{B}_2 - \mathbf{B}_1) = 0 \tag{2.10}$$

with $\mathbf{n}_{12}$ a unit normal vector to the interface between the two regions. These continuity equations are directly derived from the Maxwell equations. The continuity for $\mathbf{B}$ and $\mathbf{D}$ are found by applying the Gauss divergence theorem to Eqs. (2.3) and (2.4). The integration volume is a small cylinder placed at the interface, with faces parallel to the surface. The result is that the normal component of the magnetic induction is always continuous and the difference between the normal components of the electric displacement is equal to the surface charge density. For $\mathbf{E}$ and $\mathbf{H}$, the Stokes theorem is applied to Eqs. (2.1) and (2.2). The integration contour is a small rectangle with long side parallel to the surface of discontinuity. The result is that the tangential component of the electric field is always continuous and the difference between the tangential components of the magnetic field is equal to the surface current density. In our study, only dielectric materials are considered. The electric current density $\mathbf{j}$ and the electric charge density ρ are then equal to zero, and the boundary conditions are simplified. The normal components of $\mathbf{B}$ and $\mathbf{D}$ and tangential component of $\mathbf{E}$ and $\mathbf{H}$ are continuous at the interface separating the two media. The next step is to decouple the contribution of $\mathbf{E}$ and $\mathbf{H}$ in Maxwell equations. Here we limit the study to the case of an isotropic medium, meaning that μ and ϵ are scalar (tensors in the general case). We apply the curl operator to Eq. (2.1) and use Eq. (2.6) for $\mathbf{B}$. We get

$$\boldsymbol{\nabla} \times \left(\frac{1}{\mu} \boldsymbol{\nabla} \times \mathbf{E} \right) + \frac{\partial}{\partial t} \boldsymbol{\nabla} \times \mathbf{H} = 0. \tag{2.11}$$

If we differentiate Eq. (2.2) with respect to time, replace in Eq. (2.11) and use Eq. (2.5) for **D**, one obtains

$$\boldsymbol{\nabla} \times \left(\frac{1}{\mu} \boldsymbol{\nabla} \times \mathbf{E} \right) + \epsilon \frac{\partial^2 \mathbf{E}}{\partial t^2} = 0 \tag{2.12}$$

By using the following vector identities

$$\boldsymbol{\nabla} \times \left(\frac{1}{\mu} \boldsymbol{\nabla} \times \mathbf{E} \right) = \frac{1}{\mu} \boldsymbol{\nabla} \times (\boldsymbol{\nabla} \times \mathbf{E}) + \left(\boldsymbol{\nabla} \frac{1}{\mu} \right) \times (\boldsymbol{\nabla} \times \mathbf{E}) \tag{2.13}$$

and

$$\boldsymbol{\nabla} \times (\boldsymbol{\nabla} \times \mathbf{E}) = \boldsymbol{\nabla}(\boldsymbol{\nabla} \cdot \mathbf{E}) - \boldsymbol{\nabla}^2 \mathbf{E} \tag{2.14}$$

Eq. (2.12) becomes

$$\boldsymbol{\nabla}^2 \mathbf{E} - \mu \epsilon \frac{\partial^2 \mathbf{E}}{\partial t^2} + \left(\frac{\boldsymbol{\nabla} \mu}{\mu} \right) \times (\boldsymbol{\nabla} \times \mathbf{E}) - \boldsymbol{\nabla}(\boldsymbol{\nabla} \cdot \mathbf{E}) = 0. \tag{2.15}$$

We use again Eq. (2.5) for **D** in Eq. (2.3), and the vector identity

$$\boldsymbol{\nabla} \cdot (\epsilon \, \mathbf{E}) = \epsilon \, \boldsymbol{\nabla} \cdot \mathbf{E} + \mathbf{E} \cdot \boldsymbol{\nabla} \, \epsilon. \tag{2.16}$$

Finally Eq. (2.15) becomes

$$\boldsymbol{\nabla}^2 \mathbf{E} - \mu \epsilon \frac{\partial^2 \mathbf{E}}{\partial t^2} + \left(\frac{\boldsymbol{\nabla} \mu}{\mu} \right) \times (\boldsymbol{\nabla} \times \mathbf{E}) + \boldsymbol{\nabla} \left(\mathbf{E} \cdot \frac{\boldsymbol{\nabla} \epsilon}{\epsilon} \right) = 0. \tag{2.17}$$

This is the wave equation for **E**. The wave equation for **H** is obtained in a similar way and is

$$\boldsymbol{\nabla}^2 \mathbf{H} - \mu \epsilon \frac{\partial^2 \mathbf{H}}{\partial t^2} + \left(\frac{\boldsymbol{\nabla} \epsilon}{\epsilon} \right) \times (\boldsymbol{\nabla} \times \mathbf{H}) + \boldsymbol{\nabla} \left(\mathbf{H} \cdot \frac{\boldsymbol{\nabla} \mu}{\mu} \right) = 0. \tag{2.18}$$

For non-magnetic media (the magnetic permeability μ is always equal to μ_0), we obtain the two inhomogeneous wave equations for **E** and **H**

$$\boldsymbol{\nabla}^2 \mathbf{E} - \mu \epsilon \frac{\partial^2 \mathbf{E}}{\partial t^2} + \boldsymbol{\nabla} \left(\mathbf{E} \cdot \frac{\boldsymbol{\nabla} \epsilon}{\epsilon} \right) = 0 \tag{2.19}$$

$$\boldsymbol{\nabla}^2 \mathbf{H} - \mu \epsilon \frac{\partial^2 \mathbf{H}}{\partial t^2} + \left(\frac{\boldsymbol{\nabla} \epsilon}{\epsilon} \right) \times (\boldsymbol{\nabla} \times \mathbf{H}) = 0. \tag{2.20}$$

In homogeneous (permittivity is constant throughout the region of propagation) and isotropic (properties are independent of the direction of polarization of the wave) media, these equations reduce to the standard electromagnetic wave equations

$$\boldsymbol{\nabla}^2 \mathbf{E} - \mu \epsilon \frac{\partial^2 \mathbf{E}}{\partial t^2} = 0 \tag{2.21}$$

$$\boldsymbol{\nabla}^2\mathbf{H} - \mu\,\epsilon\,\frac{\partial^2\mathbf{H}}{\partial t^2} = 0. \tag{2.22}$$

The goal of this optical modeling is to know the optical response, i.e. the intensity of reflection or transmission of an optical element when illuminated by a light source with a given wavelength. Therefore, in the following calculation, we will use time harmonic electromagnetic fields of angular frequency ω, with electric and magnetic field expressed in the complex representation as

$$\mathbf{E}(\mathbf{r},t) = Re\left\{\mathbf{E}(\mathbf{r})e^{-i\omega t}\right\} \tag{2.23}$$

and

$$\mathbf{H}(\mathbf{r},t) = Re\left\{\mathbf{H}(\mathbf{r})e^{-i\omega t}\right\}. \tag{2.24}$$

With this notation, the first two Maxwell equations (Eqs. (2.1) and (2.2)) are

$$\boldsymbol{\nabla}\times\mathbf{E}(\mathbf{r}) = -i\omega\,\mu\,\mathbf{H}(\mathbf{r}) \tag{2.25}$$

$$\boldsymbol{\nabla}\times\mathbf{H}(\mathbf{r}) = i\omega\,\epsilon\,\mathbf{E}(\mathbf{r}). \tag{2.26}$$

For 2D geometry, the inhomogeneous wave equations for $\mathbf{E}$ and $\mathbf{H}$ (Eqs.(2.19) and (2.20)) are reduced to simpler equations. Here, 2D geometry means that the media and the field do not vary in the y-direction and that the waves are propagating in the x-z plane (see Fig. 2.1). In this case, all the partial derivatives in the y-direction are equal to zero. The calculation for TE-polarization (E_y) and TM-polarization (H_y) are done in detail in [44] and give

$$\frac{\partial^2}{\partial x^2}\,E_y(x,z) + \frac{\partial^2}{\partial z^2}\,E_y(x,z) + \epsilon_r(x,z)k^2\,E_y(x,z) = 0 \tag{2.27}$$

$$\frac{\partial}{\partial x}\left[\frac{1}{\epsilon_r(x,z)}\,\frac{\partial}{\partial x}\,H_y(x,z)\right] + \frac{\partial}{\partial z}\left[\frac{1}{\epsilon_r(x,z)}\,\frac{\partial}{\partial z}H_y(x,z)\right] + k^2\,H_y(x,z) = 0. \tag{2.28}$$

The complex relative permittivity is $\epsilon_r(x,z)$, and the complex refractive index is defined as

$$\epsilon_r(x,z) = [n(x,z)]^2 = \frac{\epsilon(x,z)}{\epsilon_0} + i\frac{\sigma(x,z)}{\omega\,\epsilon_0} \tag{2.29}$$

with the conductivity σ, the wave number $k = \omega/c$ and the speed of the light in vacuum $c = (\epsilon_0\mu_0)^{-1/2}$. The imaginary part of the complex refractive index will represent the absorption of the field by a conducting material. The structure to be solved is illustrated in Fig. 2.1. The structure is separated into three regions. Two semi-infinite homogeneous region (regions I and III) with permittivity ϵ_I and ϵ_{III} describing the incident region and the outcoupling region, respectively. The periodic surface modulation is described in the inhomogeneous region II.

The field in region S_I is the sum of the incident field E_0 and reflected field E_r. The field in region S_{III} is the transmitted field

$$E_I(\mathbf{r}) = E_o(\mathbf{r}) + E_r(\mathbf{r}),\ \text{and}\quad E_{III}(\mathbf{r}) = E_t(\mathbf{r}). \tag{2.30}$$

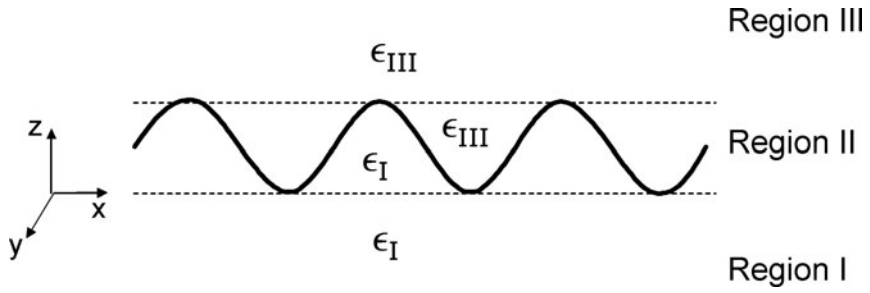

Figure 2.1: The three regions in the diffraction problem.

If we take a plane wave in the x-z plane for the incident field,

$$E_o = \exp(in_I \mathbf{k}\cdot\mathbf{r}) = \exp\left[ikn_I(x\sin\theta + z\cos\theta)\right] = \exp(i\alpha_0 x + i\beta_0 z) \tag{2.31}$$

with the angle of incidence θ. The form of the reflected $E_r(\mathbf{r})$ and transmitted field $E_t(\mathbf{r})$ will be periodic since the modulation in the inhomogeneous region is periodic in the x-direction and therefore can be written in a Fourier series

$$E_r(\mathbf{r}) = \exp(i\alpha_0 x)\sum_n v_n(z)\exp(-inKx) = \sum_n v_n(z)\exp(i\alpha_n x) \tag{2.32}$$

$$E_t(\mathbf{r}) = \exp(i\alpha_0 x)\sum_n w_n(z)\exp(-inKx) = \sum_n w_n(z)\exp(i\alpha_n x). \tag{2.33}$$

with the grating vector $\mathbf{K}$ oriented perpendicular to the grating grooves, and having length

$$K = \frac{2\pi}{\Lambda} \tag{2.34}$$

and α_n defined as

$$\alpha_n = \alpha_0 - nK. \tag{2.35}$$

If we insert Eqs. (2.32) and (2.33) in the Helmholtz Eq. (2.27), we have

$$\frac{\partial^2 v_n}{\partial z^2} + (k^2\epsilon_I - \alpha_n^2)v_n = 0, \text{ and } \quad \frac{\partial^2 w_n}{\partial z^2} + (k^2\epsilon_{III} - \alpha_n^2)w_n = 0. \tag{2.36}$$

The general mathematical solutions are

$$v_n(z) = A_n\exp(i\,\beta_{1,n}\,z) + B_n\exp(-i\,\beta_{1,n}\,z), \text{ with } \quad \beta_{1,n} = \sqrt{k^2\,\epsilon_I - \alpha_n^2} \tag{2.37}$$

$$w_n(z) = C_n\exp(i\,\beta_{3,n}\,z) + D_n\exp(-i\,\beta_{3,n}\,z), \text{ with } \quad \beta_{3,n} = \sqrt{k^2\,\epsilon_{III} - \alpha_n^2}. \tag{2.38}$$

The physical solution involves $A_n = 0$ and $D_n = 0\ \forall\, n$ since the reflected and transmitted fields consist only of backward traveling wave and forward traveling waves, respectively. Finally we obtain the Rayleigh expansion (superposition of plane waves) of the reflected and transmitted field

$$E_r(\mathbf{r}) = \sum_n R_n\exp(i\alpha_n\,x - i\beta_{1,n}\,z) \qquad \text{for Region I} \tag{2.39}$$

$$E_t(\mathbf{r}) = \sum_n T_n\exp(i\alpha_n\,x + i\beta_{3,n}\,z) \qquad \text{for Region III} \tag{2.40}$$

Solving the diffraction problem illustrated in Fig. 2.1 means to find the complex amplitudes R_n and T_n.

2.2 Rigorous theory: the Fourier modal method

This theoretical part follows the development of Turunen [44]. The next step to solve the diffraction problem is to remove the z-dependence of the permittivity $\epsilon(x, z)$. To do this, as illustrated in Figs. 2.2(a) and 2.2(b), the region II is divided into a stack of thin lamellar layers with a fixed value of the permittivity $\epsilon(x)$ for any given layer. This binary permittivity functions will be expanded in Fourier series. For sake of simplicity, the following description

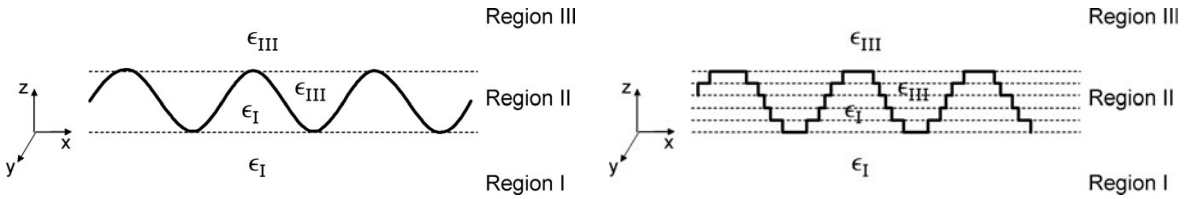

Figure 2.2: (a) The three regions in the diffraction problem. The region S_{II} contains the periodic variation of the permittivity $\epsilon(x, z)$. (b) The region S_{II} is divided into a stack of thin lamellar layers with a fixed value of the permittivity $\epsilon(x)$. The z-dependence of the permittivity is removed.

is done for only one layer. For this z-invariant case, one can solve the system with an eigenmode theory. For the TE-mode, the following separation of variables is introduced in the Helmholtz equation

$$E(x, z) = X(x)Z(z). \tag{2.41}$$

This gives two ordinary differential equations

$$\frac{d^2}{dx^2}X(x) + \left[k^2\epsilon(x) - \gamma^2\right]X(x) = 0 \tag{2.42}$$

$$\frac{d^2}{dx^2}Z(z) + \gamma^2 Z(z) = 0 \tag{2.43}$$

where γ^2 is a separation constant. The solution of Eq. (2.43) is

$$Z(z) = a\exp(i\gamma z) + b\exp\left[-i\gamma(z-h)\right]. \tag{2.44}$$

To solve Eq. (2.42), the Fourier series of the complex relative permittivity is introduced

$$\epsilon_r(x) = \sum_{p=-\infty}^{\infty} \epsilon_p \exp\left(\frac{i\,2\pi\,p\,x}{\Lambda}\right). \tag{2.45}$$

The Floquet-Bloch theorem states that since the refractive index is periodic, the solution will be pseudo-periodic and have the form

$$X(x) = \sum_{m=-\infty}^{\infty} P_m \exp(i\alpha_m x), \quad \text{with} \quad \alpha_m = \alpha_0 + m\frac{2\pi}{\Lambda}, \quad \text{and} \quad \alpha_0 = kn\sin(\theta). \tag{2.46}$$

If the solution for $X(x)$ given in Eq. (2.46) and the Fourier series of the complex relative permittivity given in Eq. 2.45 are introduced in Eq. (2.42), one obtains

$$\sum_{m=-\infty}^{\infty}\sum_{p=-\infty}^{\infty}\left[(\alpha_m^2+\gamma^2)\exp(i\alpha_p\,x)\delta_{mp}-k^2\epsilon_p\exp(i\alpha_{m+p}\,x)\right]P_m=0. \tag{2.47}$$

Multiplication with $\exp(-i\alpha_l\,x)$ and integration over the period Λ gives a system of equations (index l)

$$\sum_{m=-\infty}^{\infty}\left(k^2\epsilon_{l-m}-\alpha_m^2\delta_{lm}\right)P_m=\gamma^2P_l, \qquad \text{or} \quad \mathbf{M}\cdot\mathbf{P}=\gamma^2\mathbf{P} \tag{2.48}$$

with the coefficients of the matrix M given by

$$M_{lm}=k^2\epsilon_{l-m}-\alpha_m^2\delta_{lm}. \tag{2.49}$$

The eigenvalues γ_n and corresponding eigenvectors $\mathbf{P_n}$ can be found by solving this system of linear equations. Finally, the complete solution of the Helmholtz equations is

$$E_y(x,z)=\sum_{l=-\infty}^{\infty}\sum_{n=0}^{\infty}P_{ln}\exp(i\alpha_l x)\{a_n\exp(i\gamma_n z)+b_n\exp\left[-i\gamma_n(z-h)\right]\}. \tag{2.50}$$

For the TM polarization, the procedure is similar and here again we test a pseudo-periodic solution

$$H_y(x,z)=\{a\exp(i\gamma z)+b\exp[-i\gamma(z-h)]\}\sum_{m=-\infty}^{\infty}P_m\exp(i\alpha_m x). \tag{2.51}$$

This time, the permittivity is in the denominator in the Helmoltz equation (2.28). For this reason, the Fourier series of the inverse of the complex relative permittivity is introduced

$$\frac{1}{\epsilon_r(x)}=\sum_{p=-\infty}^{\infty}\xi_p\exp\left(\frac{i\,2\pi\,p\,x}{\Lambda}\right). \tag{2.52}$$

An equivalent eigenvalue equation for the TM polarization is obtained by introducing Eqs. (2.52) and (2.51) in the Helmoltz equation (2.28). To get a more convenient eigenvalue equation, the following function (Eq. (2.53)) and its pseudo-periodic expansion (Eq. (2.54)) are introduced

$$Q(x,z)=\frac{1}{\epsilon_r(x)}\frac{\partial}{\partial z}H_y(x,z) \tag{2.53}$$

$$Q(x,z)=i\gamma\left\{a\exp(i\gamma z)-b\exp\left[-i\gamma(z-h)\right]\right\}\sum_{m=-\infty}^{\infty}Q_m\exp(i\alpha_m x). \tag{2.54}$$

If we multiply Eq. (2.53) by $\epsilon_r(x)$ and insert the pseudo-periodic expansions for $\epsilon_r(x)$, $H_y(x,z)$ and $Q(x,z)$ (Eqs. (2.45), (2.51) and (2.54), respectively), one obtains

$$P_l=\sum_{m=-\infty}^{\infty}\epsilon_{l-m}Q_m. \tag{2.55}$$

If we place Eq. (2.53) in Helmholtz equation for $H_y(x,z)$, i.e Eq. (2.28), we obtain

$$\frac{\partial}{\partial x}\left[\frac{1}{\epsilon_r(x)}\frac{\partial}{\partial x}H_y(x,z)\right]+\frac{\partial}{\partial z}Q(x,z)k^2H_y(x,z)=0. \tag{2.56}$$

And finally after inserting Eqs. (2.51), (2.52) and (2.54), we obtain

$$\sum_{m=-\infty}^{\infty}\left(k^2\delta_{lm}-\alpha_l\xi_{l-m}\alpha_m P_m\right)=\gamma^2 Q_l. \tag{2.57}$$

In matrix form, Eqs. (2.55) and (2.57) are

$$\mathbf{NQ}=\mathbf{P} \tag{2.58}$$

$$\mathbf{MP}=\gamma^2\mathbf{Q}. \tag{2.59}$$

With the matrix element of $\mathbf{N}$ and $\mathbf{M}$ are $N_{lm}=\epsilon_{l-m}$ and $M_{lm}=k^2\delta_{lm}-\alpha_l\xi_{l-m}\alpha_m$. Finally Eq.(2.60) allows us to find the eigenvalues γ_n and the eigenvector elements Q_{ln}.

$$\mathbf{MNQ}=\gamma^2\mathbf{Q}. \tag{2.60}$$

The eigenvectors elements P_{ln} can be found with Eq. (2.58).
The fields in the three regions have been derived but the field amplitudes of the Rayleigh expansion R_m, T_m, and the amplitudes of the modes inside each layer a_n and b_n of Eqs. (2.39) and (2.40) must be solved using the boundary conditions (Eqs. (2.10), (2.7), (2.9) and (2.8)) at $z=0$ and $z=h$. For the TE polarization, the tangential part of the field must be continuous at the interface. Thus E_y is continuous at the boundaries. At the interface $z=0$, the sum of the incident (2.31) and reflected field (2.39) must be equal to the field inside of the modulated region (2.50)

$$\delta_{l0}+R_l=\sum_{m=1}^{\infty}\left[a_m+b_m\exp(i\gamma_m h)\right]P_{lm}, \qquad l=-\infty,...,\infty. \tag{2.61}$$

At the interface $z=h$, the field inside of the modulated region, given by Eq. (2.50) must be equal to the transmitted field, Eq. (2.40)

$$T_l=\sum_{m=1}^{\infty}\left[a_m\exp(i\gamma_m h)+b_m\right]P_{lm}. \tag{2.62}$$

For TM polarization, the Eqs. (2.8) and (2.25) require that H_y and the derivative $\partial\, E_y(x,z)/\partial z$ must also be continuous at the interface. For $z=0$

$$r_l(\delta_{l0}+R_l)=\sum_{m=1}^{\infty}\gamma_m\left[a_m-b_m\exp(i\gamma_m h)\right]P_{lm}, \qquad l=-\infty,...,\infty \tag{2.63}$$

and for $z=h$

$$t_l T_l=\sum_{m=1}^{\infty}\gamma_m\left[a_m\exp(i\gamma_m h)-b_m\right]P_{lm}. \tag{2.64}$$

If we replace R_l and T_l from Eqs. (2.61) and (2.62) into Eqs. (2.63) and (2.64), we obtain two equations

$$\sum_{m=1}^{\infty}(r_l+\gamma_m)P_{lm}a_m+\sum_{m=1}^{\infty}(r_l-\gamma_m)\exp(i\gamma_m h)P_{lm}b_m=2r_l\delta_{l0} \tag{2.65}$$

$$\sum_{m=1}^{\infty}(t_l-\gamma_m)\exp(i\gamma_m h)P_{lm}a_m+\sum_{m=1}^{\infty}(t_l+\gamma_m)P_{lm}b_m=0. \tag{2.66}$$

These two equations can be solved to find the values $\{a_n\}$ and $\{b_n\}$. By inserting these solutions in Eqs. (2.61) and (2.62), one obtains the values for R_l and T_l. For TM polarization, the procedure is similar. The continuity of H_y at the interfaces $z=0$ and $z=h$ is given by Eq. (2.8) since in this case the current density $\mathbf{j}=0$. The continuity of E_x and $\partial/\partial z\, H_y(x,z)$ and therefore of the function $Q(x,z)$ Eq. (2.53) is given by Eq. (2.9) and (2.26). With these conditions, one obtains the following equations

$$\sum_{m=1}^{\infty}(n_I^{-2}r_lP_{lm}+\gamma_mQ_{lm})a_m+\sum_{m=1}^{\infty}(n_I^{-2}r_lP_{lm}-\gamma_mQ_{lm})\exp(i\gamma_m h)b_m=2n_I^{-2}r_l\delta_{l0} \tag{2.67}$$

$$\sum_{m=1}^{\infty}(n_{III}^{-2}t_lP_{lm}-\gamma_mQ_{lm})\exp(i\gamma_m h)a_m+\sum_{m=1}^{\infty}(n_{III}^{-2}t_lP_{lm}+\gamma_mQ_{lm})b_m=0. \tag{2.68}$$

The general case with the modulated region sliced in more than one layer can be solved by applying the boundary conditions at each interface. Equations are given in [44]

2.3 Limitations and validity of the numerical method

The Fourier modal method can be used to solve all kinds of periodic surface relief structures. Here the 2D method was described but a 3D method, useful for crossed gratings, also exists [22]. Nevertheless, like in every numerical simulation, the validity of the results must be carefully verified before conclusions can be drawn. The description of the FMM can be resumed in finding the solutions of an eigenvalue problem and of the boundary value problem. That was described including infinite matrices and vectors. In numerical calculation, these matrices and vectors must be truncated to a size allowing stable results and in order to limit the calculation time. When doing so, we retain a finite number of terms in the series describing the fields and the dielectric grating refractive index variations. If N Rayleigh orders are used (hence N lowest order eigenmodes of the modulated structure) the eigenvalue matrix has dimension of $N\times N$. The corresponding dimension of the boundary value matrix is $2N\times 2N$ for one layer. For Q-layers, the dimension is $2N(Q+1)\times 2N(Q+1)$. The number of layers that represent the surface relief is not only important in the size of matrix and the calculation time but also for the accuracy of the result. The individual layers must have a thickness several time thinner than the incident wavelength in order not to introduce additional effects. A simple example can be see in [14]. Here a traditional sinusoidal grating modeled with slice thickness of the order of a quarter of the wavelength can produce strong reflecting effects. A general method to verify the accuracy of the calculation is the following.

First of all, we must keep all the propagating Rayleigh orders. In addition, one must take a number of evanescent orders to reach accurate results. To do this, one increases progressively the number of orders and observes the convergence of the diffraction efficiency of the different reflected and transmitted orders.

2.4 Ray tracing

To model a system combining a Bragg reflector and micro-optical elements, we used TracePro (Lambda Research), a commercial Ray tracing software. This software allows the possibility to introduce surface properties like a multilayer Bragg mirror or various coatings. As the rays propagate along different paths throughout the solid model, TracePro keeps track of the optical flux associated with each ray [21]. It accounts for the absorption, specular reflection and refraction, diffraction and scattering of light. Useful references for an introduction and further reading on ray tracing simulations can be found in [16, 21, 43].

2.5 Reflection spectrum and human color perception

The optical measurement of a sample gives the spectral reflection efficiency. We are interested in converting the reflection spectrum human color perception, i.e. to know which color will be perceived for given illumination conditions and sample reflection spectrum. The perception of color will be determined by the illumination condition (angle and spectrum of illumination) and by the observer conditions (angle of view, acceptance angle). For converting reflectivity $R(\lambda, \Theta)$ into color-map, we use the CIE normalization (Commission Internationale de l'éclairage [2]). The normalized illuminant D65 [1] that fits the daylight sky spectrum is used as the light source (see Fig. 2.3(a)). The CIE 1931 spectral tristimulus

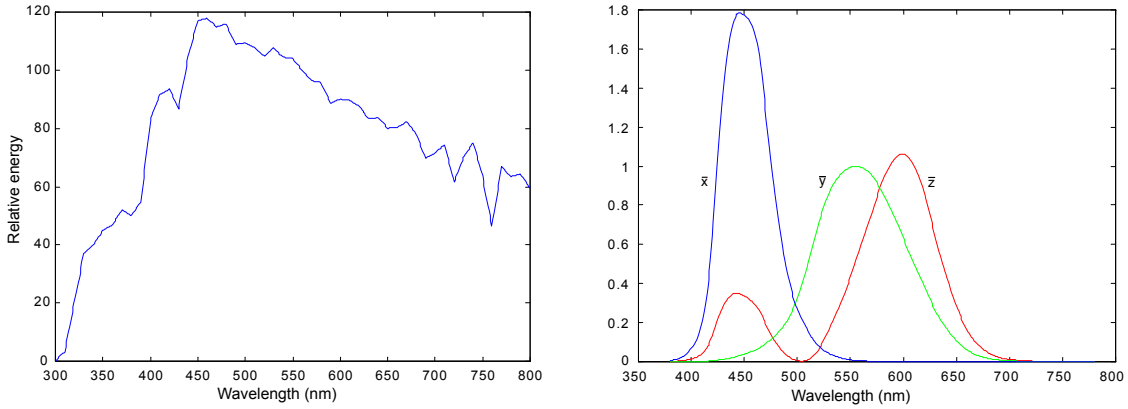

(a) (b)

Figure 2.3: (a) Relative energy distribution $D(\lambda)$ of the CIE D65 illuminant, (b) $\bar{x}$, $\bar{y}$ and $\bar{z}$ spectral tristimulus values.

functions $\bar{x}$, $\bar{y}$, $\bar{z}$ (see Fig. 2.3(b)) are used to convert the reflectivity spectrum $R(\lambda)$ into

X,Y and Z tristimulus coordinates according to Eqs. (2.69) to (2.71):

$$X = \frac{1}{k}\int D(\lambda)R(\lambda)\bar{x}d\lambda \tag{2.69}$$

$$Y = \frac{1}{k}\int D(\lambda)R(\lambda)\bar{y}d\lambda \tag{2.70}$$

$$Z = \frac{1}{k}\int D(\lambda)R(\lambda)\bar{z}d\lambda \tag{2.71}$$

with k a normalization coefficient determined by the condition $Y = 1$ (luminance) for reflectivity $R(\lambda) = 1,\ \forall\lambda$

$$k = \int D(\lambda)\bar{y}d\lambda. \tag{2.72}$$

The values X, Y and Z are then normalized to obtain the values x, y and z,

$$x = \frac{X}{X+Y+Z} \tag{2.73}$$

$$y = \frac{Y}{X+Y+Z} \tag{2.74}$$

$$z = \frac{Z}{X+Y+Z}\ . \tag{2.75}$$

We converted each reflection spectrum to its correspondent point (x,y coordinate) in the CIE chromacity diagram (Fig. 2.4). This method provides a direct view of the sample behavior

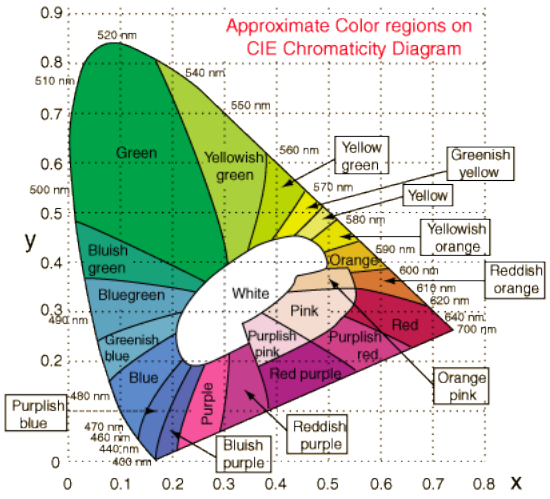

Figure 2.4: CIE 1931 chromaticity diagram. Image from [27]

with its angular dependence. The only drawback of this representation is that we loose the intensity of the reflected light. For this reason, the luminance spectra Y was calculated using Eq. (2.70) and plotted as a function of the incident angle. With both the CIE chromacity diagram and the luminance diagram, the spectral and intensity dependence as a function of the incidence angle are described.

Chapter 3

Fabrication

In this chapter, various fabrication methods and technologies used to fabricate samples are described. Specific explanations on the different samples are given in the related chapters.

3.1 Deposition of Bragg multilayer reflectors

We start with deposition by spin-coating of a stack of layers of two different polymers to form an organic quarterwave stack reflector on a cleaned one inch square glass substrate. The same structures have been realized on polycarbonate substrates as well as on flexible and transparent plastic sheets.
The glass substrates were cleaned by dipping in Deconex 12PA (from Borer Chemie AG) diluted at 4% in deionized water for 24 hours. Then the samples were rinsed in deionized water and dried with N2 jet. Finally they are backed in an oven at 200°C for 24 hours to remove moisture. This cleaning process is essential to obtain a substrate that permits to deposit polymer layers with a clean and defect-free surface.
The polymers should have particular characteristics, like solubility in two different solvents and non-miscibility. A relatively high distinct refractive index difference is of advantage for the quarterwave stack purpose. We follow the choice given in [6] where two polymers, ideal for their optical and mechanical properties, are used. The first polymer is the water soluble poly(vinyl alcohol) (PVA) and the second polymer the toluene soluble poly (N-vinycarbazole) (PVK). They have a refractive index of 1.56 and 1.72, respectively, at a wavelength of 500 nm [6]. They permit alternative coatings without interlayer problems, allowing to reach a large number of layers (> 40) required to build a multilayer Bragg mirror with high reflectivity. For the two polymers, different molecular weights (mw) were dissolved. It was found that the solubility can be very difficult to achieve with the chosen solvents for high molecular weight. It was important to choose the right molecular weight because of the solubility of the polymer in their solvents. In fact, the less molecular weight the more soluble the polymer. For PVA, a low hydrolysis percentage guaranties a good solubility in water [3]. Taking into account these parameters, PVA with average molecular weight Mw $\approx$ 9,000-10,000, 80% hydrolyzed from Sigma-Aldrich and PVK with average molecular weight Mw $\approx$ 40,000 from Polysciences were chosen.
Different solutions with 2-5%wt were made to reach the various layers thicknesses needed to

have a defined layer thickness of polymer. A chosen concentration of the solution gives an approximate thickness of the spun layer and spin speed must be adjusted for fine tuning of the thickness.
Single layer thickness were measured on test plates using an Alpha-Step profilometer by removing a part of the layer in the center of the spun layer. To obtain a good dissolution of the polymer in the solution, that is a key point for having good surface quality, it was also important to rise the temperature of the solution close to the boiling point. The PVA-water solution was heated on a hot plate till the boiling point and the PVK-toluene solution was heated in a ventilated oven until bubbles appear. The solution could be used directly after cooling down to room temperature. The fabrication process is based on successively spinning PVA and PVK layers on the precleaned glass substrate. A typical spin time is 20 seconds. Because of the very thin layer thickness, the drying process for solvent evaporation between each spin-coating was not necessary. With this method, samples with a large number of

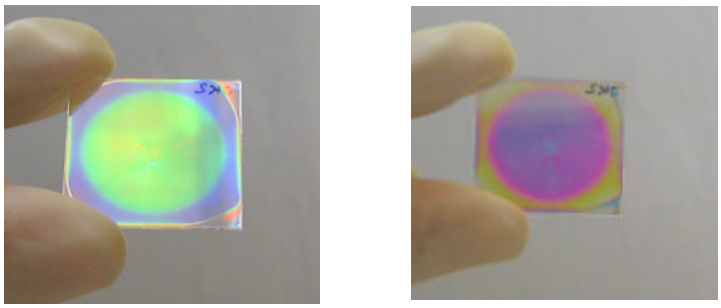

(a) (b)

Figure 3.1: Photos of a sample spun on a glass substrate: (a) reflection; (b) transmission

layers could be obtain very conveniently, giving very high reflection efficiency. On one inch glass substrate, a circular homogeneous Bragg mirror of approximatively 16 mm in diameter was obtained. Figures 3.1(a) and 3.1(b) are pictures of the same multilayer Bragg reflector seen in reflection and transmission, respectively. This Bragg reflector is formed of a total of 40 layers. The first layer on glass substrate is a PVA layer. The layer thicknesses are $\approx 80 - 85$ nm and $75 - 80$ nm for PVA and PVK, respectively.

3.2 Grating fabrication

The master gratings were realized by laser beam interference. As illustrated in Fig. 3.2, a fringe pattern is created by interference of two beams.
The laser used is a Krypton laser with a wavelength of 413 nm and a maximal power $P = 1$ W. The intensity distribution of the fringe pattern is recorded in a photoresist material. The photoresist is then developed and the exposed part of the photoresit is dissolved (positive photoresist). An atomic force microscope (AFM) allows to verify profile and period of the gratings.
For the recording we take two linearly polarized plane waves of frequency ω, with electric

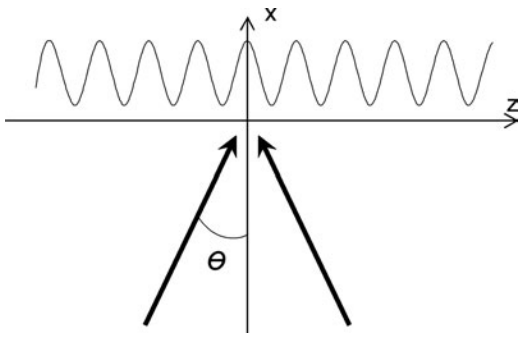

Figure 3.2: Intensity of the fringe pattern created by the interference of two laser beams.

fields described by

$$\mathbf{E}_1 = \mathbf{A}_1 \exp\left[i\left(\omega t - \mathbf{k}_1 \cdot \mathbf{r} + \phi_1\right)\right], \; and \quad \mathbf{E}_2 = \mathbf{A}_2 \exp\left[i\left(\omega t - \mathbf{k}_2 \cdot \mathbf{r} + \phi_2\right)\right] \tag{3.1}$$

with the amplitudes $\mathbf{A}_i$, wavevectors $\mathbf{k}_i$ and phases ϕ_i. The measured intensity of the superposition of the two waves becomes

$$I = |\mathbf{E}_1 + \mathbf{E}_2|^2 = |\mathbf{E}_1|^2 + |\mathbf{E}_2|^2 + 2\mathbf{A}_1 \cdot \mathbf{A}_2 \cos\left(\mathbf{K} \cdot \mathbf{r} - \phi\right) \tag{3.2}$$

with $\mathbf{K} = \mathbf{k}_1 - \mathbf{k}_2$ and $\phi = \phi_1 - \phi_2$. In our case, the two beams are obtained from the same laser, the polarizations are the same and the two fields are mutually coherent, i.e. $\phi = constant$. The intensity of the interference pattern (Eq. 3.2) can also be written as

$$I = |\mathbf{E}_1 + \mathbf{E}_2|^2 = I_1 + I_2 + 2\sqrt{I_1 I_2} \cos\left(\mathbf{K} \cdot \mathbf{r} - \phi\right) \tag{3.3}$$

where $I_i = |E_i|^2$. The period of the interference pattern, and therefore the periodicity of the exposed grating, is given by Eq. (3.4), with the refractive index of the media n, the wavelength of the laser light λ, the half angle between the two incident beams θ and the grating period $\Lambda_{grating}$

$$\Lambda_{grating} = \frac{\lambda}{2n \sin\theta} \tag{3.4}$$

This period varies as a function of the laser wavelength and the incident angle. Since the wavelength of the laser is fixed, the choice of the angle between the two beams gives the period of the fringes. A setup developed and realized by a former member of the IMT applied optics laboratory was used [47]. This setup is illustrated in Fig. 3.3. A rotating table with the photoresist sample and mirror placed at 90° is used to create the interference pattern on the photoresist surface. Usually, a glass substrate with 2 μm thick layer of photoresist was used. An absorptive coating was placed on the back side of the substrate. This absorptive layer was done by two different ways depending on conditions. A simple painted black layer gave good results but was difficult to remove for samples used in transmission. Another efficient absorptive system was used for sample tested in transmission. An absorbent thick glass was placed on the back of the substrate and an index matching oil between the two plate to avoid reflection at the interfaces. The thick absorbent glass is removed after the grating exposition. The back of the sample must be cleaned with a solvent to remove all traces of the index matching oil before development of the photoresist.

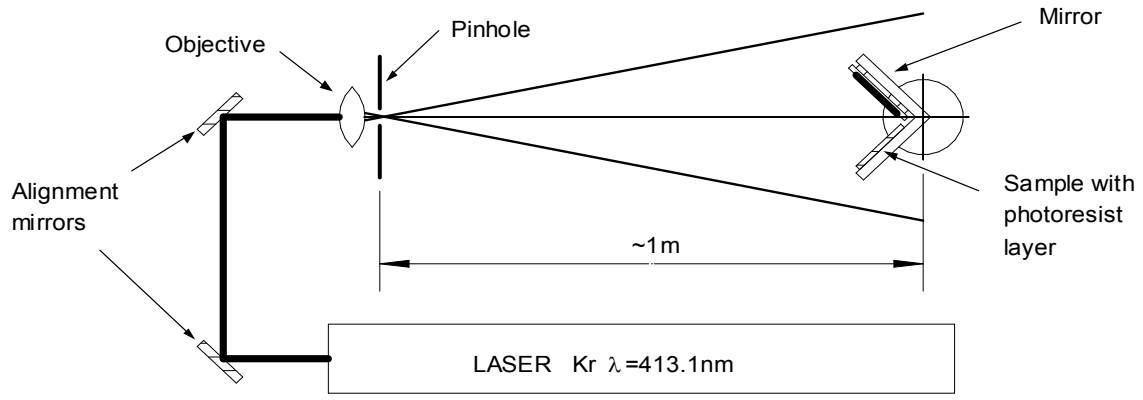

Figure 3.3: Illustration of the recording setup (two-beam interference). One beam is reflected by the mirror and illuminates the photoresist, the other beam reaches directly the sensitive surface. The interference pattern is recorded in the photoresist [47].

3.3 Microlens fabrication

For the microlenses fabrication, we followed the known process published in literature [29]. Basically, microcylinders in resist are produced by photolithography. The diameter of the cylinder will give the diameter of microlenses. Then, the cylinders are melt to produce spherical microlenses. A more detailed description is given hereafter. After cleaning the

Figure 3.4: Microlenses fabrication procedure. Photolithography, developing and melting of the resist cylinders to form the spherical microlenses.

wafer, we rinsed it with deionized water and dry it with nitrogen pressure. The wafer is then put at 200°C for minimum one hour to remove moisture traces. A thin base layer of photoresist ($h \approx 0.6\,\mu$m) is then spun on the wafer. This layer is hardened by a bake process at 160°C for 30 minutes. This layer permits a better control of the microlens quality. The top layer is then spun at the chosen thickness h_C to reach the right height h_L of the microlenses at the end of the process. For this, we simply calculate the volume of a microcylinder V_C with Eq. (3.5) and compare it to the volume of the microlenses V_L in Eq. (3.6) after the melting process, with $r = \emptyset/2$ corresponding to the cylinder radius and R being the radius of curvature of the microlens.

$$V_C = \pi r^2 h_C \tag{3.5}$$

$$V_L = \frac{1}{3}\pi h_L^2(3R - h_L) = \frac{1}{6}\pi h_L(3r^2 + h_L^2) \tag{3.6}$$

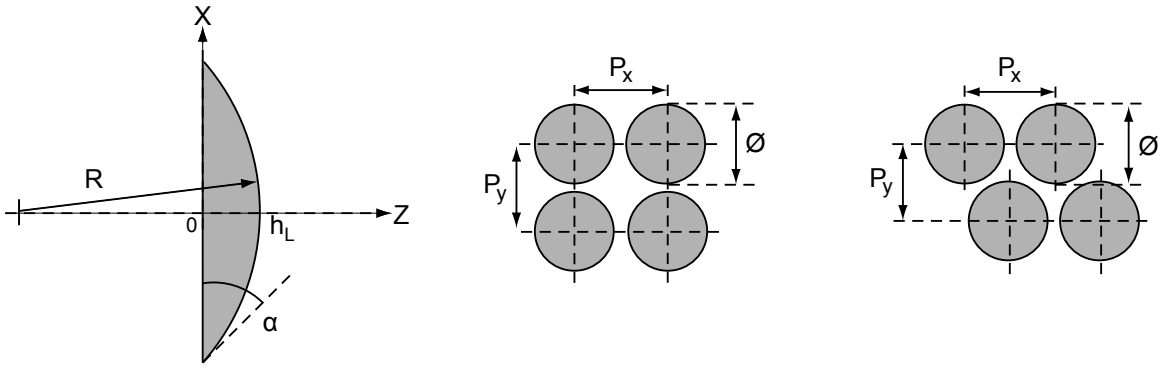

Figure 3.5: Microlenses dimensions. Lens diameter ∅, lens height h_L, radius of curvature R. The rectangular and hexagonal arrangement of microlens array is shown, with p_x and p_y the periodicity in the $x-$ and $y-$directions .

Theoretically, if the volume is conserved and the shape of the lens is perfectly spherical, one can simply equal Eqs. (3.5) and (3.6) to find the relation:

$$h_C = \frac{h_L}{2} + \frac{h_L^3}{6r^2} \tag{3.7}$$

Usually, the volume of the photoresist shrinks due to degas of solvents and therefore a correction factor has to be applied. The following relation permits to have a good approximation of the microlenses height:

$$h_L = \gamma h_C \qquad \gamma \approx 1.3 - 1.7 \tag{3.8}$$

The factor γ depends on the lens diameter d and the resist type. Once the top layer was spun, the layer must be dried for four hours with temperature gradually increasing from 40 to 70°C. This process is particularly important in the case of transfer of the microlenses in the substrate with dry etching processes. To generate the structure, the wafer is exposed with UV light through a mask (see Fig. 3.4). The exposed wafer is then developed and an array of microcylinders is formed. To form the lens shapes, the wafer is put on a hot plate at 150°C for 10 minutes and the microcylinders melt. Due to surface tension, spherical shape that minimize the total energy can be obtained.

3.4 Replication of micro-optics elements

Two different methods to replicate the micro-optics elements were tested. The first method called soft replication uses soft mold and the replication is done in a UV curing polymer. The second method, called hot embossing uses hard mold and replication are done in polycarbonate.

Replication in a UV-curing polymer

For the first method, the fabrication of the stamp follows the process illustrated in Fig. 3.6. The fabrication of the PDMS mold was done as given in manufacturers recipes. We used

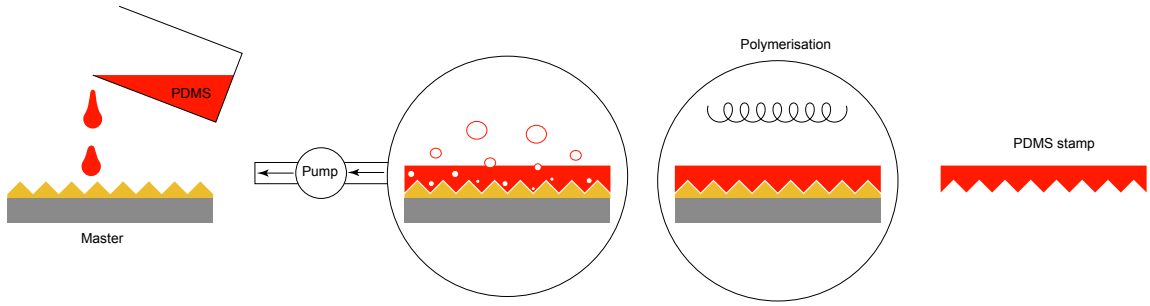

Figure 3.6: Illustration of the steps to fabricate a soft mold of a master sample.

the SYLGARD 184 (Dow Corning). We mixed 1:9 ratio of curing agent with PDMS. When stirring and mixing, a lot of air bubble are trapped in the mixture. If the solution is used in this state, the replicated element will not have a clean and smooth surface because the bubbles create a lot of defects on the stamp surface. To avoid this problem, the solution is placed under a progressive vacuum pumping to degas. Then the PDMS solution is poured on the reference grating structure, and baked for 24 hours at 50°C. The result of the baking process is that the PDMS solution hardened but stay flexible enough and can be separated easily from the original structure without destroying it. The mould is ready to be replicated in a uv curing glue.

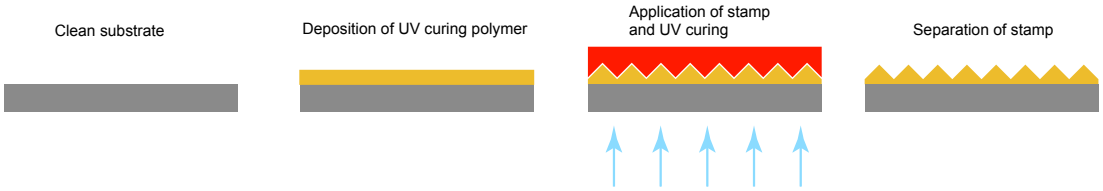

Figure 3.7: Illustration of the steps to replicate a structure with a soft stamp.

The fabrication of replicated structures follows the process illustrated in Fig. 3.7. A thin layer of a UV curing glue is deposited on a substrate. We used different optical adhesive from Norland Products [4], mostly the optical adhesive NOA61 and NOA65 with refractive index $n \approx 1.56$ and $n \approx 1.52$, respectively. One can either deposit a drop of pure optical adhesive that gives relatively thick residual layer of adhesive under the replicated structure, or dilute the optical adhesive in a solvent and deposit a thinner layer by spin coating. The first method was principally used to replicate microstructures like microlens and microprism arrays. The second method was applied to nanostructures like gratings. It allows to have a better control of the layer thickness that can be useful in some applications. Then a poly(dimethylsiloxane) (PDMS) replication stamp of the micro- or nanostructure was applied on the surface of the fresh NOA layer. The replication stamp is usually pressed against the surface of the optical adhesive to form an homogenous replicated layer. To harden the glue, the sample was cured for 10 minutes in UV chamber, with an irradiance of $2\,\mathrm{mW/cm^2}$. The principle line of the UV chamber peaks at 365 nm. The stamp was then removed and the sample was cured again for 10 minutes to complete hardening the adhesive.
With this process, a replication of the stamp in the optical adhesive was obtained and so,

gave a micro- or nanostructure in a transparent material with optical properties similar to glass.

Hot embossing

Due to the possibility to fabricate samples on various substrates, including plastic substrates, an attempt to spin multilayer Bragg reflectors on polycarbonate substrates was done. It was shown that this deposition is possible. The first layer directly on the polycarbonate (PC) is ideally the PVA layer because it is water soluble. A PVK layer could also be deposited directly on PC but the solvent dissolves partially the surface if there was a delay between dropping the solution on substrate and spin-coating. A problem was cleaning the surface prior to the spin coating process. For plastic substrates it is clearly more difficult to clean the surface without damaging it. The layer were deposited on PC directly after removing the protective blue tape layer. The obtained Bragg mirror exhibits good temperature stability. We could heat up the PC plate with the multilayer Bragg mirror to 150°C on a hot plate without any visible deterioration of the mirror. At 180°C the PC plate began to soften and bent.
Several attempts of hot embossing of gratings directly on multilayer Bragg reflectors were done to calibrate pressure and temperature of the mould. It is difficult to adjust the parameters to avoid layers to be melt or removed during the process. The advantage could be to have the grating directly scribed in the multilayer Bragg mirror and give samples with structures similar to the one of some butterfly's (see the morpho butterfly structure in [8]).

Chapter 4

Multilayer Bragg reflector

4.1 Perfect Bragg reflector characteristics

A perfect Bragg reflector is build from an alternative stack of thin layers with high and low refractive index material. The thicknesses of the layers are respectively $t_H = \lambda/4n_H$ and

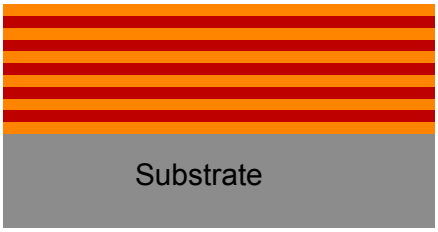

Figure 4.1: A Bragg reflector is build from an alternative stack of thin layers with high and low refractive index material. The thicknesses of the layers are respectively $t_H = \lambda/4n_H$ and $t_L = \lambda/4n_L$, with n_H and n_L the refractive index of the two materials, and λ the center wavelength of the reflector

$t_L = \lambda/4n_L$, with n_H and n_L the refractive index of the two material, and λ the center wavelength of the reflector. A fraction of the incident beam is reflected at each interface in the stack . A phase shift of π at normal incidence is induced when the incident light goes from low-index medium in a high-index medium. Since the phase difference of the reflected beams is zero or a multiple of 2π they interfere constructively. An analytical calculation of the reflectance dependence as the function of the incident wavelength for TE and TM-polarization is detailed in [49]. The maximum of reflectance can be derived. The reflectance of a quarter-wave stack at normal incidence with (2p + 1) layers and with high refractive index for the first and the last layer is given by

$$R = \left(\frac{1-Y}{1+Y}\right)^2 \tag{4.1}$$

with the optical admittance Y

$$Y = \left(\frac{n_H}{n_L}\right)^{2p} \frac{n_H^2}{n_S} \tag{4.2}$$

and n_S the refractive index of the substrate. Figure 4.2(a) shows the calculated reflection efficiency of a multilayer Bragg reflector on a glass substrate as a function of the number of layers with the characteristics of the polymer used in this work. The refractive indices are $n_H = 1.72$ for the polymer PVK and $n_L = 1.56$ for the PVA. The corresponding thicknesses of the layer are respectively $t_H = \lambda/4n_H = 82.85\,\text{nm}$ and $t_L = \lambda/4n_L = 91.35\,\text{nm}$ when the center wavelength of the reflector is $\lambda = 570\,\text{nm}$. One sees that since the refractive index difference between the two materials is small, a large number of layers are required to reach high reflection efficiency. For example around 30 layers are required to reach 90% reflection efficiency. On the other hand, the spectral width $\Delta\lambda$ of such a quarter-wave stack is proportional to the refractive index difference and given by [49]

$$\Delta\lambda \approx \frac{4}{\pi}\lambda \arcsin\left(\frac{n_H - n_L}{n_H + n_L}\right) \tag{4.3}$$

For $n_L = 1.56$, $n_H = 1.72$ and $\lambda = 570\,\text{nm}$, one obtains $\Delta\lambda \approx 35\,\text{nm}$ that gives a reflector with a good spectral purity. The value for $\Delta\lambda$ given in Eq. (4.3) is right for the case where there are enough layers to reach a reflection efficiency close to unity. The spectral

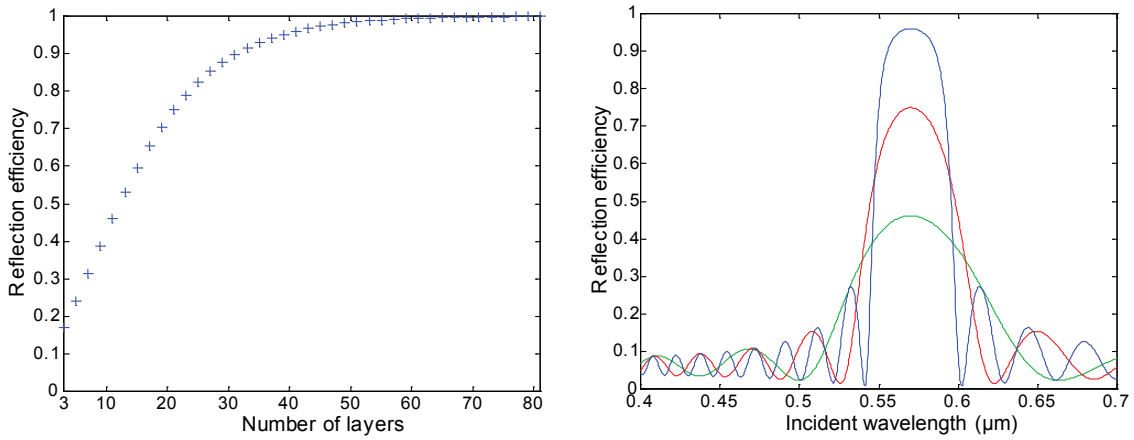

(a) (b)

Figure 4.2: (a) Calculation of the reflection efficiency of a multilayer Bragg reflector on glass substrate as a function of the number of layers. The multilayer reflector is built from an alternative stack of thin layers with high and low refractive index material, high refractive index for the first and the last layer. The thicknesses of the layer are respectively $t_H = \lambda/4n_H$ and $t_L = \lambda/4n_L$, with $n_H = 1.72$ and $n_L = 1.56$ the refractive index of the two material, and $\lambda = 570nm$ the center wavelength of the reflector. (b) Calculation of the reflection efficiency as a function of the incident wavelength for the case of 11, 21 and 41 layers.

width becomes larger if the number of layer are limited. The results of a calculation for the reflection efficiency as a function of the incident wavelength for a Bragg reflector with 11, 21 and 41 layers is illustrated in Fig. 4.2(b).

Another very important aspect of a multilayer Bragg structure is its angular dependent reflection. This effect is illustrated in Fig. 4.3(a). For angle of incidence of 0°, 15°, 30°, 45° and 60°, the reflection efficiency of a multilayer Bragg reflector with 11 layers and a reflection band at normal incidence centered at $\lambda = 570\,\text{nm}$ are calculated. One sees a shift

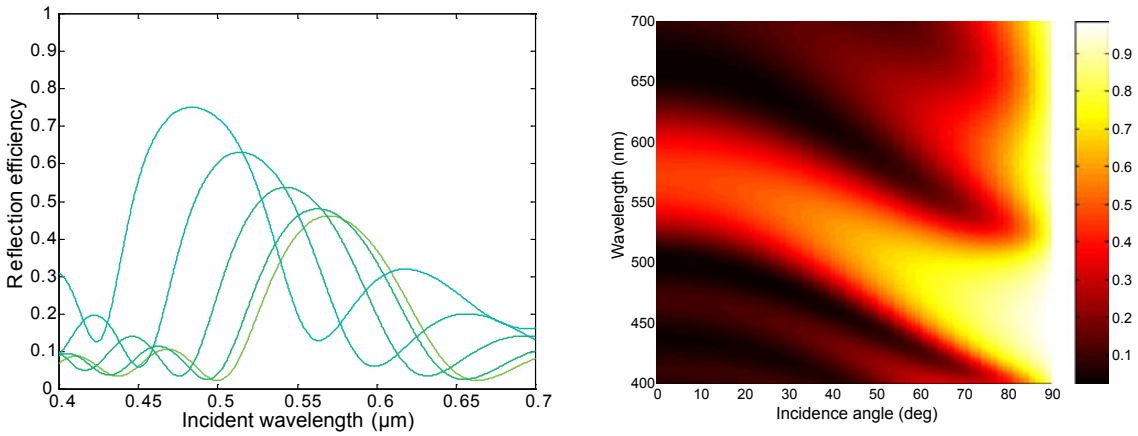

(a) (b)

Figure 4.3: (a) Angular dependent reflection of the TE component of a multilayer Bragg reflector with a total of 11 layers and a reflection band centered at $\lambda = 570\,\text{nm}$. The different curves correspond to the angle of incidence of 0°, 15°, 30°, 45° and 60°. (b) The reflection efficiency as a function of the angle of incidence for the same sample is represented in a map view.

of the maximum of reflection towards the shorter wavelength and a global increase of the reflection efficiency when the angle of incidence increase. In order to have an overview of the reflection properties as a function of the incident angles, a map of the reflection efficiency as a function of the angle of incidence is represented in Fig 4.3(b). This representation will be preferred since it gives in one view the reflection efficiency of the sample at all angles.

4.2 Measurement setup

To characterize the sample we use a collimated illumination and a measurement setup providing spectral reflection measurements for various incident angles and conical angles (goniometer). The goniometer is shown in Fig. 4.4. A Koehler illumination mount with a xenon

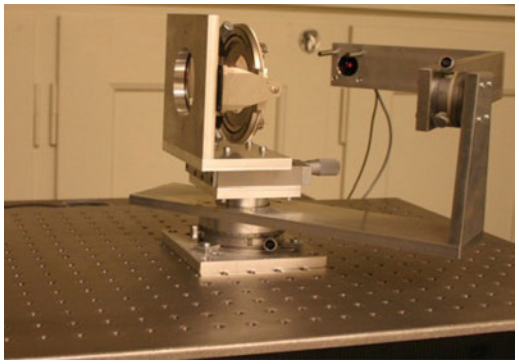

Figure 4.4: The goniometer used for measurement allows reflection and transmission measurements.

lamp that covers the visible spectrum was used. It allows us to have control over the spatial coherence of the illumination as well as the spot size and intensity. A xenon lamp was used

to have high intensity in the blue part of the spectrum. The chosen focusing spotsize was approximatively 1.5 mm in diameter. The spot on the sample must be sufficiently small to be reduced to an homogenous region of the sample. We use an Ocean Optics S2000 fiber optic spectrometer to record the reflected spectra. The fiber core is 400 μm in diameter. We use a lens with an aperture diameter of 5 mm and a focal length of 10 mm to focus the light in the fiber. The distance sample-lens is about 30 cm. It means that the acceptance angle was about 1°. The head of the spectrometer is fixed on a rotating arm. The setup allows to change the angle of incidence from 0° to 90°.

4.3 Specular reflection measurement

We measured the specular reflection of the multilayer Bragg reflector. The geometry is illustrated on Fig. 4.5. For each incident angle the detector is rotated to follow the specular

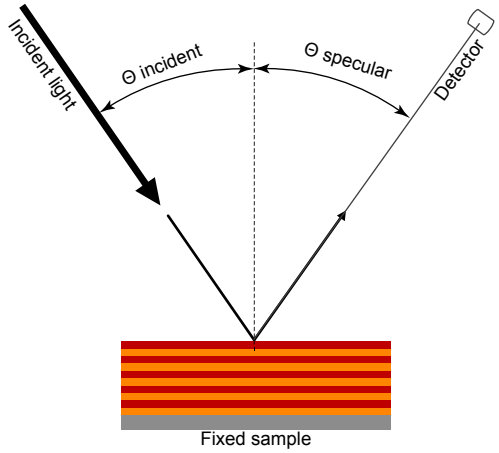

Figure 4.5: Specular reflection measurement. For each incident angle the detector is rotated to follow the specular reflection beam. The sample was rotated from 4° to 40°.

reflection beam. The measured spectra depend on the spectrum of the illumination and on the spectral characteristics of the optical elements between the sample and the detector (lens, fiber, spectrometer spectral sensitivity). We normalized each measurement by the spectrum of the lamp. Due to this normalization, some artefact or shifts can appear in the spectral region where the signal of the lamp is weak or not stable in time.
For incidence angles θ_i between 4° to 40°, we measured the specular reflection of the different multilayer Bragg reflectors. The results for a sample with a total of 9 layers and a reflection band centered at $\lambda = 570$ nm is shown in Fig. 4.6(a). The sample is made of 4 PVA layers and 5 PVK layers. The PVA and PVK thicknesses are ≈ 91 nm and 83 nm, respectively. A reflection band appears as expected. The center wavelength changes for larger angles of incidence and shows a cosine-like dependence as a function of the incident angle θ_i. The maximum reflectivity is at 570 nm at normal incidence. The Fig. 4.6(b) shows the corresponding calculated color coordinates in the CIE chromaticity diagram when the sample was illuminated by a normalized illuminant D65 that fits the daylight sky spectrum

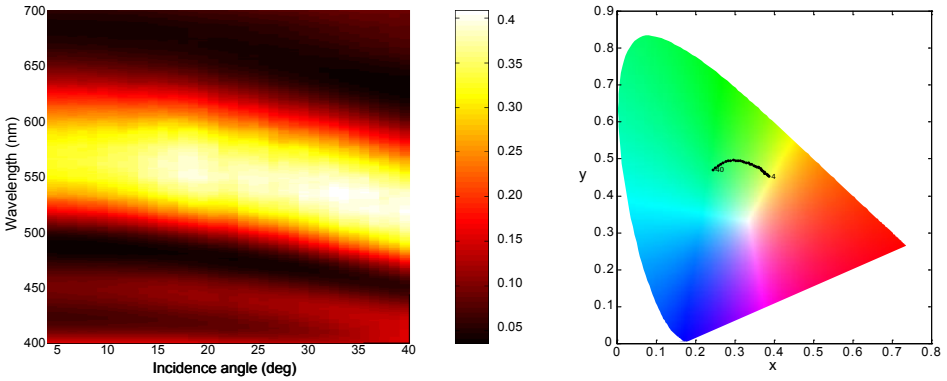

(a) (b)

Figure 4.6: (a) Specular reflection measurement for a multilayer Bragg reflector on glass substrate with a reflection band centered at $\lambda = 570nm$, with 4 PVA layers and 5 PVK layers. The thicknesses are ≈ 91 nm (PVA) and ≈ 83 nm (PVK) (sample n°3). (b) Color coordinates in the CIE chromacity diagram.

(see Chap. 2.5). The color changes from yellow to green. As excepted, shorter wavelengths are reflected when the incident angle increases. Results for sample with a total of 21 layers

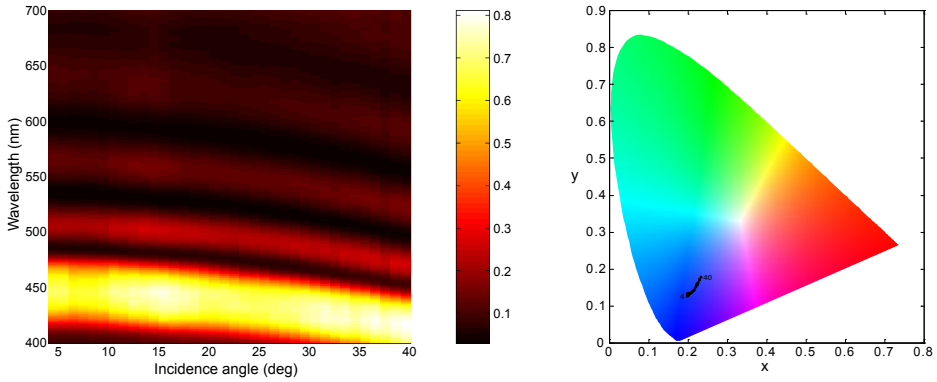

(a) (b)

Figure 4.7: (a) Specular reflection measurement for a multilayer Bragg reflector on glass substrate with a reflection band centered at $\lambda = 450$ nm, with 10 PVA layers and 11 PVK layers. The thicknesses are $\approx 70 - 75$ nm (PVA) and ≈ 65 nm (PVK) (sample n°5). (b) Color coordinates in the CIE chromacity diagram.

and a reflection band centered at $\lambda = 450$ nm is shown in Fig. 4.7(a). The sample is made of 10 PVA layers and 11 PVK layers. The PVA and PVK thicknesses are $\approx 70 - 75$ nm and 65 nm, respectively. A reflection band appears this time in the blue region since the Bragg mirror was designed to have its maximum reflection at 450 nm at normal incidence. The reflection efficiency is increased due to the larger number of layers. Figure 4.7(b) shows the corresponding calculated color coordinates. The reflection band shifts to shorter wavelengths and the color stays in the blue region for the different incidence angle.

The goal was to combine these multilayer Bragg reflectors with micro- or nano-optical elements replicated on top in an optical adhesive (see Chap. 5 and 6). It was therefore interesting to know the optical effect of adding a flat thick layer on top of a multilayer Bragg reflector. A rigorous simulation of the reflection efficiency of a multilayer Bragg reflector has been done. The results were compared to the simulation of the same reflector but with a thick and flat top layer with refractive index equal to the optical adhesive. Figure 4.8(a) shows the reflection simulation for a multilayer Bragg reflector with a total of 9 layers on glass substrate. The PVA thickness are 91.35 nm and the PVK thickness 82.85 nm. The measured value for the corresponding fabricated sample are given in Fig. 4.6(a). Figure 4.8(b)

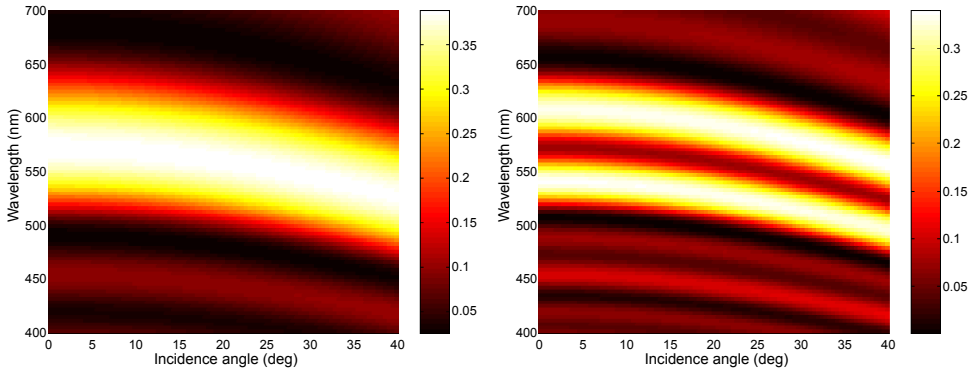

(a) (b)

Figure 4.8: (a) Reflection simulation for a multilayer Bragg reflector with 9 layers on glass substrate. The thicknesses are 91.35 nm (PVA) and 82.85 nm (PVK). The simulation can be compared with the measurement in Fig. 4.6(a). (b) Same configuration with a 1 μm top layer with refractive index 1.57.

shows the simulation of a multilayer Bragg reflector at 570 nm with a total of 9 layers with a top layer of $d = 1\,\mu$m. One can see that the original reflection band shown in Fig. 4.8(a) is splitted in two bands and have a smaller reflection wavelength width and a maximum reflection wavelengths just over and below the original reflection wavelength of the Bragg reflector alone. This effect depends on the thickness of the added last layer and must be kept in mind when adding structures on top of a multilayer Bragg structure.

4.4 Bragg reflector microcavity

If a defect is introduced in the center of a multilayer Bragg structure, a narrowband transmission filter can be obtained. Figure 4.9 shows an illustration of such a filter structure. The special case of a half-wave layer layer introduced between two quarter wave stacks gives a narrowband transmission filter. The transmission filter is centered in the center of the reflection band of the multilayer Bragg reflector. Figure 4.10(a) shows a simulation of the reflection at normal incidence for a multilayer Bragg reflector on a glass substrate with 11 PVA layers and 12 PVK layers, with a reflection band centered at $\lambda = 540$ nm. Figure 4.10(b) shows a simulation for the same structure but with a central PVA layer with thickness corresponding

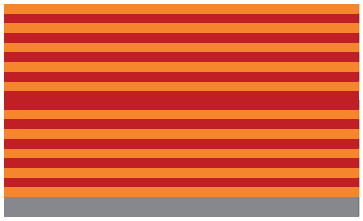

Figure 4.9: A waveguide is inserted between two Bragg reflectors creating a microcavity. The reflection properties of the multilayer Bragg mirror are modified considerably.

to $\lambda/2n_{PVA}$. One sees that the half-wave layer layer introduced between two quarter wave

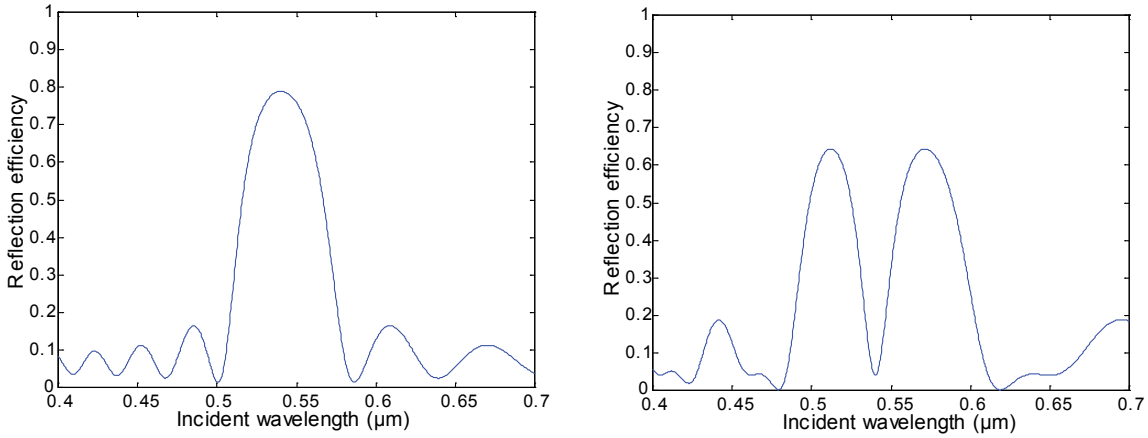

(a) (b)

Figure 4.10: (a) Specular reflection simulation for a multilayer Bragg reflector on glass substrate with 11 PVA layers and 12 PVK layers, with a reflection band centered at $\lambda = 540\,\text{nm}$, PVA thickness $\lambda/4n_{PVA} = 86.5\,\text{nm}$, PVK thickness $\lambda/4n_{PVK} = 78.5\,\text{nm}$. (b) Specular reflection simulation for a double Bragg reflector with a central microcavity on glass substrate, with 11 PVA layers, 12 PVK layers. The microcavity thickness is $\lambda/2n_{PVA} = 173.1\,\text{nm}$.(no69)

stacks gives a narrowband transmission filter centered in the center of the reflection band. Figure 4.11(a) shows how the wavelength of the filter varies if the thickness of the central layer is $0.6 \cdot \lambda/2n_{PVA}$, $0.8 \cdot \lambda/2n_{PVA}$, $1.2 \cdot \lambda/2n_{PVA}$ and $1.4 \cdot \lambda/2n_{PVA}$. One sees a shift of the narrow transmission band towards higher wavelength when the thickness of the central layer is increased from 0.6 to 1.4 time the thickness of a half-wave plate. The reflection sideband are also modified with the thickness of the central layer. Figure 4.11(b) summarizes the wavelength position of the transmission band as a function of the thickness of the central layer.

Figure 4.12 shows the specular reflection measurement for a double Bragg reflector with a PVA defect layer in the center. The 11 PVA layers and 12 PVK layers are deposited on a glass substrate. The multilayer Bragg reflection band is centered at $\lambda = 540\,\text{nm}$. Here the wavelength of transmission is around $\lambda = 518\,\text{nm}$. In Fig. 4.11(b), this corresponds to a layer thickness of $0.75 \cdot \lambda/2n_{PVA} = 130\,\text{nm}$.

Figure 4.13(a) shows a simulation of the reflection at normal incidence for a multilayer Bragg

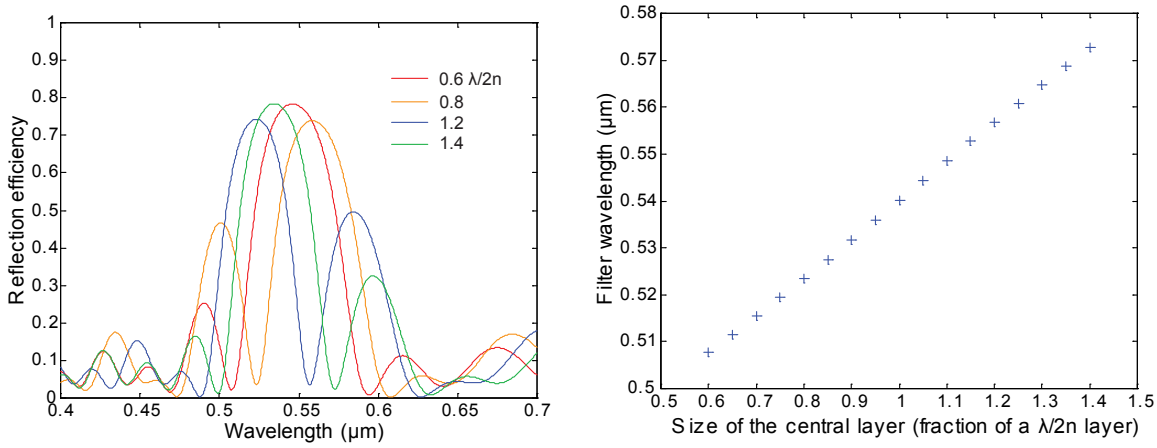

(a) (b)

Figure 4.11: (a) Reflection simulation at normal incidence for a double Bragg reflector on glass substrate with different microcavity thickness. The sample is made of 11 PVA layers and 12 PVK layers. The thickness of the central layer is $0.6 \cdot \lambda/2n_{PVA}$, $0.8 \cdot \lambda/2n_{PVA}$, $1.2 \cdot \lambda/2n_{PVA}$ and $1.4 \cdot \lambda/2n_{PVA}$, respectively, with $\lambda/2n_{PVA} = 173.1\,\text{nm}$. (b) Wavelength position of the transmission band as a function of the thickness of the central layer.

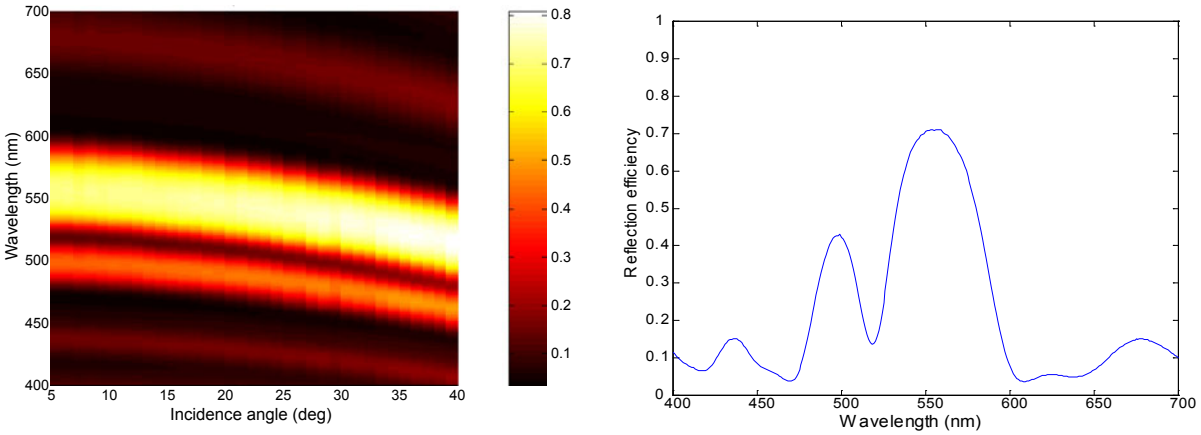

(a) (b)

Figure 4.12: (a) Specular reflection measurement for a double Bragg reflector with a central microcavity on glass substrate. The sample is made of 11 PVA layers and 12 PVK layers. The thickness of the central PVA layer is $\approx 130\,\text{nm}$. The thicknesses of the other layers are $\approx 85\,\text{nm}$ (PVA) and $\approx 75\,\text{nm}$ (PVK). (b) Reflection efficiency at incident angle $\theta = 4\,^\circ$.

reflector on a glass substrate with 16 PVA layers and 17 PVK layers, with a reflection band centered at $\lambda = 550\,\text{nm}$.

Figure 4.13(b) shows a simulation for a similar structure but with the central PVK layer with thickness corresponding to $\lambda/2n_{PVK}$. Like in the case of low refractive index, a high refractive index defect introduced in the center of a multilayer Bragg structure creates a narrowband transmission filter between two reflecting sidebands. Figure 4.14(a) shows how the center wavelength varies if the thickness of the central layer is $0.6 \cdot \lambda/2n_{PVK}$, $0.8 \cdot \lambda/2n_{PVK}$,

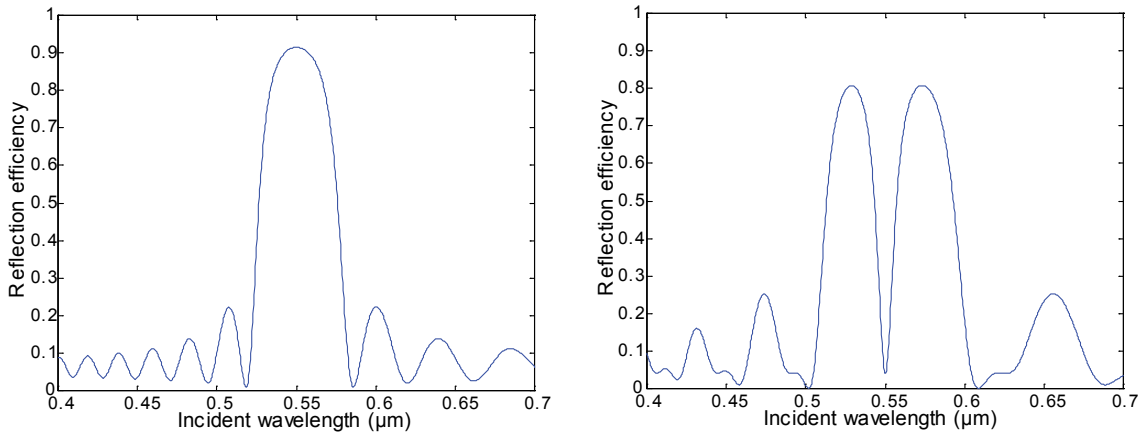

(a) (b)

Figure 4.13: (a) Specular reflection simulation for a multilayer Bragg reflector on a glass substrate with 16 PVA layers and 17 PVK layers, with a reflection band centered at $\lambda = 550\,\text{nm}$, PVA thickness $\lambda/4n_{PVA} = 88.1\,\text{nm}$, PVK thickness $\lambda/4n_{PVK} = 79.9\,\text{nm}$. (b) Specular reflection simulation for a double Bragg reflector with a central microcavity on a glass substrate, with 16 PVA layers, 17 PVK layers, the microcavity thickness is $\lambda/2n_{PVK} = 159.9\,\text{nm}$.

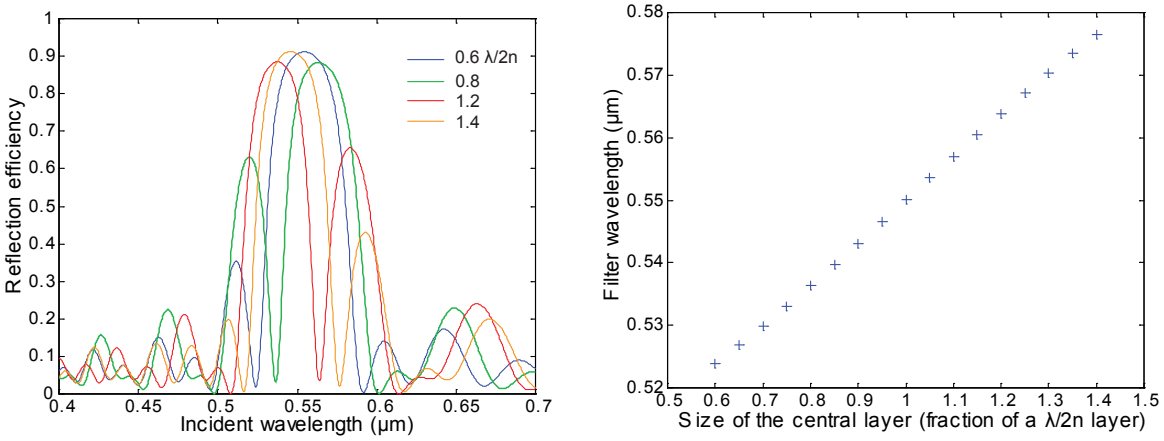

(a) (b)

Figure 4.14: (a) Reflection simulation at normal incidence for a double Bragg reflector with a reflection band centered at $\lambda = 550\,\text{nm}$ on a glass substrate with different microcavity thickness. The sample is made of 17 PVK layers and 16 PVA layers. The thickness of the central layer is $0.6 \cdot \lambda/2n_{PVK}$, $0.8 \cdot \lambda/2n_{PVK}$, $1.2 \cdot \lambda/2n_{PVK}$ and $1.4 \cdot \lambda/2n_{PVK}$, respectively, with $\lambda/2n_{PVK} = 159.9\,\text{nm}$. (b) Wavelength position of the transmission band as a function of the thickness of the central layer.

$1.2 \cdot \lambda/2n_{PVK}$ and $1.4 \cdot \lambda/2n_{PVK}$. Here again a shift of the narrow transmission band towards higher wavelengths is induced when the thickness of the central layer is increased from 0.6 to 1.4 time the thickness of a half-wave plate. Figure 4.14(b) summarize the wavelength position of the transmission band as a function of the thickness of the central layer. Figures 4.15(a), 4.16(a) and 4.17(a) show the specular reflection measurement for three similar samples but with a different central layer thickness. Each sample has a double Bragg re-

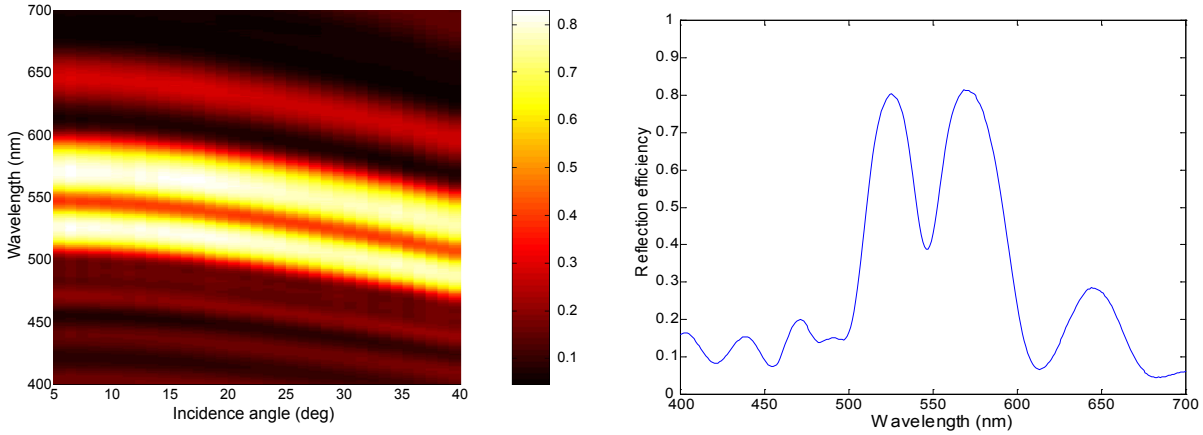

(a) (b)

Figure 4.15: (a) Specular reflection measurement for a double Bragg reflector with a central microcavity on a glass substrate. The sample is made of 16 PVA layers and 17 PVK layers. The thickness of the central PVK microcavity is $\approx 160\,\text{nm}$. The thicknesses of the other layers are $\approx 88\,\text{nm}$ (PVA) and $\approx 80\,\text{nm}$ (PVK). (b) Reflection efficiency at incident angle $\theta = 4\,^\circ$.

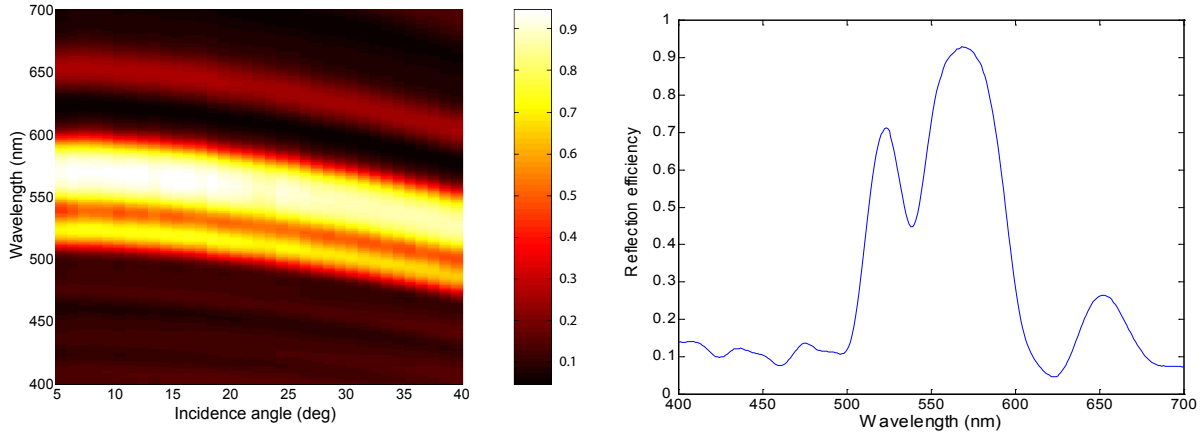

(a) (b)

Figure 4.16: (a) Specular reflection measurement for a double Bragg reflector with a central microcavity on a glass substrate. The sample is made of 16 PVA layers and 17 PVK layers. The thickness of the central PVK microcavity is $\approx 130\,\text{nm}$. The thicknesses of the other layers are $\approx 88\,\text{nm}$ (PVA) and $\approx 80\,\text{nm}$ (PVK). (b) Reflection efficiency at incident angle $\theta = 4\,^\circ$.

flector on a a glass substrate with 16 PVA layers and 17 PVK layers, with a thicker central PVK layer. The multilayer Bragg reflection band is centered at $\lambda = 550\,\text{nm}$. As excepted the wavelength of transmission for the different sample are not the same due to the different central layer thicknesses. Figures 4.15(b), 4.16(b) and 4.17(b) show the reflection efficiency at incident angle $\theta = 4\,^\circ$. The wavelengths of transmission are around $\lambda = 546\,\text{nm}$, $539\,\text{nm}$ and $528\,\text{nm}$, respectively. Figure 4.14(b) shows that these filter wavelengths correspond theoretically to layer thicknesses of around $\lambda/2n_{PVK} = 160\,\text{nm}$, $0.85 \cdot \lambda/2n_{PVK} = 136\,\text{nm}$ and $0.7 \cdot \lambda/2n_{PVK} = 112\,\text{nm}$, respectively. Despite a good agreement between measurements and simulations, the level of transmission at the filtering frequency is not as low as excepted. A

possible reason is that the thickness of the fabricated samples have an average roughness and/or thickness that vary from the theoretical values. For example, if the thickness of the central layer varies over the sample surface, the transmission signal will be an average from the signal obtained for the different thicknesses and therefore the transmission will be reduced. A reason for this variation could be due to the fact that we added a fraction of another solvent (THF) in order to reach easily the solubility of the solution for the thicker layer. This solvent is very efficient for all polymer and dissolve PVK but also PVA.

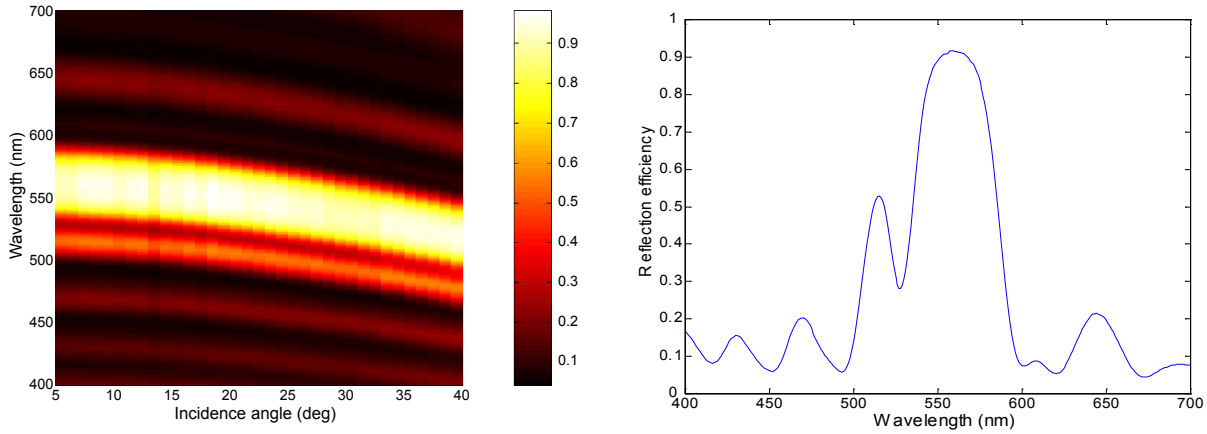

(a) (b)

Figure 4.17: (a) Specular reflection measurement for a double Bragg reflector with a central microcavity on a glass substrate. The sample is made of 16 PVA layers and 17 PVK layers. The thickness of the central PVK microcavity is $\approx 110\,\text{nm}$. The thicknesses of the other layers are $\approx 88\,\text{nm}$ (PVA) and $\approx 80\,\text{nm}$ (PVK). (b) Reflection efficiency at incident angle $\theta = 4\,^\circ$.

4.5 Bragg reflector with dye doped microcavity layer

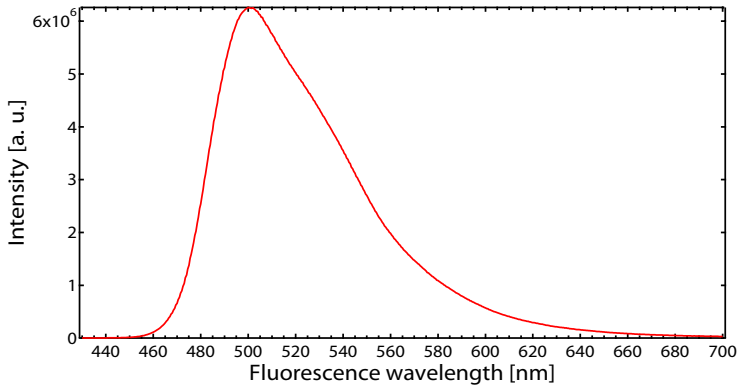

Figure 4.18: Fluorescence emission spectrum of Coumarin 6 dissolved in ethanol [5].

Since the deposition of a polymer multilayer Bragg reflector with the addition of a defect is possible, an attempt to introduce a fluorescent dye inside the defect layer was done. One

can imagine to fabricate a DBR laser with this method. Our choice of dye was made for the Coumarin 6 because of its fluorescence emission spectrum in the green. Figure 4.18 shows the fluorescence emission spectrum of Coumarin 6 dissolved in ethanol. Figure 4.19(a) shows

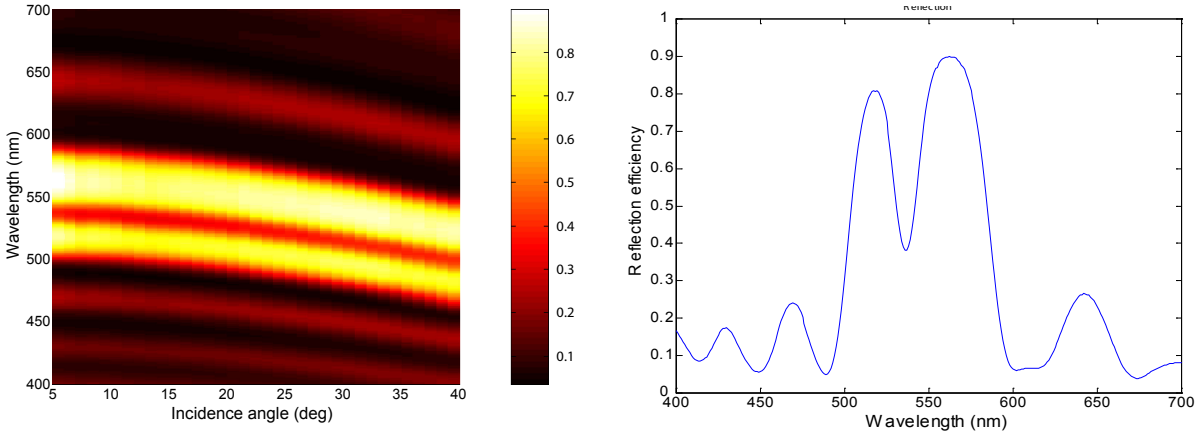

(a) (b)

Figure 4.19: (a) Specular reflection measurement for a double Bragg reflector with a central microcavity. The 16 PVA layers and 17 PVK layers are deposited on a glass substrate. The thickness of the PVK microcavity is $\approx 145\,\text{nm}$ and contains 1.5 % wt of Coumarin C6 dye. The thicknesses of the other layers are $\approx 86\,\text{nm}$ (PVA) and $\approx 78\,\text{nm}$ (PVK). (b) Reflection efficiency at incident angle $\theta = 4\,^\circ$.

the specular reflection measurement for a double Bragg reflector with a PVK defect layer in the center with addition of 1.5 % wt of Coumarin 6. The 16 PVA layers and 17 PVK layers are deposited on a glass substrate. The multilayer Bragg reflection band is centered at around 540 nm. The wavelength of transmission is around $\lambda = 536\,\text{nm}$ at $\theta = 4\,^\circ$. At

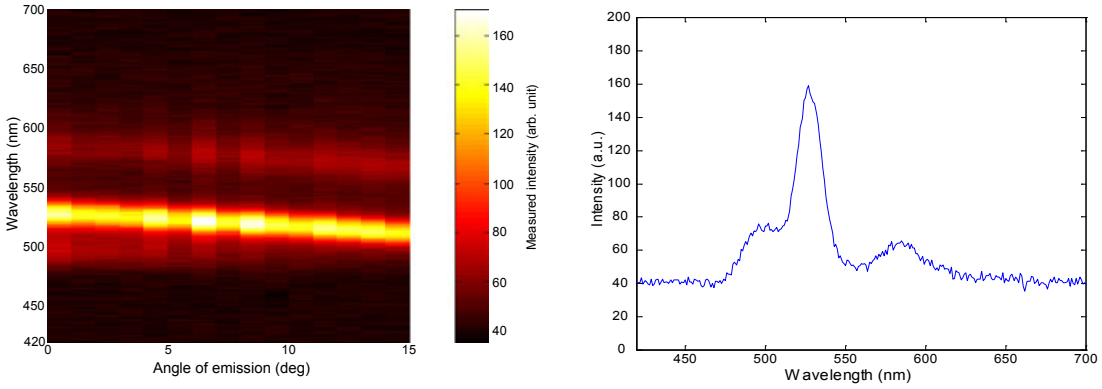

(a) (b)

Figure 4.20: (a) Fluorescent emission measured when the sample described in Fig. 4.19 is optically pumped with a pump laser at $\lambda = 405\,\text{nm}$. (b) Detail of the measurement for a measurement angle $\theta = 0\,^\circ$.

first sight and with a standard illumination, one cannot distinguish between this sample and a sample without addition of a dye. The effect of the dye is weak with a standard

illumination. The fluorescence was only measured if the sample was illuminated with a pump laser at $\lambda = 405\,\mathrm{nm}$. Figures 4.20(a) and (b) show the fluorescent spectrum emitted by the dye through the double multilayer Bragg reflector. The emission peak is measured at around $527\,\mathrm{nm}$ at $\theta = 0\,^{\circ}$. One can compare this emission spectrum with the reflection efficiency of the sample measured in Fig. 4.19(a) and (b). The wavelength of emission is well restricted to the spectral region where the sample has a lower reflection efficiency.

Chapter 5

Resonant grating structures for visual color effects

Our goal was to realize eye sensitive structural visual color effects on reasonably large surfaces. To get a particular color effect depending on orientation of the sample, we took example on various reflective and diffractive structures in animals, like butterfly [8], beetle and other spiders [31]. In these examples, the visual effects are due to a combination between multilayer Bragg reflections and diffraction at lateral grating structures. The goal was then to produce low cost nature-like structures with thin organic layers.
Polymeric multilayer Bragg reflectors were fabricated by spin-coating and combined with replicated diffractive gratings to produce artificial visual color effects (see Chap. 3 for fabrication details). The obtained devices are stable and robust. An illustration of a sample is given in Fig. 5.1. Angular dependent reflection spectrums for the visible are measured.

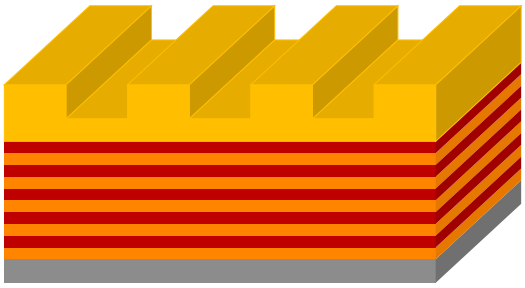

Figure 5.1: Illustration of a sample with a multilayer Bragg reflector with a square grating structure on top.

These results show that it is possible to obtain unexpected reflection effects like a loss of specular reflection at a given angle. A rich variety of color spectra can be generated, which is not possible with a single grating. This can be explained by the coupling of transmission of grating orders and the Bragg reflection band. A simple model permits to explain some of the spectral vs angular dependence of reflected light. The combined effects can also be

used to design particular filter functions and various resonant structures. Multilayer Bragg reflectors and corrugated gratings are widely used in optical components and optoelectronics such as interference filters, antireflection coatings, vertical cavity surface emitting lasers (VCSEL), distributed Bragg reflectors (DBR), distributed feedback (DFB) lasers [40,49,50]. Usually such devices are fabricated with inorganic oxides, mainly due to well known processes (sputtering, vapor deposition) and the possibility of high refractive index contrast, giving excellent control of the deposited thicknesses and high efficiency reflection bands with few layers. Polymers are generally less used because of the difficulty to find two polymers processable in thin layers, their low refractive index contrast and therefore the need of a bigger number of layers for an equivalent reflection efficiency. For polymers, it is more difficult to control the deposited thickness that depends on solution dilution, parameters of the spin coating process, humidity and surface cleanness. In specific domains where only visual effect are searched, these drawbacks can become advantages, resulting in narrower reflection spectrum that can potentially give some richer color shade. Not like other domains where very high efficiencies are sought, for visual color effect, even a small reflection efficiency can be useful when combined with a black absorber.
The recent developments of organic light emitting diodes (OLED) and other organic optical structures show the trend to all organic optical components. Reduction of costs of optical component is reached by new fabrication processes like replication and spin coating instead of costly molecular deposition under vacuum, e-beam writing or other processes. In this view, it seems also important to develop basic optical functionalities to be integrated in devices, such as waveguide, couplers, multilayer Bragg mirrors. Here, we are interested in producing color effects based on Bragg mirrors coupled with corrugated gratings.

5.1 Introduction

Different structures were studied. We can separate them into two categories. For the first group of samples, a grating with period $d = 600\,\text{nm}$ was used. With this grating, the diffraction orders were limited. In a second time, multiple orders gratings were studied. In this case, a grating with a period of $d = 1.5\,\mu\text{m}$ was used. In these two cases, the reflection wavelength and the reflectivity of the multilayer Bragg mirror were modified. All the samples were measured in two different configurations. In the first configuration, we wanted to measure the perceived effect given by a sample when illuminated with a fixed source and viewed by human eye. For this, we measured the samples in a configuration described in Chap. 5.5. In a second time, the samples were measured in the traditional specular reflection configuration. These last measurements allowed us to underline the different optical effects.

5.2 Principle

A simple model was developed in order to understand effects due to combination of the light from different grating orders. This simple model is drawn using the grating equation for

reflection

$$\sin\theta_m = \sin\theta_i + m\frac{\lambda}{d} \tag{5.1}$$

and for transmission

$$n_2 \sin\theta_{2_m} = n_1 \sin\theta_i + m\frac{\lambda}{d} \tag{5.2}$$

to calculate the diffraction angles of the different grating orders. With n_1 the refractive index of the incident medium, n_2 the refractive index of the transmitted medium, m the grating order, d the grating period and λ the wavelength of incident light.
Figure 5.2 shows the different contributions that combine to form the specular reflection considering the particular case where the grating diffracts light only in grating order $m = \pm 1$. The first contribution is the following: the incoming light is not diffracted (grating order

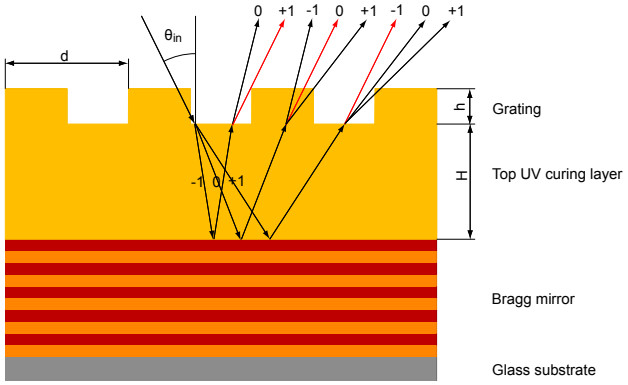

Figure 5.2: Ray optics view of the sample with the combination of different diffraction orders to form the specular reflection.

$m = 0$), reflected by the Bragg mirror and transmitted again without being diffracted (grating order $m = 0$). Another contribution to the specular beam can be added if a part of the incoming light is diffracted in the grating order $m = -1$, reflected by the Bragg mirror and transmitted in the grating order $m = +1$. A last contribution is formed by the incoming light diffracted in the grating order $m = +1$, reflected by the Bragg mirror and transmitted in the grating order $m = -1$.
If the diffraction efficiency of the reflected order $m = \pm 1$ is measured instead of the specular reflection, one has also different contributions. Here we still consider the particular case where the grating diffracts light only in grating order $m = \pm 1$. One can see that for a given wavelength, the angle of the reflected order $m = -1$ (see Fig. 5.3(a)) is the same as the one of the transmitted order $m = 0$ that is reflected by the Bragg mirror and diffracted by the grating in the order $m = -1$ (see Fig. 5.3(b)). The same angle is found for the order $m = -1$ transmitted by the grating, that is reflected by the Bragg mirror and transmitted again in the order $m = 0$ (see Fig. 5.3(c)).
The different components that have different spectral value due to the angular reflection dependence of the Bragg mirror are combined to form the measured signal. Depending on the efficiency of the different grating orders and the incident angle, a shift in wavelength for the maximum of reflection is observed.

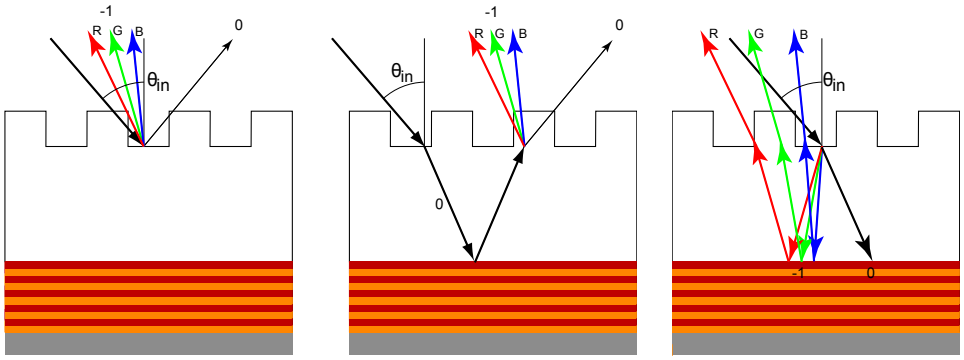

Figure 5.3: Illustration of the different contributions for the diffraction order $m = -1$ of a grating. (a) Direct reflection of the grating. (b) Reflection of the transmitted order $m = 0$ by the Bragg mirror and diffraction as order $m = -1$. (c) Reflection of the transmitted order $m = -1$ by the Bragg mirror and transmitted as order $m = 0$

The efficiency of the system and the change of the spectrum are given by the diffraction efficiency of the different grating orders and by the reflection of the Bragg mirror. The incident light is diffracted a first time before reaching the Bragg mirror and a second time after being reflected, when it is outcoupled from the grating. For the Bragg mirror, we can easily increase the number of layers to reach higher reflectivity. For the grating, the choice of small grating period to limit the number of grating orders can be used as a design parameter and can increase the efficiency of the system. With this simple scheme, one can design elements that generate a rich variety of color spectra.
Nevertheless a rigorous simulation is essential to describe all effects since the reflected spectrum depends on the efficiency of the grating orders (grating shape, height and period), the spectral response of the Bragg mirror (layers thicknesses, total number of layers, refractive index difference) and also on the thickness of the intermediate layer between the Bragg multilayer and the grating. Some interference effects show a strong dependence on the thickness of this intermediate layer and could only be explained with rigorous simulations.

5.3 Samples characteristics

Three representative samples are described and studied. For each one, an identical sample without top grating served as reference for comparison. The Bragg mirror were fabricated on a glass substrate as described in Chap. 3.1. The first two samples were designed to have a Bragg mirror with reflection peak around 570 nm. The third one was designed for 450 nm. Due to sensitivity of the eye being smaller in the blue part of the spectrum, we increased the number of layers of the Bragg reflector to reach higher reflectivity.
Two different grating periods, $d = 600\,\text{nm}$ and $d = 1.5\,\mu\text{m}$ were used, with grating depths $h = 350\,\text{nm}$ and $h = 1.3\,\mu\text{m}$, respectively. The grating were fabricated in photoresist and replicated in an optical adhesive on top of the multilayer Bragg reflector as described in Chaps. 3.2 and 3.4, respectively. Here, the optical adhesive was diluted in a solvent and

deposited by spin-coating. This method allows control over the thickness of the optical adhesive. The thickness of the residual layer can be controlled if the deposition of the adhesive layer is done in two steps. The first step consists in depositing a first layer by spin coating and to expose it to UV light in order to harden it. A second layer can be deposited over the first layer by spin coating and used to replicate the grating. If the mould is applied with enough force on the substrate, it will touch the first layer of optical adhesive. As a result, the residual layer between the replicated grating and substrate (here the multilayer Bragg reflector) is known. Figures 5.4 and 5.5 show AFM measurements of the replicated grating with 600 nm and 1.5 μm period, respectively. The measured gratings are about 350 nm and $h = 1.3\,\mu$m high and the profile are not binary. The peaks that appear in the cut view are artifacts produced during the AFM measurements.

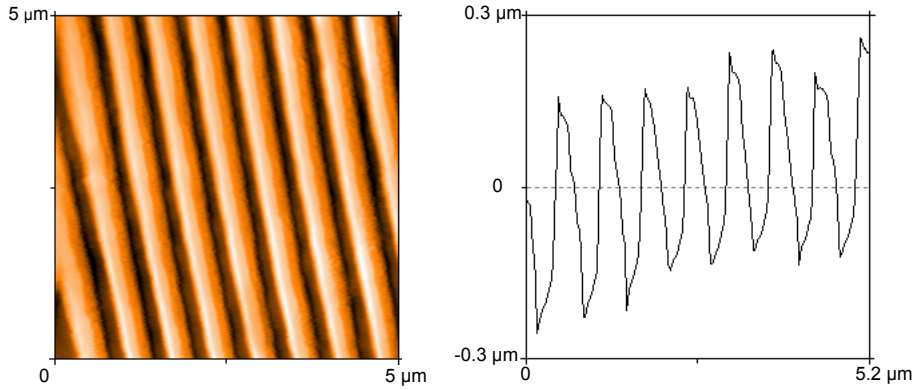

Figure 5.4: AFM measurement of a replicated grating with period $d = 600$ nm and height $h \approx 350$ nm.

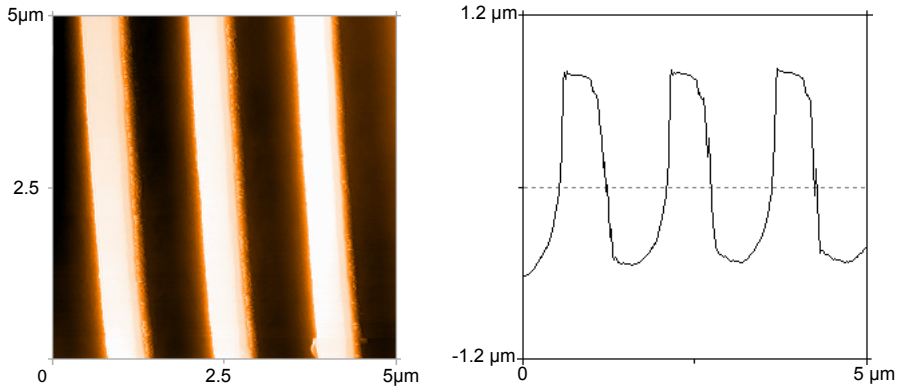

Figure 5.5: AFM measurement of the grating with period $d = 1.5\,\mu$m and height $h \approx 1.3\,\mu$m.

The characteristics of the samples studied are outlined in Tab. 5.1. Samples n°1, 3 and 5 are the reference multilayer Bragg reflectors. These samples are characterized for specular reflection in Chap. 4.3. In Fig. 5.6, we show a SEM image of a multilayer sample with a 1.5 μm period grating. One identifies the grating on top and the border between the multilayer and the grating. The dark region between the Bragg multilayer and the substrate shows that the organic part was separated from the substrate during the sample preparation

Sample	Bragg mirror layers	Reflectivity max.	Grating period	Grating height
1	10, PVA first	570 nm	-	-
2	10, PVA first	570 nm	1.5 μm	1.3 μm
3	9, PVK first	570 nm	-	-
4	9, PVK first	570 nm	600 nm	350 nm
5	21, PVK first	450 nm	-	-
6	21, PVK first	450 nm	1.5 μm	1.3 μm

Table 5.1: Description of the selected samples. Samples n° 1, 3 and 5 are reference Bragg multilayers. Samples n° 2, 4 and 6 have the same Bragg multilayer as samples n° 1, 3 and 5, respectively, but with a grating replicated on top.

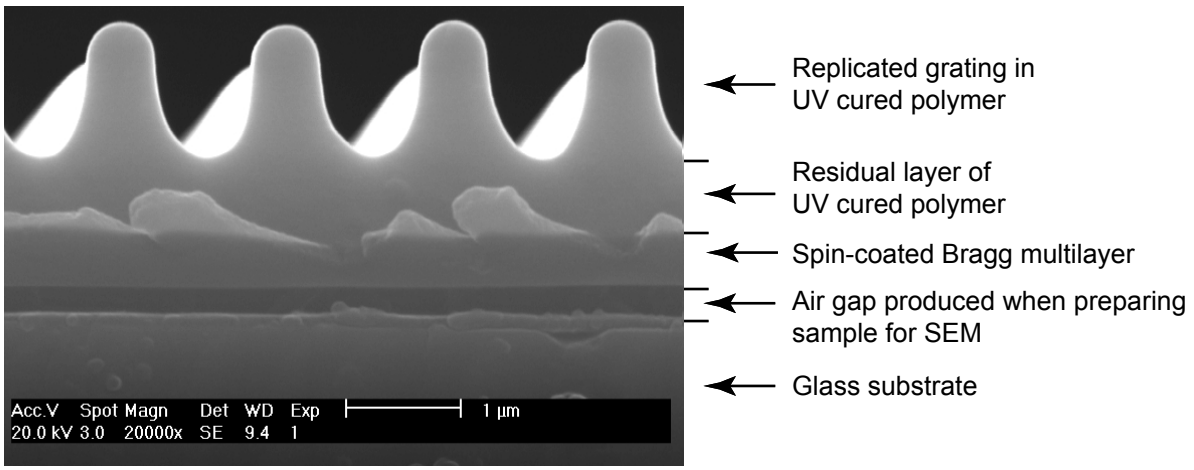

Figure 5.6: SEM picture of a cleaved sample. One sees the grating on top and the border between the multilayer structure and the grating. The low contrast of the two polymers in the Bragg multilayer does not allow to see the details of the multilayer.

for SEM. The grating shape is not binary. A residual layer of UV glue forms a layer between the grating and the Bragg reflector. On this image, this layer thickness is about 700 nm.

5.4 Measurement setup

To characterize the sample we use a collimated illumination and a measurement setup providing spectral reflection measurements for various incident angles and conical angles (goniometer). This setup is described in Chap. 4.2. Two sets of measurements were done. The first measurements were done using a fixed angle of 30° between the incident light and the direction of observation. The sample was rotated from an incident angle $\theta_i = 15°$, corresponding to specular reflection, to $\theta_i = 90°$ (see Figs. 5.7(a) and 5.7(b)). This measurement correspond to a set eye-point source illumination system where the observer rotates the sample in its hand. It permits to have a description of what effects are perceived from an observer. In a second time, the specular reflection of the samples were measured (see Fig. 5.15(a)). For each incident angle the detector is rotated to follow the specular reflection

beam (zero diffraction order). The measured spectra depend on the spectrum of the illumination and on the spectral characteristics of the optical elements between the sample and the detector (lens, fiber, spectrometer spectral sensitivity). We normalized each measurement by the spectrum of the lamp. Due to this normalization, some artefact or shifts can appear in the spectral region where the signal of the lamp is weak or not stable in time.

5.5 Observer-like optical measurement

To record the reflected light from the samples according to what one sees when we turn the sample in the hands with a fixed light source like the sun or an electric bulb, we set up this non-standard measurement. This measurement was performed using a fixed angle of 30° between the incident light and the direction of observation. The sample was rotated from an incident angle $\theta_i = 15°$, corresponding to the specular reflection, to $\theta_i = 90°$. The

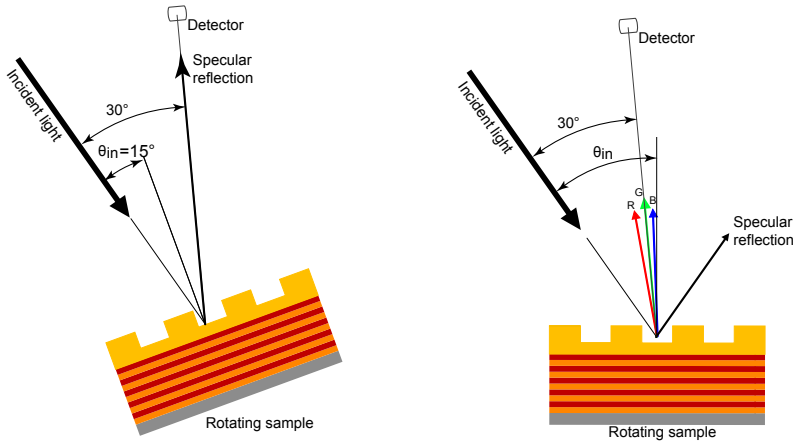

Figure 5.7: Measurement geometry. The measurements were performed using a fixed angle of 30° between the incident light and the direction of observation. (a) The sample was rotated from an incident angle $\theta_i = 15°$, corresponding to specular reflection, to a maximum of $\theta_i = 90°$. (b) Illustration of the case when the grating order $m = -1$ is measured.

geometry is illustrated on Figs. 5.7(a) and 5.7(b). The measurement scans the different (negative) grating diffraction orders when the sample is turned. Measured values are taken for incident angles with a resolution of one degree, giving step-like data when plotted. The measurement results for the samples n°2, n°4 and n°6 are shown in Figs. 5.8(a), 5.11(a) and 5.13(a). In Fig. 5.8(a), for an incident angle $\theta_i = 15°$, at the leftmost position one observes the specular reflected spectrum. At this angle, the maximum of intensity is measured for wavelengths between 550 and 600 nm. That corresponds to the wavelength of reflection of the Bragg mirror. Between $\theta_i = 40°$ and 50°, the first diffracted order causes reflection. The corresponding wavelength is around 550 nm that fits with the wavelength of reflection of the Bragg mirror. Figure 5.8(b) shows the corresponding color coordinates, calculated for each incident angle, using an illuminant D65 as a light source. A maximum intensity can be observed at $\theta_i = 44°$ in the luminance plot (see Fig. 5.9). The first grating order contributes

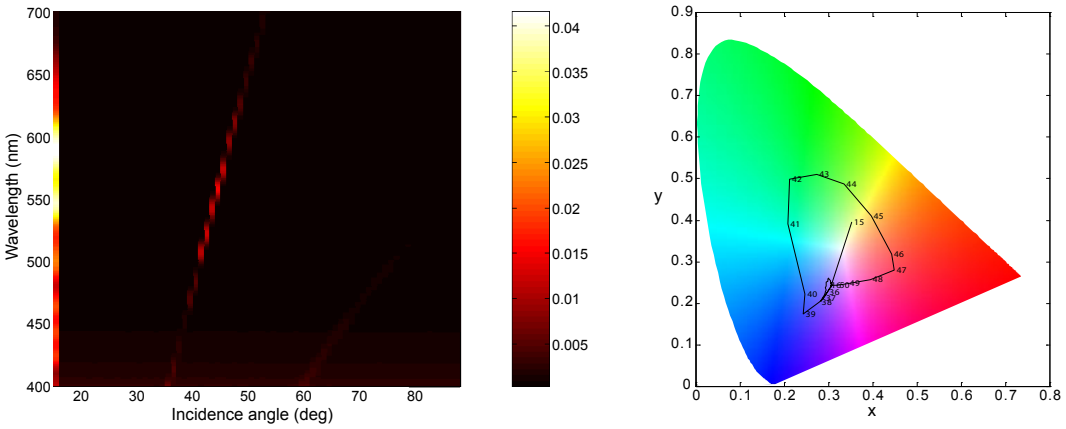

(a) (b)

Figure 5.8: (a) Reflection as a function of the angle of incidence using a fixed angle of 30° between the incident light and the direction of observation. The multilayer Bragg reflector has a reflection band centered at 570 nm with 4 PVA layers and 5 PVK layers. The thicknesses are ≈ 91 nm (PVA) and ≈ 83 nm (PVK). The grating period is $d = 600$ nm (sample n°4). (b) Color coordinates for this measurement.

to a scan into the color coordinates from blue for incident angle around $\theta_i = 38°$ to 40°, to green for incident angle around $\theta_i = 42°$ to 43° and finally to red for incident angle around $\theta_i = 46°$ to 47°. Note that the luminance is limited to a very narrow angular range (Fig. 5.9). Photos in Fig. 5.10 were taken at different angles and illustrate the different color shade that can be seen on the sample with a daylight illumination. For a 600 nm grating, only one grating order can contribute to the reflectivity. With a larger grating period, the number of grating orders will increase. A sample with the same multilayer Bragg reflector but with a grating period of 1.5 μm instead of 600 nm, is measured and results are in Fig. 5.11(a). Since the total incident light is distributed in a higher number of grating orders, the reflection efficiency of particular orders are reduced. In Fig. 5.11(a), for an incident angle $\theta_i = 15°$, one sees the specular reflected spectrum. At this angle, the maximum intensity is measured for wavelengths around 470 nm, which does not correspond to the wavelength of the maximum reflection of the Bragg mirror. One can also see that the maximum intensity of the different grating orders does not fit perfectly with the wavelength of reflection of the Bragg mirror. In particular the grating order $m = -4$ has two maximum intensities at around $\theta_i = 55°$ and 70°, with a wavelength around 450 nm and 600 nm, respectively. This gives indication of the contribution of different grating orders in the measurement (see discussion in section 5.2). Figure 5.11(b) shows the corresponding color coordinates. With increasing incident angle, each grating order contributes to a spectral scan from blue to green and finally to red. For the first order, we can see that the points are situated close to the border of the color diagram where the spectral color are found. That means the colors are quite pure. For the larger angles θ_i, the points in the diagram are situated more in the center, meaning that the colors are less saturated. We can see that for large angles, the contribution of different diffracted orders are added. For example at $\theta_i = 55°$, the total contribution is the sum of the

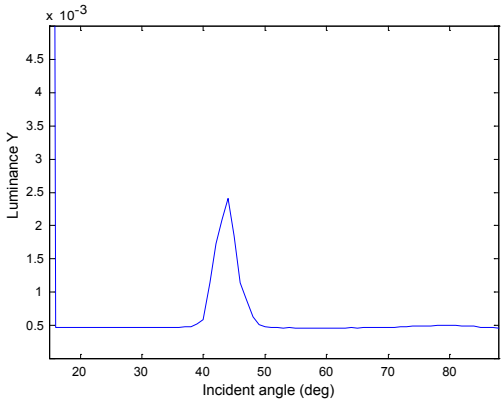

Figure 5.9: Luminance as a function of sample angle for the system given in Fig. 5.8 (sample n°4).

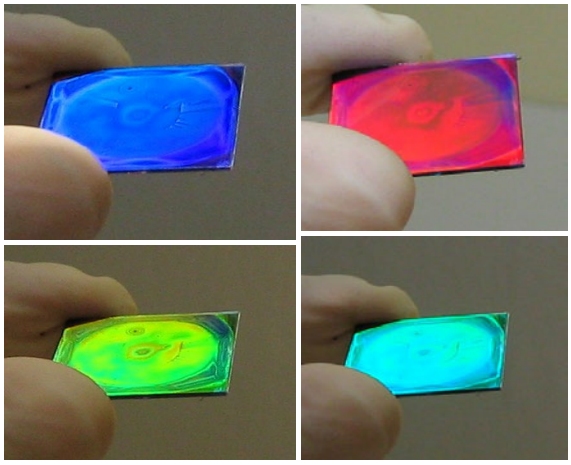

Figure 5.10: Photos of a multilayer Bragg reflector with a top grating taken at different angle of incidence (sample n°4).

order $m = -4$ and $m = -3$ at around 450 nm and 600 nm, respectively. In the luminance plot (see Fig. 5.12) one finds maxima of intensity at $\theta_i = 27°$, 40°, 51° and 72° . The colors at these angles are orange (27°), red (40°), green (51°) and pale red (72°). The width of these peaks become larger for larger incident angles, that is due to bigger dispersion and the contribution of different grating orders. A sample with the same grating period but a different multilayer Bragg reflector with a reflection band at 450 nm instead of 570 nm was also investigated. The Bragg reflector efficiency has been increased by taking a total number of 21 layers. In Fig. 5.13(a), for an angle $\theta_i = 15°$, one sees the specular reflected spectrum. The maximum of intensity is measured for wavelengths between 400 and 450 nm. For the different grating orders, one can see that the maximum of the reflection is always around 450 nm. In Fig. 5.13(b), color coordinates are situated in the blue region, that means the sample appears blue for a wide range of angles.

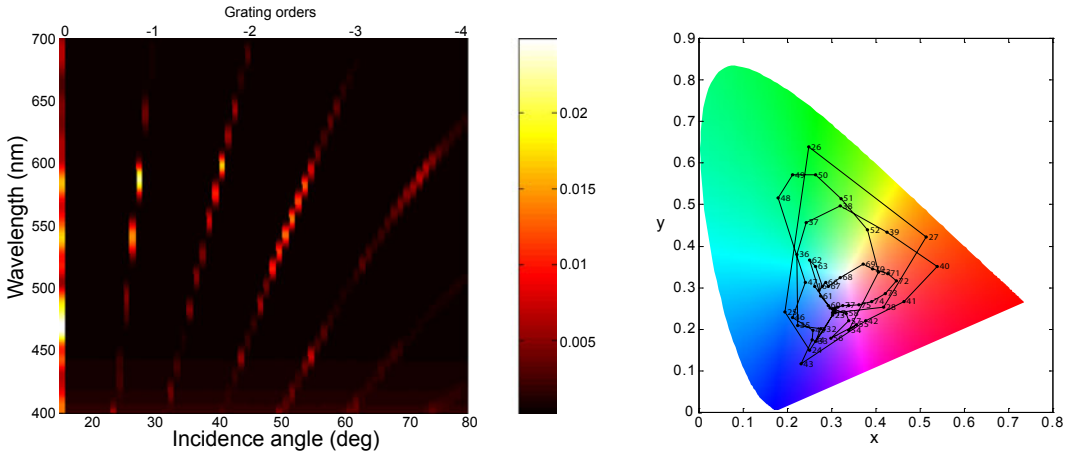

(a) (b)

Figure 5.11: (a) Reflection as a function of the angle of incidence using a fixed angle of 30° between the incident light and the direction of observation. The multilayer Bragg reflector has a reflection band centered at 570 nm with 5 PVA layers and 5 PVK layers. The thicknesses are ≈ 91 nm (PVA) and ≈ 83 nm (PVK). The grating period is $d = 1.5\,\mu$m (sample n°2). (b) Color coordinates for this measurement.

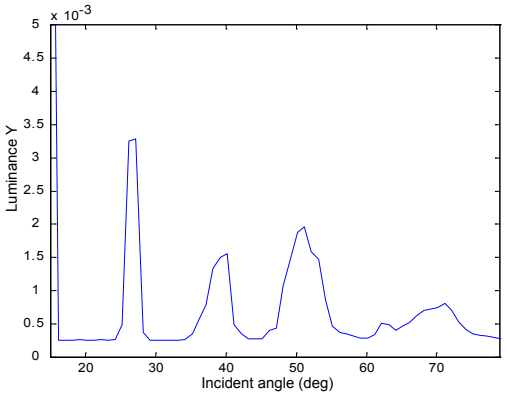

Figure 5.12: Luminance as a function of sample angle for the system given in Fig. 5.11 (sample n°2).

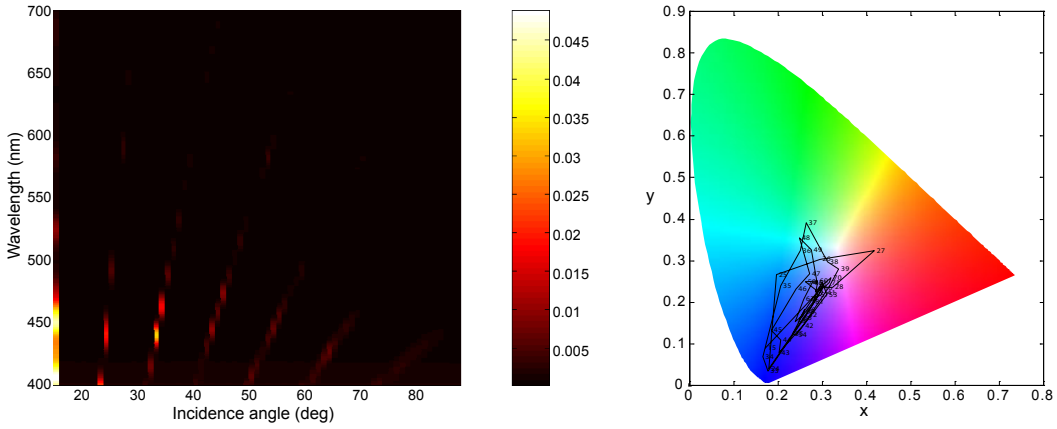

(a) (b)

Figure 5.13: (a) Reflection as a function of the angle of incidence using a fixed angle of 30° between the incident light and the direction of observation. The multilayer Bragg reflector has a reflection band centered at 450 nm with 10 PVA layers and 11 PVK layers. The thicknesses are $\approx 70-75$ nm (PVA) and ≈ 65 nm (PVK). The grating period is $d = 1.5\,\mu$m (sample n°6). (b) Color coordinates for this measurement.

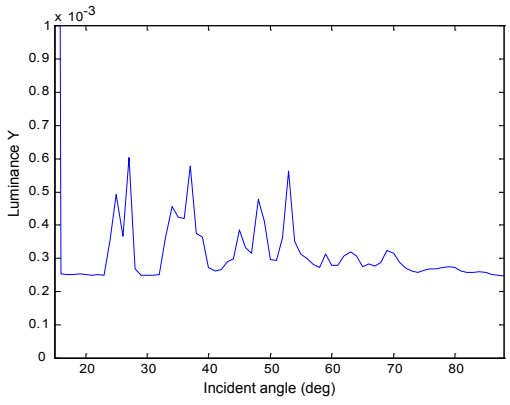

Figure 5.14: Luminance as a function of sample angle for the system given in Fig. 5.13 (sample n°6)

5.6 Specular reflection measurement

To study the interference effects and the dependence on the different parameters (thickness of the intermediate layer between the Bragg multilayer and the grating, grating shape, height and period, Bragg mirror spectral response), the angular dependent specular reflection of the samples was measured. The specular reflection as a function of the incidence angle for

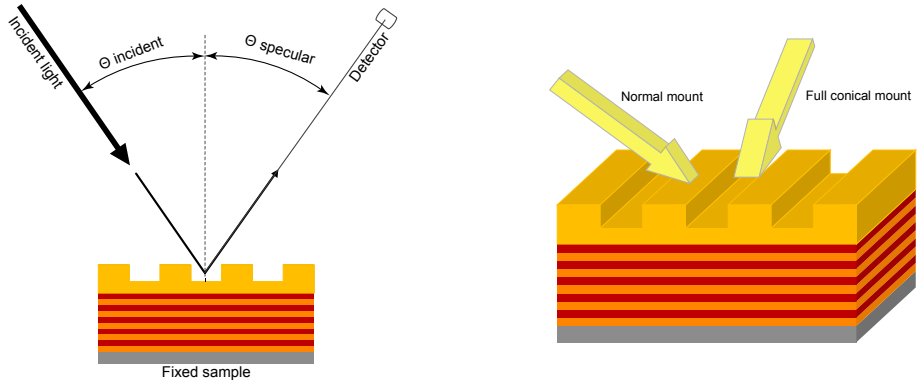

(a) (b)

Figure 5.15: (a) Specular reflection measurement. For each incident angle the detector is rotated to follow the specular reflection spot. The sample was rotated from 4° to 40°. (b) Illustration of the sample illuminated in the two configurations: normal and full conical mount.

normal mount (in plane component of incident k vector perpendicular to the grooves) and full conical mount (in plane component of incident k vector parallel to the grooves) were measured. The two different mounts are illustrated in Fig. 5.15(b).
For the full conical mount, the measurement results for the samples n°2 and n°4 are shown in Figs. 5.16(a) and 5.16(b).
We can see a difference between this case and the sample with Bragg mirror only (Fig. 4.6(a)). One sees a splitting in the reflection band due to the top layer. This is particularly visible in Figs. 5.16(a) and 5.16(b) for an incident angle around $\theta_i = 25°$ and $\theta_i = 35°$, respectively, where two reflection bands are visible. These two bands have a smaller reflection width in wavelength and a maximum reflection wavelengths just over and below the original reflection wavelength of the Bragg reflector alone. The reflection bands have also a reflection efficiency smaller than in the case without the grating. This is due to fraction of light being diffracted in grating orders. Only the grating order 0 is measured in the specular beam. In the full conical mount, the grating layer can be seen as a flat layer with an average layer thickness. Always the same fraction of the incident light is lost in the grating orders since the light has no component in the direction of the grating vector for any full conical angle.
For the normal mount, the measurement results for the samples n°2 and n°4 are shown in Figs. 5.17(a) and 5.17(b).
The specular reflection measurements for the Bragg mirror alone (see Chap. 4.3) and sample with Bragg mirror and grating in full conical mount were taken as a reference to see how the reflection in normal mount is modified by the grating. For all samples, by comparing with full conical mount measurement, one can observe several losses of specular reflection

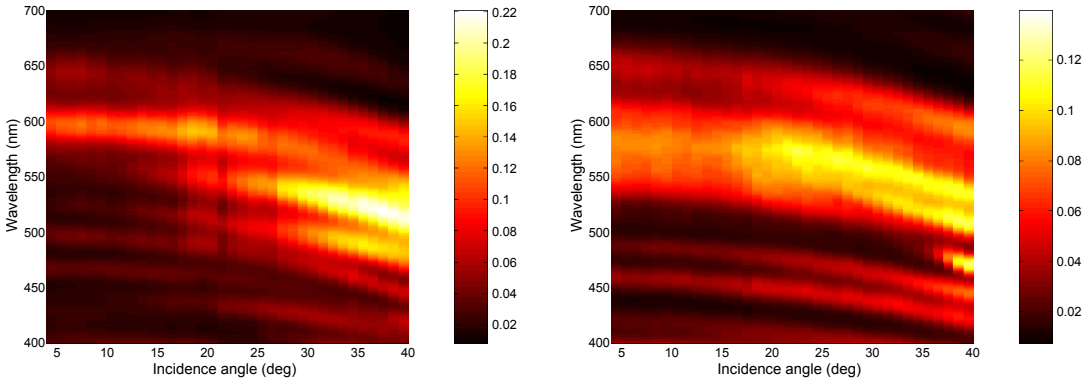

(a) (b)

Figure 5.16: (a) Specular reflection measurement in full conical mount. The multilayer Bragg reflector has a reflection band centered at 570 nm with 5 PVA layers and 5 PVK layers. The thicknesses are ≈ 91 nm (PVA) and ≈ 83 nm (PVK). The grating period is $d = 1.5\,\mu$m (sample n°2).(b) The multilayer Bragg reflector has a reflection band centered at 570 nm with 4 PVA layers and 5 PVK layers. The thicknesses are ≈ 91 nm (PVA) and ≈ 83 nm (PVK). The grating period is $d = 600$ nm (sample n°4).

for particular angles. For sample n°2 and n°4, the global effect on luminance can be seen in Figs. 5.18(a) and 5.18(b) where the minima of intensity for incident angle are around $\theta_i = 14°$ and 33° and $\theta_i = 11°$ and 27°, respectively. We still see the reflection bands and the band structures are conserved. This is visible when comparing Figs. 5.17(a) and 5.17(b) with Figs. 5.16(a) and 5.16(b), respectively. Nevertheless, for these angles, the reflection bands are clearly diminished. The reflectivity is lowered by interferences due to reflection of the multilayer structure and the different orders of the grating. A rigorous simulation for sample n°2 and n°4 is given in Figs. 5.19(a) and 5.19(b). Due to the technology used to fabricate the samples, the dimension of the intermediate layer is not known with precision. We had to make multiple simulations to find a good agreement between measurement and simulation. The simulation for the sample n°4 seems in better agreement with the measurements. It is also due to a smaller grating period, giving a reduced number of grating orders.

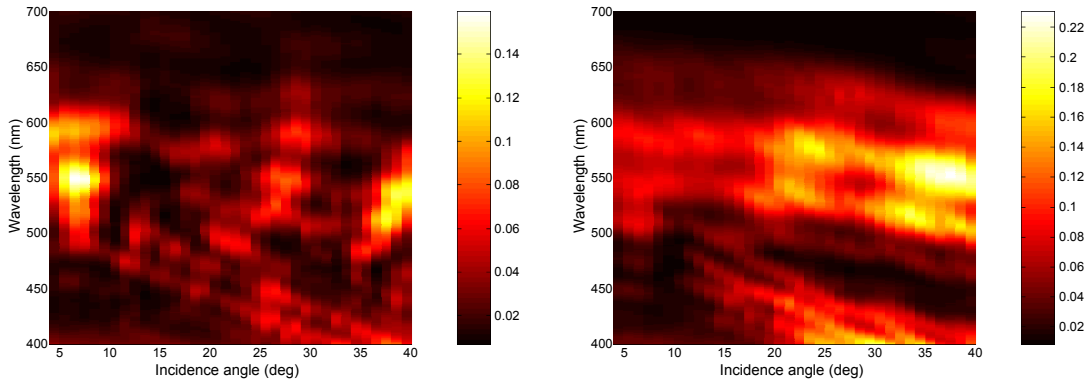

(a) (b)

Figure 5.17: Specular reflection measurement in normal mount. (a) The multilayer Bragg reflector has a reflection band centered at 570 nm with 5 PVA layers and 5 PVK layers. The thicknesses are $\approx$ 91 nm (PVA) and $\approx$ 83 nm (PVK). The grating period is $d = 1.5\,\mu$m (sample n°2). (b) Specular reflection measurement in normal mount. The multilayer Bragg reflector has a reflection band centered at 570 nm with 4 PVA layers and 5 PVK layers. The thicknesses are $\approx$ 91 nm (PVA) and $\approx$ 83 nm (PVK). The grating period is $d = 600$ nm (sample n°4).

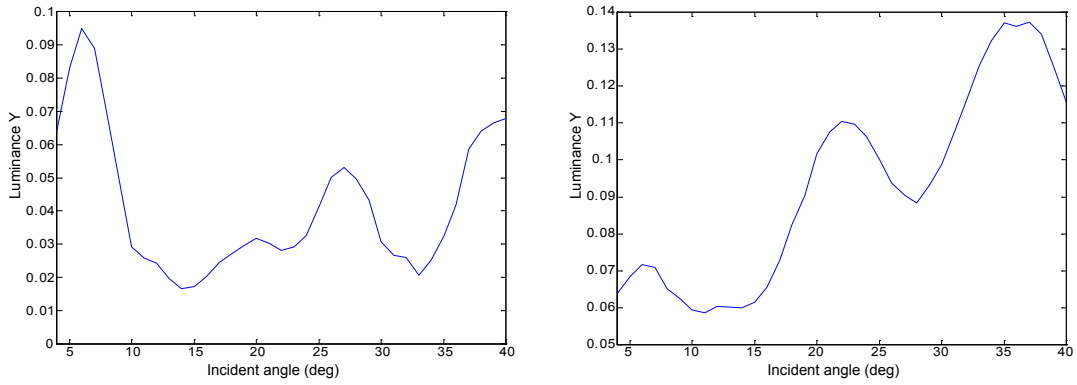

(a) (b)

Figure 5.18: (a) Luminance as a function of sample angle for the system given in Fig. 5.17a (sample n°2). (b) Luminance as a function of sample angle for the system given in Fig. 5.17b (sample n°4).

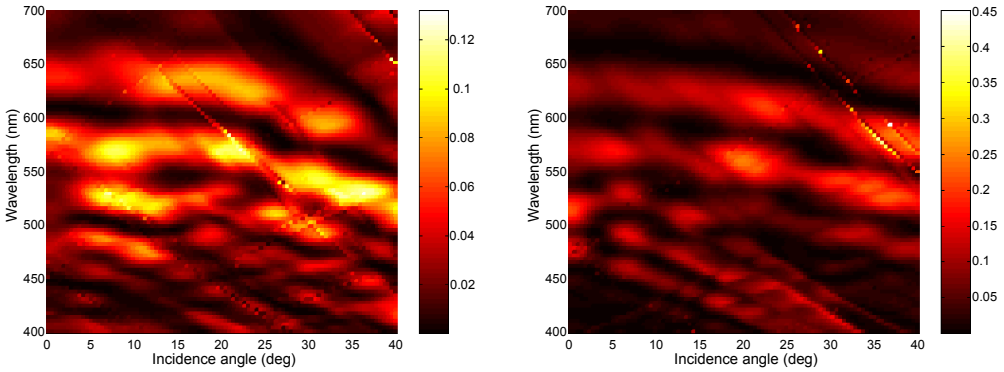

(a) (b)

Figure 5.19: Simulation of reflection as a function of sample angle. (a) The multilayer Bragg reflector has a reflection band centered at 570 nm with 5 PVA layers and 5 PVK layers. The thicknesses are ≈ 91 nm (PVA) and ≈ 83 nm (PVK). The grating period is $d = 1.5\,\mu$m (sample n°2). (b) The multilayer Bragg reflector has a reflection band centered at 570 nm with 4 PVA layers and 5 PVK layers. The thicknesses are ≈ 91 nm (PVA) and ≈ 83 nm (PVK). The grating period is $d = 600$ nm (sample n°4).

5.7 Parameters influence on reflection in simulation

In order to understand the effects of the different parameters of the selected samples on the reflection, rigorous optical simulations were done. The simulation are based on a rigorous coupled wave analysis as described in Chap. 2. We began by the specular reflection case. In order to understand the contributions of the different parameters , we modeled a Bragg mirror with a grating on top. A square grating was chosen for sake of simplicity. We first chose a total number of 21 layers with refractive indices $n_1 = 1.56$ and $n_2 = 1.72$. These values correspond to the refractive indices of the two polymers used in this work to fabricate the multilayer Bragg reflector. Figures 5.20(a) and 5.20(b) correspond to the zero order

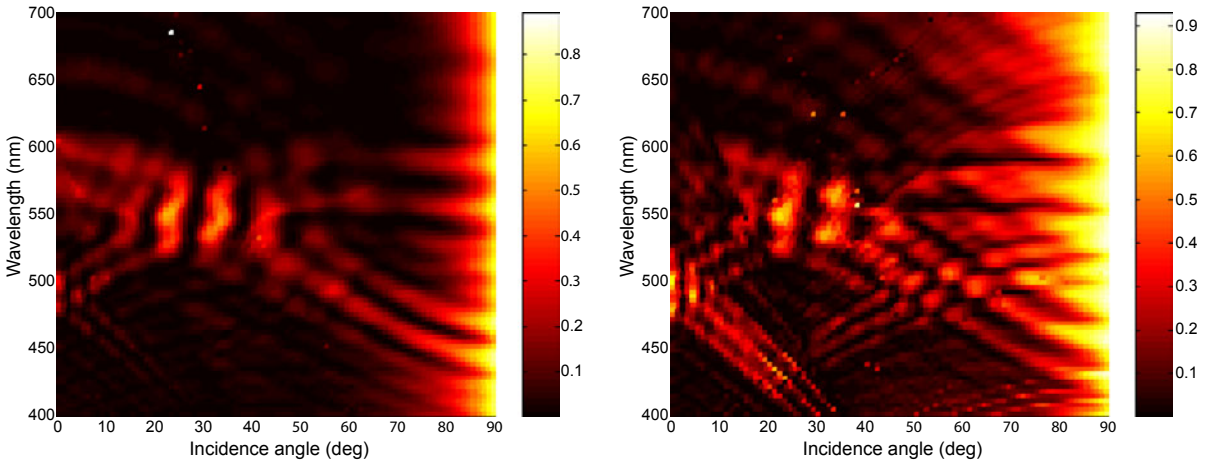

(a) (b)

Figure 5.20: Simulation of the zero order reflection for a Bragg multilayer reflector at 570 nm with 21 layers on a glass substrate ($n_1 = 1.56$, $n_2 = 1.72$), with a 2 μm optical adhesive top layer and grating period $d = 600$ nm with grating height $h = 400$ nm. (a) TM component; (b) TE component.

reflection simulation, for the TM and TE components, respectively, for a Bragg multilayer reflector with reflection wavelength centered at 570 nm, with 21 layers on a glass substrate ($n_L = 1.56$, $n_H = 1.72$), with a 2 μm optical adhesive top layer, grating period $d = 600$ nm and with grating thickness $h = 400$ nm. One observes that for incident angle around 23°, 34° and 42° the reflection is maximum. On the other hand, there are angle around 18°, 27° and 38° where the reflection is very low. The reflection band is limited for wavelength between 500 nm and 600 nm.

One sees that the the small difference of refractive index between the two polymers restricts the width of the reflection band and the maximum reflectivity. To have a larger reflection band, a high reflection efficiency and in order to better see the effects of the different parameters, we model the same sample but change the higher refractive index material to $n_H = 3$. The influence of the reflection width of the Bragg mirror can be seen when comparing Fig. 5.20(a) for the sample with refractive index $n_L = 1.56$, $n_H = 1.72$ and Fig. 5.21(b) for the sample with refractive index $n_L = 1.56$, $n_H = 3$. As excepted the wavelength width where there is specular reflection is increased. One observes also an increase of the width

of angular region where the reflection is high. As discussed earlier, the simple model drawn in Chap. 5.2 was neither taking into account the grating efficiency, given by the shape and height of the grating, nor the thickness of the residual layer between the multilayer Bragg mirror and the grating. For this reason, these two parameters are studied below. The

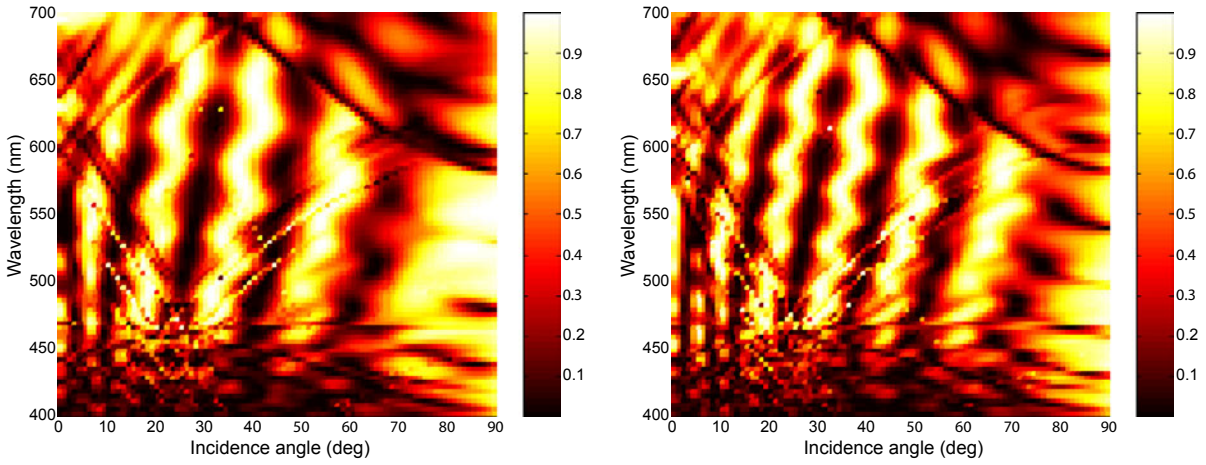

(a) (b)

Figure 5.21: Simulation of the zero order reflection for a Bragg multilayer reflector at 570 nm with 21 layers on a glass substrate ($n_1 = 1.56$, $n_2 = 3$), with two different thicknesses for the optical adhesive top layer: (a) $H = 1.5\,\mu$m and (b) $H = 2\,\mu$m. The grating period is $d = 600$ nm and grating height $h = 400$ nm.

thickness of the residual layer between the multilayer Bragg mirror and the grating was first modified with the other parameters fixed. The influence of a change in this layer thickness can be seen in an example illustrated in Figs. 5.21(a) and 5.21(b). These simulations show the zero order reflection for a Bragg multilayer reflector at 570 nm with 21 layers on a glass substrate ($n_L = 1.56$, $n_H = 3$), with two different thicknesses, $H = 1.5\,\mu$m and $2\,\mu$m, for the residual layer (optical adhesive layer). The grating period is $d = 600$ nm and the grating height $h = 400$ nm. One sees that there is an increased number of angles with constructive and destructive interferences with a thicker residual thickness. By changing this layer thickness, one modifies the number of optical modes that can couple inside and their propagation characteristics. This layer can be seen as a waveguide for a given range of wavelength, also influenced by the multilayer Bragg mirror and the grating. The grating allows us to couple a part of the incident light inside this layer. Different effects of light coupling in a waveguide are approached in Chap. 7.

The second parameter to be varied was the grating height. The influence of the grating height can be seen in Figs. 5.22(a) and 5.22(b). These simulations show the zero order reflection for a Bragg multilayer reflector at 570 nm with 21 layers on a glass substrat ($n_L = 1.56$, $n_H = 3$), with two different grating heights $h = 200$ nm and $h = 400$ nm. The grating period is $d = 600$ nm and the residual layer (optical adhesive layer) is $H = 1.5\,\mu$m. One sees that the region with a very low reflection efficiency (dark zone) are less present for the thinner grating. We know that the grating height change the efficiency of the grating. Therefore the

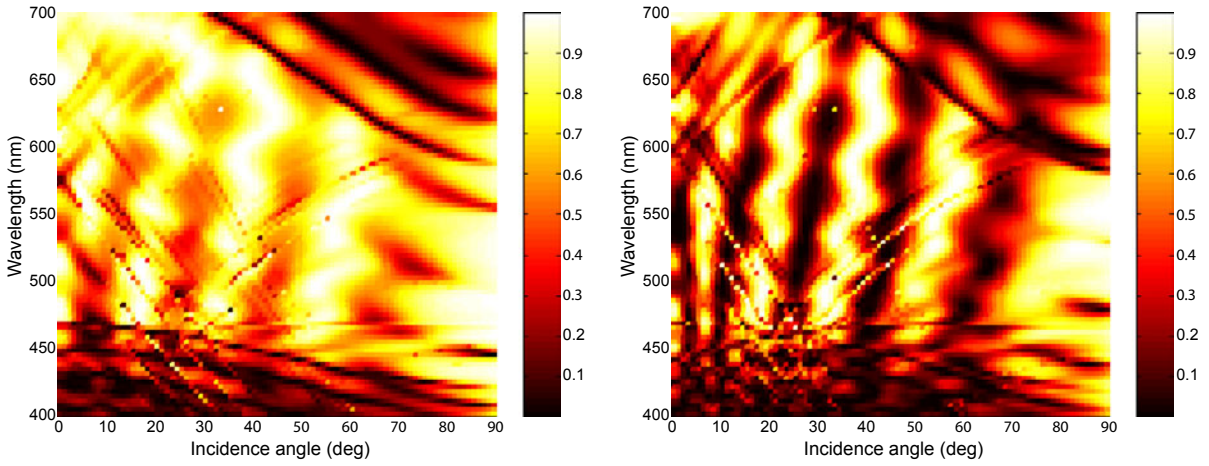

(a) (b)

Figure 5.22: Simulation of the zero order reflection for a Bragg multilayer reflector at 570 nm with 21 layers on a glass substrate ($n_1 = 1.56$, $n_2 = 3$) with two different heights for the grating: (a) $h = 200\,\text{nm}$ and (b) $h = 400\,\text{nm}$. The grating period is $d = 600\,\text{nm}$ and the optical adhesive top layer is $H = 1.5\,\mu\text{m}$.

total incident intensity will be distributed in a different way in the different grating orders when the grating height is changed. When the specular reflection falls, one can see that the reflected intensity in superior orders increases.

5.8 Outlook

We fabricated successfully low cost polymeric multilayer Bragg structures on a glass substrate and replicated diffractive gratings on top to produce artificial visual color effects. We measured the angular dependent reflectivity with and without grating. We could see that the combination of the multilayer Bragg mirror and grating diffraction gives color effects that cannot be produced with a single optical element. These effects can be explained by the coupling of different grating orders and the Bragg reflection band. A simple model could illustrate the different contributions of a specific reflected order. A complete description of the samples can not be given only with this simple model. Different rigorous optical simulations allow us to understand the contribution of the variation of the different parameters. The rigorous model shows that the number of angular region where we found a loss of reflection depend on the layer thickness H (see Fig. 5.2) and the contrast between the different region with high or low reflectivity can be tuned with the grating height, that changes the different grating orders efficiency.

Chapter 6

Interference stacks with micro-structured surfaces

Different micro-optical elements were replicated on multilayer Bragg reflector to produce visual color effects. The idea to combine micro-optical elements and multilayer Bragg reflectors is inspired directly from Nature. Some SEM pictures found in [8] show insects using this combination to produce iridescent colors. The different replicated micro-optical elements used were:

- microlenses with 145 μm diameter and 20 μm height
- microlenses with 32 μm diameter and 16 μm height
- concave microlenses with 250 μm diameter and 20 μm height
- prisms with 50 μm period and 25 μm height (commercially available 45° periodic prisms)
- replicated diffusers (commercially available)

Here, the challenge was to combine optical elements with nanometer sizes ($\lambda/4$ layers from the multilayer Bragg reflector) with micro- or macro-optical elements such as microlens and microprism arrays. The microlenses and microprisms allowing to change the angular spectrum of the light, shifts and combinations of the reflecting properties of the multilayer Bragg reflector at various angle were sought.

6.1 Measurement setup

To characterize the sample we used the measurement setup described in Chap. 4.2. The measurements were performed using a fixed angle of 30° between the incident light and the direction of observation as described in Chap. 5.5. The geometry is illustrated in Figs. 5.7(a) and 5.7(b). The sample was rotated from an incident angle $\theta_i = -10°$, to $\theta_i = 45°$. The angle $\theta_i = 15°$ corresponds to the specular reflection. This measurement corresponds to what an observer sees if he/she rotates the sample in its hands with a fixed point source illumination.

6.2 Characterization of the multilayer Bragg reflectors

The fabrication of the samples is described in details in Chap. 3. To simplify the study, the multilayer Bragg reflectors were fabricated at the same time and with the same layer thickness for all the samples studied in this chapter. They are formed of quarterwavelength stacks of PVK and PVA layers. The multilayer Bragg reflectors are formed of a total of 5 periods, 5 PVA layers and 6 PVK layers. The first layer on the glass substrate is a PVK layer. The layer thicknesses are around 90 nm and 80 nm, for PVA and PVK respectively. The fabricated multilayer Bragg reflectors have their maximum of reflection around 570 nm at normal incidence. For incidence angles θ_i between 4° to 40°, we measured the specular reflection. The measurement geometry is illustrated in Fig. 4.5. The results for a multilayer Bragg reflector are shown in Fig. 6.1(a). A reflection band appears. The center wavelength of

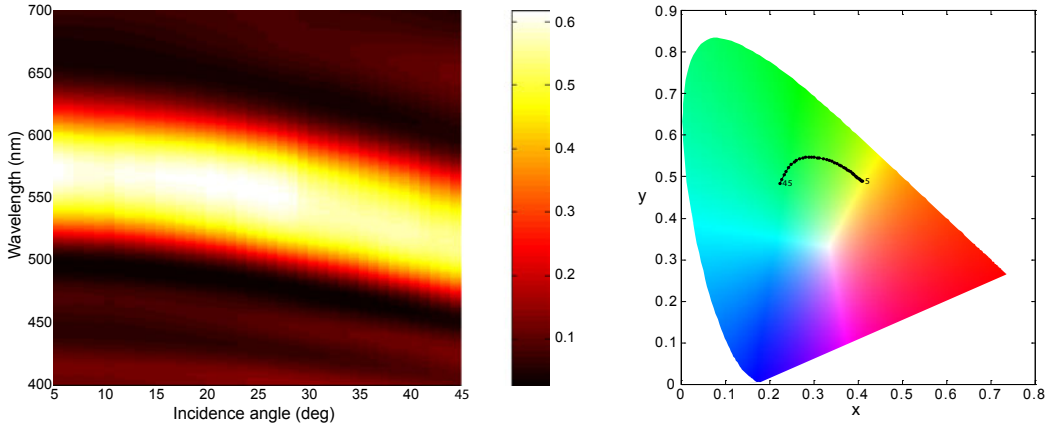

(a) (b)

Figure 6.1: (a) Specular reflection measurement for multilayer Bragg reflector on glass substrate with a reflection band centered at $\lambda = 570$ nm, with 6 PVK layers and 5 PVA layers. The thicknesses are ≈ 90 nm (PVA) and ≈ 80 nm (PVK). (b) Color coordinates in the CIE chromacity diagram.

the reflection band changes for larger angles of incidence and shows a cosine-like dependence as a function of the incident angle θ_i. The maximum reflectivity is at 570 nm for normal incidence. Figure 6.1(b) shows the corresponding calculated color coordinates in the CIE chromaticity diagram when the sample is illuminated by a normalized illuminant D65 that fits the daylight sky spectrum [2]. The color changes from yellow to green. As excepted, shorter wavelengths are reflected when the incident angle is increased.

6.3 Convex microlenses on multilayer Bragg reflectors

Figures 6.2(a) and 6.2(b) show SEM pictures of replicated 150 μm diameter microlenses on multilayer Bragg reflectors and details of the shape of a single lens, respectively. Since the multilayer Bragg reflector is made by spincoating of two different polymer material, it turned to be difficult to prepare the element for the SEM picture. Usually, the samples are scribed on the glass substrate and broken to provide a clean side cut. Here the multilayer

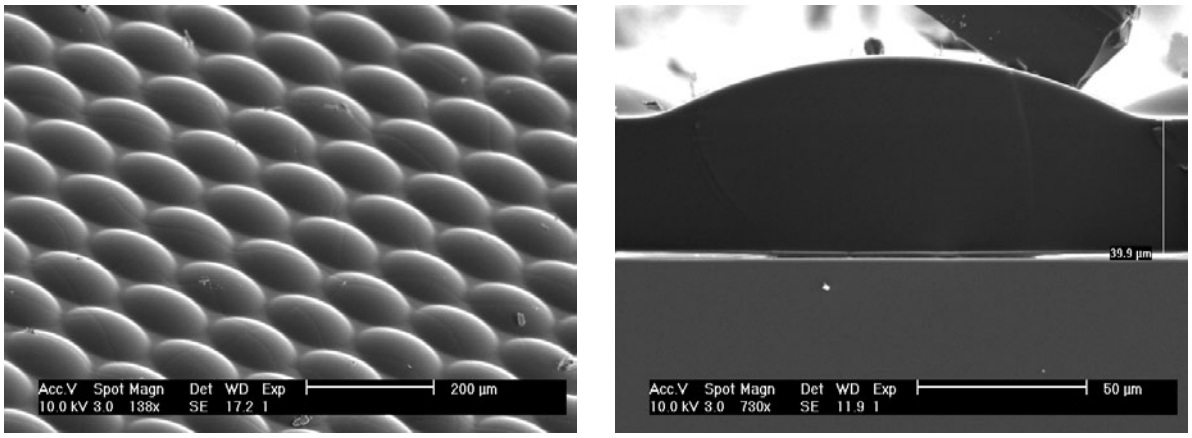

(a) (b)

Figure 6.2: (a) SEM picture of replicated 150 μm diameter microlenses; (b) detail of the shape of a single lens.

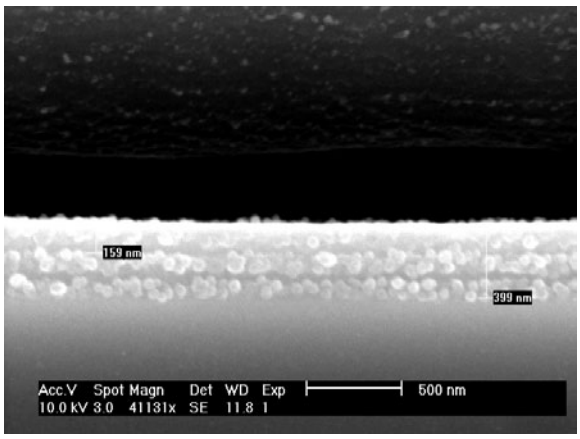

Figure 6.3: SEM picture of a multilayer Bragg reflector made of 5 layers. The sample has been cut under liquid nitrogen condition.

Bragg reflector was too soft and did not break with the glass substrate. For this reason, the sample was put into liquid nitrogen to harden the multilayer Bragg reflector before being broken. The result can be seen in Fig. 6.3. One can see the 5 layers of a multilayer Bragg reflector and some bubbles probably formed into liquid nitrogen. Another attempt to realize a SEM picture of a replicated micro-optical element on top of a polymer multilayer Bragg reflector has been done. This time, the multilayer Bragg reflector and replicated microlens array were removed from the substrate. To do this, we scratched a part of a sample prior dipping it in liquid nitrogen. The resulting stress helped to remove the all plastic sample from the glass substrate. Since the two different polymers used for the multilayer Bragg reflector are not different enough to produce a contrast difference distinguishable on a SEM picture, we had to cut the sample in such a way to get a step like cut surface. The soft sample has been simply cut with a scissor before the SEM measurement. With this method, an image of the polymer Bragg multilayer and replicated microlens array on top could be taken. Figures 6.4(a) to 6.4(e) show a serie of SEM images of a replicated 64 μm diameter

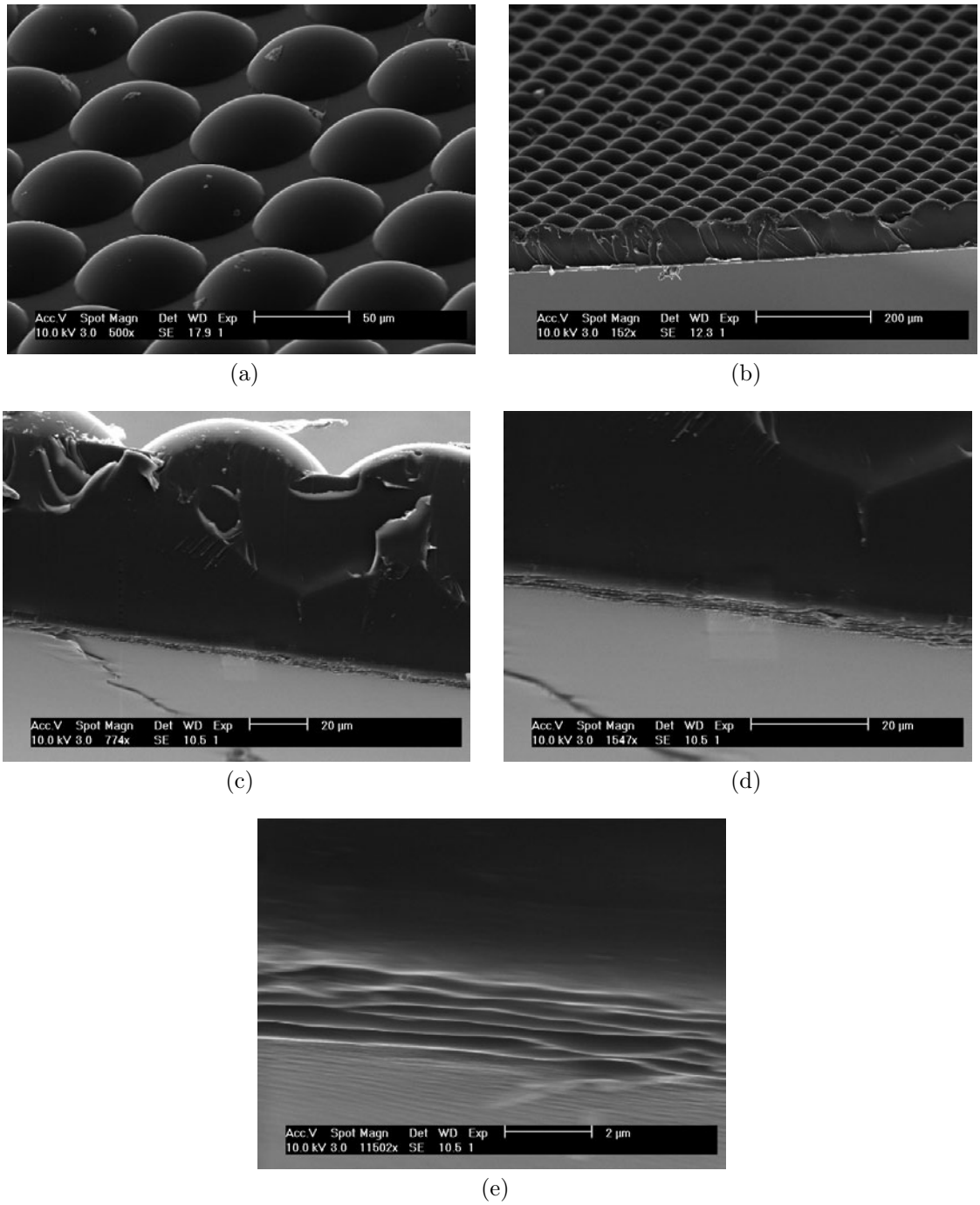

Figure 6.4: SEM measurement of a 64 μm lens replicated on top of a multilayer Bragg reflector: (a) view of the microlens array from top; (b) broad view of the microlens array and cut side of the sample; (c) detail of a single microlens; (d) and (e) details of the multilayer Bragg reflector.

microlens array on a multilayer Bragg reflector. Figure 6.4(a) shows a view of the microlens array from top. Figure 6.4(b) shows a broad view of the microlens array and also the cut side of the sample. The multilayer Bragg reflector is on the bottom of the sample. The layer thickness between the microlens array and the multilayer Bragg reflector is around 60 μm. Figure 6.4(c) shows a detail of a single microlens. Here the multilayer Bragg reflector is

clearly visible on the bottom of the sample. Details of the multilayer Bragg reflector can be seen in Figs. 6.4(d) and 6.4(e).
In short, one will encounter three different configurations for the incoming light on the multilayer Bragg reflector. The three configurations depend on the wavelength of the incident light, on the wavelength of reflection of the reflector and on the incident angle on the reflector. This angle being given by the refraction of the micro-optical element. The first case is for incident light with a wavelength higher than the wavelength of reflection of the multilayer Bragg reflector. This wavelength will not be reflected. The second case occurs when the wavelength of the incident light is the same as the wavelength of reflection of the multilayer Bragg reflector. The light will be reflected at normal incidence and the reflection will rapidly decrease when the incident angle increase. The third case occurs when the wavelength of the incident light is smaller than the wavelength of reflection of the multilayer Bragg reflector. The light will not be reflected at normal incidence. The reflection efficiency will increase when the incident angle increases, will reach a maximum for a given angle and possibly decrease when the incident angle is increased further.
The measurement of the reflection efficiency for a sample with a multilayer Bragg reflector

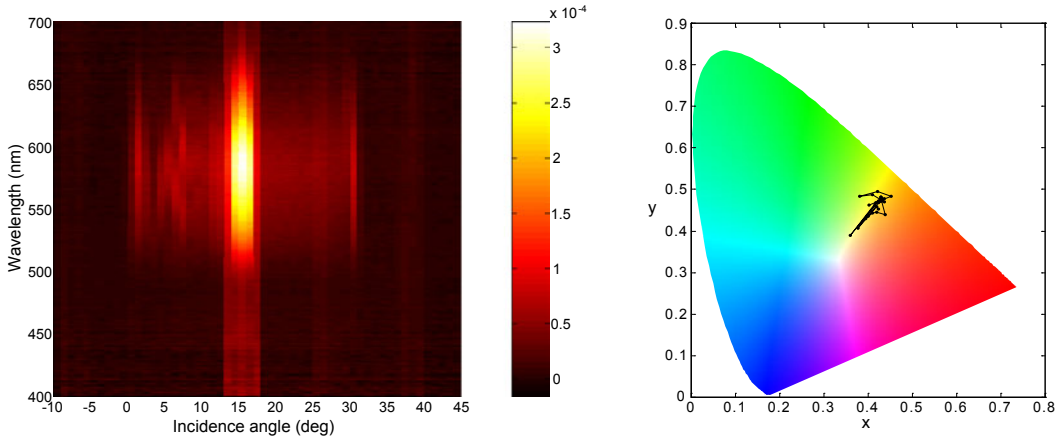

(a) (b)

Figure 6.5: (a) Reflection as a function of the angle of incidence using a fixed angle of 30° between the incident light and the direction of observation. Measurement for a multilayer Bragg reflector with microlenses 145 μm diameter and 20 μm height on top. The multilayer Bragg reflector has a reflection band centered at $\approx$ 570 nm with 5 PVA layers and 6 PVK layers. The thicknesses are $\approx$ 90 nm (PVA) and $\approx$ 80 nm (PVK). (b) Color coordinates in the CIE chromacity diagram for angle 0 to 30°.

as described in Chap. 6.2 and replicated microlens array on top with 145 μm diameter and 20 μm height are shown in Fig. 6.5(a). For an incident angle $\theta_i = 15°$, one observes a maximum of reflected intensity that is the specular reflection. At this angle, the maximum of intensity is measured for wavelengths between 550 and 600 nm. That corresponds to the wavelength of reflection for the multilayer Bragg reflector at normal incident angle. One can see in Fig. 6.6 that the intensity drops rapidly when the angle is different from the specular reflection angle. The interesting features are the plateau of intensity between $\theta_i = 18°$ and

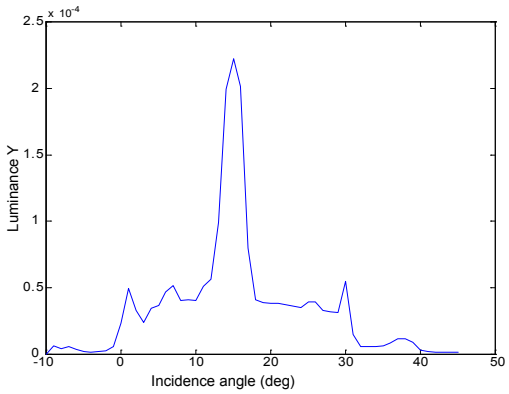

Figure 6.6: Luminance as a function of sample angle for the system given in Fig. 6.5.

30°, the peak of intensity at $\theta_i = 31°$ and a smaller peak of intensity at $\theta_i = 37°$. Between $\theta_i = 31°$ and 37°, the measured intensity is very low. If we look at the sample at these angles, the sample is seen as "grey". So, there is a range of angle where the sample does not reflect light. One can also see in Fig. 6.5(b) that the color of the reflected light stays in a region where the color is yellow. A model of the light propagation in this sample is simulated with a ray tracing software. The geometry is shown in Fig. 6.7(a).

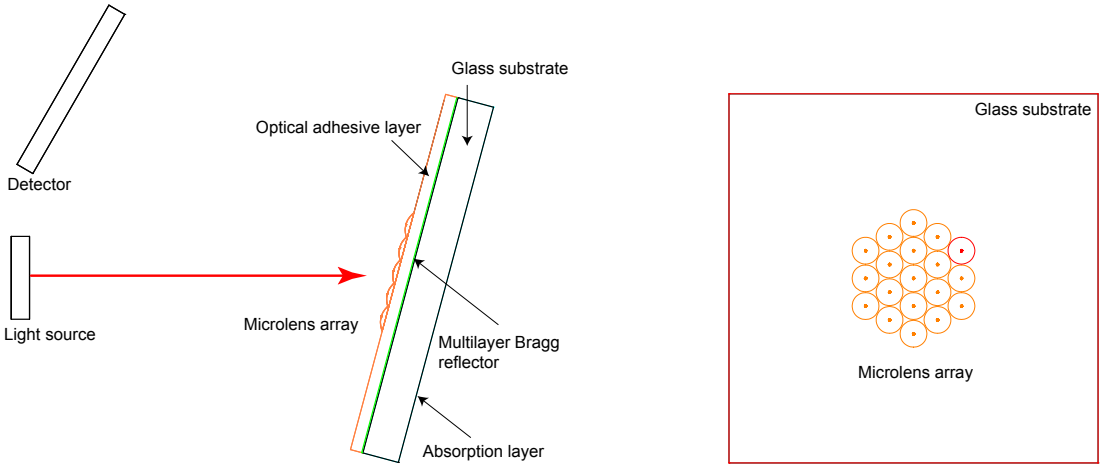

Figure 6.7: (a) Geometry for the ray tracing simulation for microlens array on a multilayer Bragg reflector. The incident angle $\theta_i = 15°$ is illustrated. (b) Illustration of the microlens array spatial arrangement.

To highlight the wavelength selectivity of the sample, a multilayer Bragg reflector with a total of 41 layers was chosen, i.e. 20 periods. The reflection efficiency is 0.96 at normal incidence for wavelength 550 nm. The reflector is placed on a glass substrate. The thickness of the layer between the microstructure and the glass substrate is set to 70 μm. The microlenses have a diameter of 145 μm, a period of 150 μm and 25 μm height. Figures 6.8(a) and 6.8(b) show ray trace simulations for an incidence angle $\theta_i = 0°$, with a threshold fixed at 10 % of

the peak flux, for incidence wavelength of 540 nm and 520 nm, respectively. The threshold fixed at 10 % eliminates all rays with an intensity lower than 10 % of the peak flux. This gives a less crowded image of the simulation. Red rays corresponds to a range from 0.66 to 1 times the incident peak flux. Green corresponds to a range from 0.33 to 0.66 and blue to a range from 0 to 0.33 of the incident peak flux. A detailed analysis done by increasing the

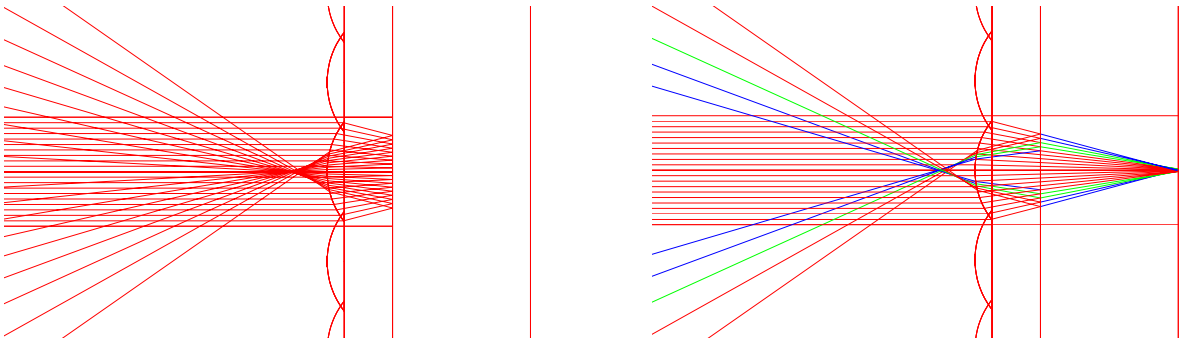

(a) (b)

Figure 6.8: Ray tracing simulation for incident angle $\theta_i = 0°$ with a threshold fixed at 10 % of the peak flux, for incident wavelength of: (a) 540 nm ; (b) 520 nm. The thickness of the layer between the microstructure and the multilayer Bragg reflector is 70 μm. The diameter of the microlenses is 145 μm, the period is 150 μm and the height 25 μm. The multilayer Bragg reflector is made of 41 layers, has a reflection band centered at 550 nm with a maximum efficiency of 0.96 at normal incidence.

threshold value of the rays shows that at normal incidence the major contribution to the reflected intensity comes directly from the multilayer Bragg reflector, i.e. from the regions between the lenses that represent only 15 % of the surface (fill-factor ≈ 0.85). The light goes through the optical adhesive layer without being refracted by a lens and is reflected by the multilayer Bragg mirror. One sees such a ray in Fig. 6.8(a) for the upmost and downmost rays. The second important contribution comes from the light refracted by the lens, reflected by the multilayer Bragg reflector and refracted a second time outside the lens surface. The reflected intensity coming back from the sample will be principally inside this cone. The angle of this cone is defined by the numerical aperture of the lens. Here the focal length of the microlenses is much larger than the distance between microlenses and multilayer Bragg reflector. With larger incident angles, it reduces the possibility for the light to be reflected by the mirror in a neighboring microlens. Figures 6.8(b) and 6.9 show how the angular dependence of the multilayer Bragg reflector interacts with the lens refraction. The light with wavelength at 520 nm, i.e. lower than the wavelength of reflection of the multilayer Bragg reflector, is reflected with a higher efficiency (red rays in Fig. 6.8(b)) when the incident angle on the multilayer Bragg reflector is large. This is the case for rays refracted at the side of the lens. The light at 560 nm (Fig. 6.9), i.e. wavelength larger than the wavelength of reflection of the multilayer Bragg reflector, is reflected with a higher efficiency when the incident angle on the multilayer Bragg reflector is close to normal. This is the case for the rays refracted in the middle of the lens.
Figures 6.10(a) and 6.10(b) show simulations for incident light at 550 nm with a threshold

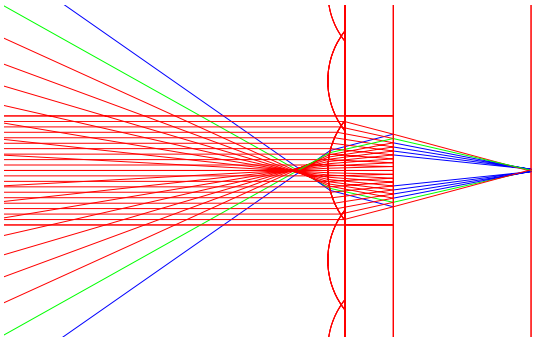

Figure 6.9: Ray tracing simulation for incident angle $\theta_i = 0°$ with a threshold fixed at 10 % of the peak flux, for incident wavelength of 560 nm. The diameter of the microlenses is 145 μm, the period is 150 μm and the height 25 μm. The multilayer Bragg reflector is made of 41 layers, has a reflection band centered at 550 nm with a maximum efficiency of 0.96 at normal incidence.

fixed at 30 % of the peak flux, for incident angle $\theta_i = 30°$ and $\theta_i = 40°$, respectively. Figure 6.10(a) show that for an angle $\theta_i = 30°$, the light refracted at the upper part of the lens is strongly reflected by the multilayer Bragg reflector and refracted again by the upper part of the lens. This part of the light can be measured by the detector at 30° (see measurement geometry in Fig. 6.7(a)). When the incident angle is $\theta_i = 40°$, the light refracted at the upper part of the lens is still strongly reflected by the multilayer Bragg reflector but outside the lens and not any more refracted in the direction of the detector . The intensity measured by the detector drops. This simple schema can explain the limit around the angle $\theta_i = 40°$ measured in Fig. 6.6 where the reflected intensity was falling. This threshold depends on the geometry of the microlenses (NA), the microlens array arrangement and the intermediate layer thickness (optical adhesive layer). The intermediate layer thickness will also determine if the ray stays in the channel or not, i.e. if the incident light in a lens can emerge from another lens.

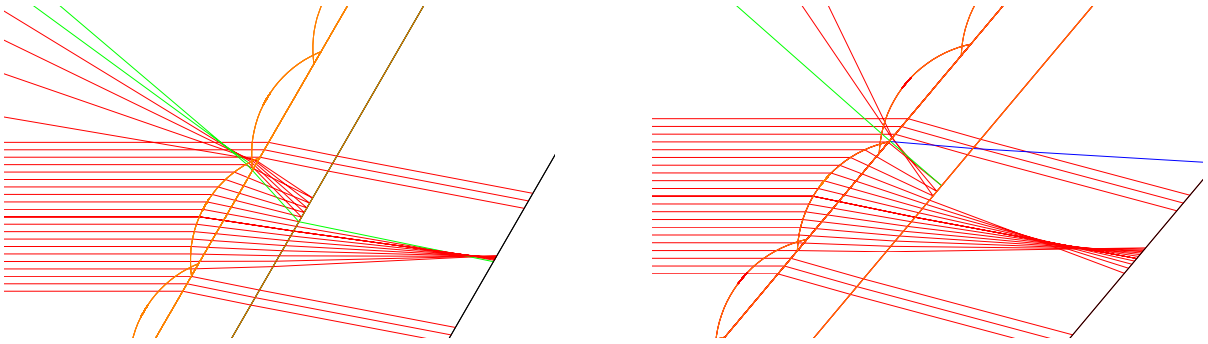

(a) (b)

Figure 6.10: Ray tracing simulation for incident light at 550 nm with a threshold fixed at 30 % of the peak flux, for incident angle: (a) angle $\theta_i = 30°$; (b) angle $\theta_i = 40°$. The diameter of the microlenses is 145 μm, the period is 150 μm and the height 25 μm. The multilayer Bragg reflector is made of 41 layers, has a reflection band centered at 550 nm with a maximum efficiency of 0.96 at normal incidence.

The measurement results for a sample with a multilayer Bragg reflector as described in Chap. 6.2 and replicated microlenses on top with 32 μm diameter and 16 μm height, that means hemispherical microlenses, are shown in Fig. 6.11(a). For an incident angle $\theta_i = 15°$,

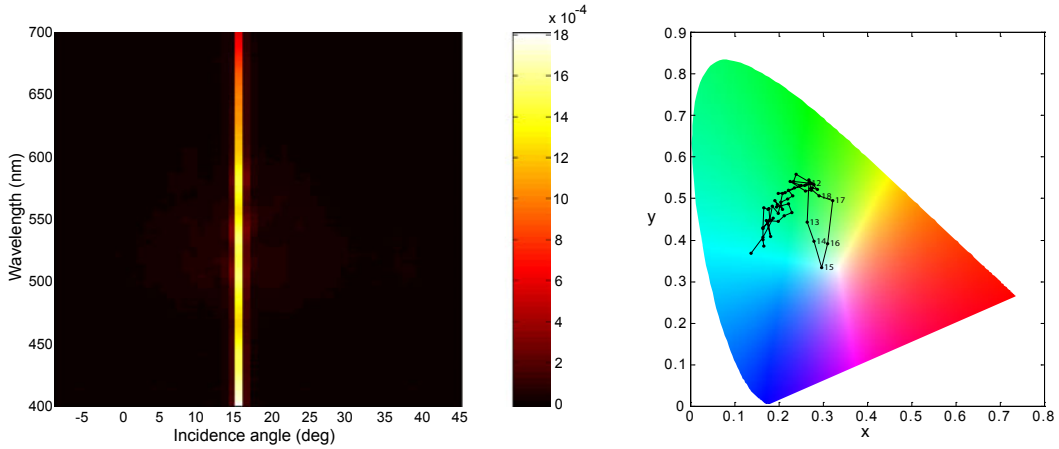

(a) (b)

Figure 6.11: (a) Reflection as a function of the angle of incidence using a fixed angle of 30° between the incident light and the direction of observation. Measurement for a multilayer Bragg reflector with microlenses 32 μm diameter and 16 μm height on top. The multilayer Bragg reflector has a reflection band centered at $\approx$ 570 nm with 5 PVA layers and 6 PVK layers. The thicknesses are $\approx$ 90 nm (PVA) and $\approx$ 80 nm (PVK). (b) Color coordinates in the CIE chromacity diagram for angle -10 to 40°.

one observes the maximum of intensity that is the specular reflected spectrum. At this angle, we can see that we have a quasi equivalent contribution in intensity for all the wavelengths between 400 and 600 nm. The corresponding color coordinate for $\theta_i = 15°$ in Fig. 6.11(b) is located in the middle of the diagram. Here the wavelength of reflection of the multilayer Bragg reflector has not a visible influence. Figures 6.12(a) and 6.12(b) show details for

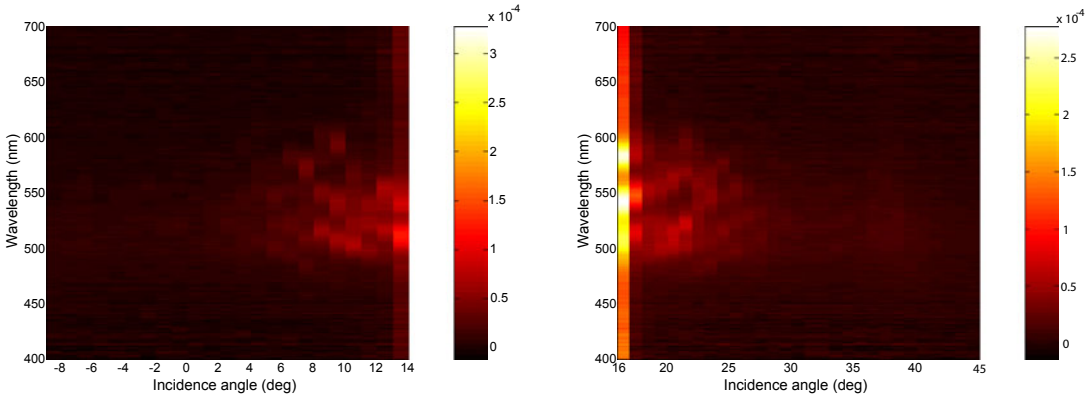

(a) (b)

Figure 6.12: Details of Fig. 6.11(a). (a) Angles between -9° to 14°; (b) angles between 16° to 45°.

angles between -9° to 14° and 16° to 45°. One sees that the reflection efficiency is very

low but there is a wavelength dependent reflection due to the multilayer Bragg reflector. Figure 6.13(a) shows that the intensity drops rapidly when the angle is different from the specular reflection angle. Details are shown in Fig. 6.13(b). Here, we do not find the plateau

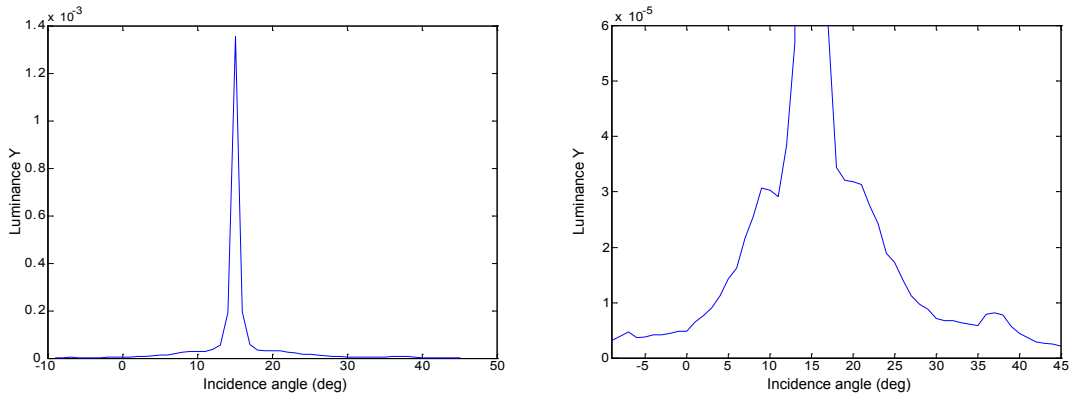

(a) (b)

Figure 6.13: (a) Luminance as a function of sample angle for the system given in Fig. 6.11(a). (b) Detail of the measurement.

of intensity that we had in Fig. 6.6 but there is again a small peak of intensity at $\theta_i = 37°$. For the case of hemispherical microlenses, an effect of total internal reflection inside the lens surface was seeked. Figures 6.14(a) and 6.14(b) show the simulation for incident light

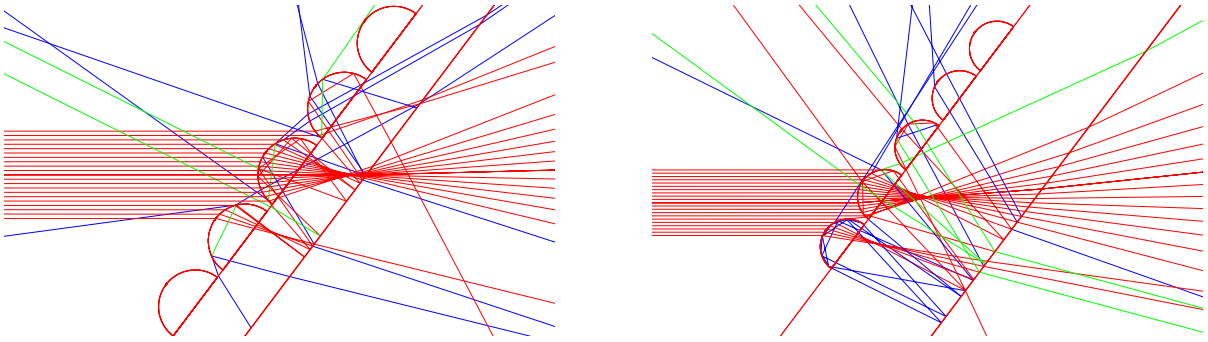

(a) (b)

Figure 6.14: Ray tracing simulation of hemispherical microlens array on a multilayer Bragg reflector for incident light at 540 nm with a threshold fixed at 10 % of the peak flux, thickness of the intermediate layer of: (a) 25 μm; (b) 70 μm. The diameter of the microlenses is 32 μm, the period is 35 μm and the height 16 μm. The multilayer Bragg reflector is made of 41 layers, has a reflection band centered at 550 nm with a maximum efficiency of 0.96 at normal incidence.

at 540 nm with a threshold fixed at 10 % of the peak flux, for incident angle $\theta_i = 37°$ and thickness of the intermediate layer of 25 μm and 70 μm, respectively. In the first case, the focal length of the microlenses is of the order of the distance between microlenses and multilayer Bragg reflector. In the second, the focal length of the microlenses is shorter than the distance between microlenses and multilayer Bragg reflector. With larger incident angles, it increases the possibility for the light to be reflected by the mirror in a neighboring

microlenses. One also sees that some of the rays are totaly internally reflected and have a long path before going out of the system. Such a system could produce interesting effects if photoluminescent polymer or dye are added in the UV curing material of the microlenses. The surface of the microlens (with internal total reflection) and multilayer Bragg reflector creating a wavelength selective microcavity where photoluminescence could be enhanced.

6.4 Concave microlenses on multilayer Bragg reflectors

As seen in SEM picture in [8], interesting visual effects are produced with spherical micro-cavities. Microlens arrays with negative curvature (concave microlenses) were replicated in an UV curing material over a multilayer Bragg reflector. To fabricate the mould of the concave microlenses, we began to fabricate standard microlenses in photoresist and a PDMS mould of them like described in Chap. 3.3 and 3.4, respectively. The mould of the concave microlenses was produced by using the mold of the standard microlenses as a master.
The measurement results for a sample with a multilayer Bragg reflector as described in Chap. 6.2 and replicated concave microlenses on top with 245 μm diameter and 20 μm deep are shown in Figs. 6.15(a) and 6.15(b). For an incident angle $\theta_i = 15°$, one observes the maximum of intensity that is the specular reflected spectrum. At this angle, the maximum of intensity is measured for a wavelength of 550 nm. That corresponds to the wavelength of reflection of the multilayer Bragg reflector at this angle. One can see in Fig. 6.17 that the intensity drops rapidly when the angle is different from the specular reflection angle. The interesting features are the loss of intensity between $\theta_i = 25°$ and 30°, and also around 7°. There are also peaks of intensity between $\theta_i = -5°$ and 6° and at $\theta_i = 32°$. In Fig. 6.15(b),

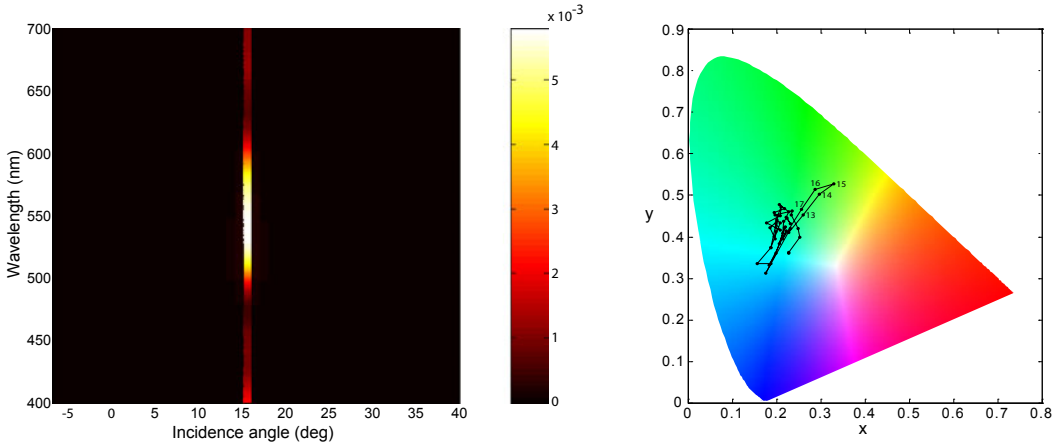

(a) (b)

Figure 6.15: (a) Reflection as a function of the angle of incidence using a fixed angle of 30° between the incident light and the direction of observation. Measurement for a multilayer Bragg reflector with concave microlenses 250 μm diameter and 20 μm height on top. The multilayer Bragg reflector has a reflection band centered at $\approx$ 570 nm with 5 PVA layers and 6 PVK layers. The thicknesses are $\approx$ 90 nm (PVA) and $\approx$ 80 nm (PVK). (b) Color coordinates in the CIE chromacity diagram for angle -10 to 40°.

one sees that for an incident angle $\theta_i = 15°$, the corresponding point in the CIE diagram is in the yellow-green region. For incident angles smaller or larger as $\theta_i = 15°$, on sees that the corresponding points in the CIE diagram go rapidly in the blue region. One sees this also in Figs. 6.16(a) and 6.16(b) where details of Fig. 6.15(a) are shown. The shift of the measured spectra in the blue region from 14° to 9° and 16° to 25° is much faster than in the case of a simple multilayer Bragg mirror.

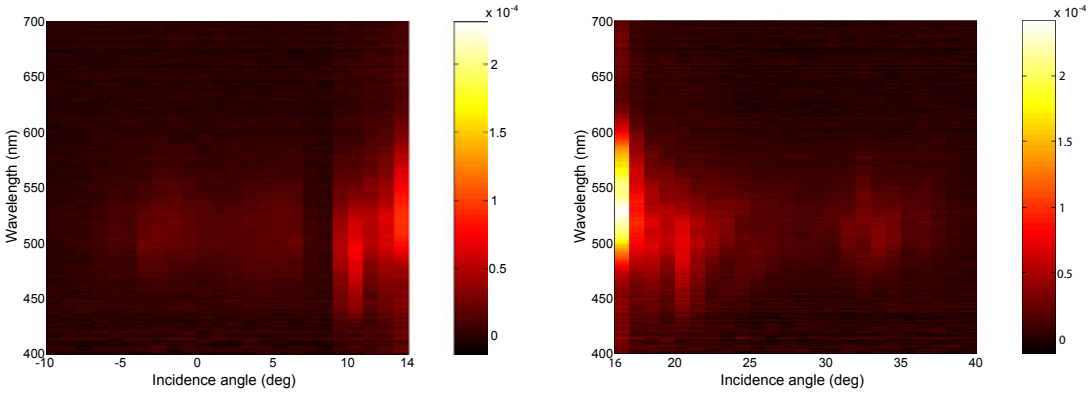

(a) (b)

Figure 6.16: Details of Fig. 6.15(a). (a) Angles between -10° to 14°; (b) angles between 16° to 40°.

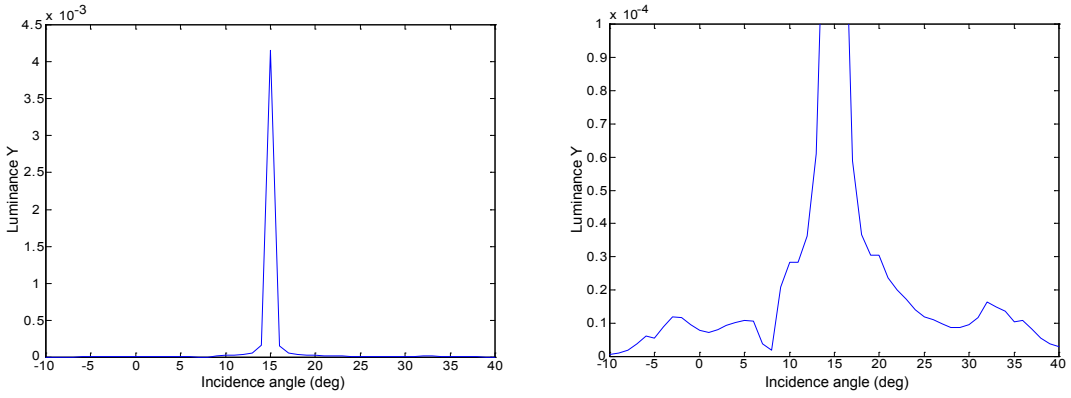

(a) (b)

Figure 6.17: (a) Luminance as a function of sample angle for the system given in Fig. 6.15(a). (b) Detail of the measurement.

A model based on this sample is simulated with ray tracing. To highlight the wavelength selectivity of the sample, a model of a multilayer Bragg reflector with a total of 41 layers was chosen. The reflector is placed on a glass substrate. The thickness of the layer between the microstructure and the glass substrate is 70 μm. The microlenses have a diameter of 245 μm, a period of 250 μm and 20 μm height. Figures 6.18(a) and 6.18(b) show ray trace simulations for an incidence angle $\theta_i = 0°$, with a threshold fixed at 4 % of the peak flux, for incidence wavelength of 540 nm and 530 nm, respectively. Red rays correspond to a range from 0.66 to 1 times the incident peak flux. Green corresponds to a range from 0.33 to 0.66 and blue to a range from 0 to 0.33 of the incident peak flux. An analysis done by changing the value of the threshold of the rays shows that at normal incidence the major contribution to the reflected intensity comes directly from the multilayer Bragg reflector, i.e. from the regions between the lenses that represent here only 13 % of the surface (fill-factor $\approx$ 0.87). The light goes through the optical adhesive layer without being refracted by a lens and is reflected by the multilayer Bragg mirror. The second most important contribution comes

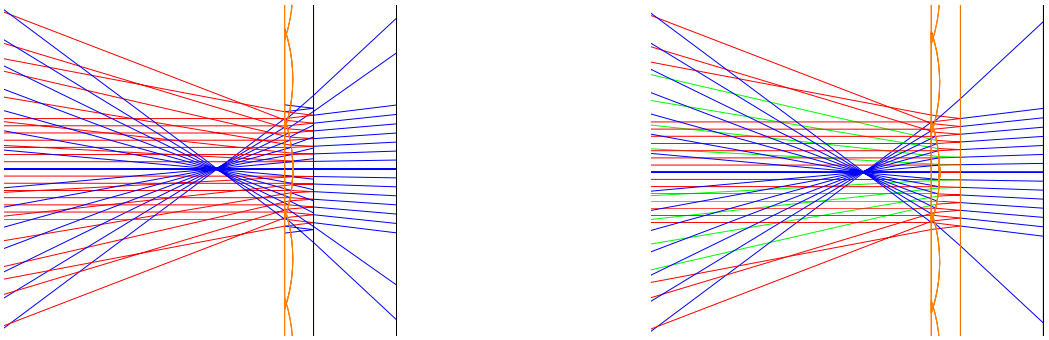

(a) (b)

Figure 6.18: Ray tracing simulation of concave microlens array on a multilayer Bragg reflector for incident light at $\theta = 0\,^\circ$ with a threshold fixed at 4 % of the peak flux, thickness of the intermediate layer of 70 μm and incident wavelength of: (a) 540 nm; (b) 530 nm. The diameter of the microlenses is 245 μm, the period is 250 μm and the height 20 μm. The multilayer Bragg reflector is made of 41 layers, has a reflection band centered at 550 nm with a maximum efficiency of 0.96 at normal incidence.

from the light refracted by the lens, reflected by the multilayer Bragg reflector and refracted a second time outside the lens surface. The reflected intensity coming back from the sample will be principally inside this cone. The angle of this cone is defined by the size of the lens, more precisely by the angle between lens and incident light. A smaller contribution comes directly from the part of the light being reflected at the interface air-lenses. Figures 6.18(a)

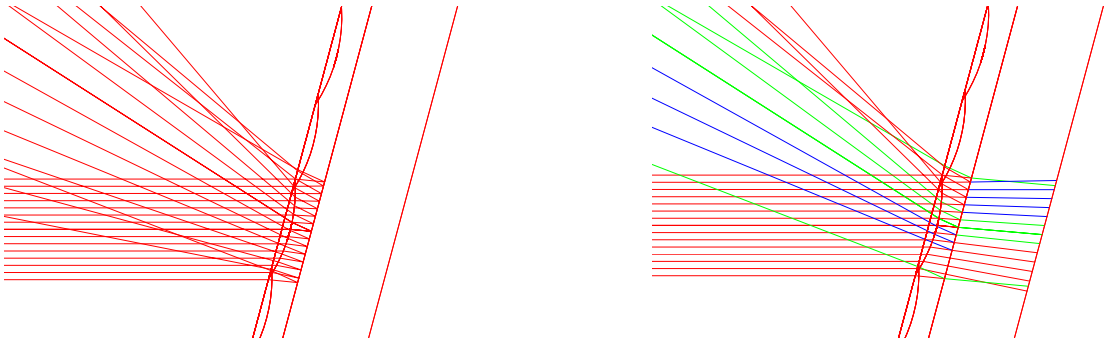

(a) (b)

Figure 6.19: Ray tracing simulation of concave microlens array on a multilayer Bragg reflector for incident light at $\theta = 15\,^\circ$ with a threshold fixed at 10 % of the peak flux, thickness of the intermediate layer of 70 μm and incident wavelength of: (a) 540 nm; (b) 520 nm. The diameter of the microlenses is 245 μm, the period is 250 μm and the height 20 μm. The multilayer Bragg reflector is made of 41 layers, has a reflection band centered at 550 nm with a maximum efficiency of 0.96 at normal incidence.

and 6.18(b) highlight the angular vs. spectral dependence of the multilayer Bragg reflector. The light with wavelength at 540 nm i.e. a bit lower than the wavelength of reflection of the multilayer Bragg reflector is reflected with high efficiency (red rays in Fig. 6.18(a)) when the incident angle on the reflector is large. For the light with wavelength at 530 nm, one sees

that the reflection efficiency for the rays in the middle of the lens is lowered. The rays at the side of the lens are more refracted and reach the multilayer Bragg reflector with a larger incident angle. They are reflected with high efficiency (red rays). The same effect is shown for the case of the specular reflection, i.e. $\theta_i = 15°$ and incidence wavelength of 540 nm and 520 nm, respectively, in Figs. 6.19(a) and 6.19(b). The light at 540 nm is reflected with a high efficiency (red rays in Fig. 6.19(a)). In Fig. 6.19(b) the incident wavelength is 520 nm. Only the rays with the larger angle of incidence, here the ones that are not much refracted by the lens, are reflected with a high efficiency. For the rays that reach the multilayer Bragg mirror with a smaller incident angle, the efficiency of reflection is reduced (reflected green and blue rays). Figures 6.20(a) and 6.20(b) show the simulation for incident light at

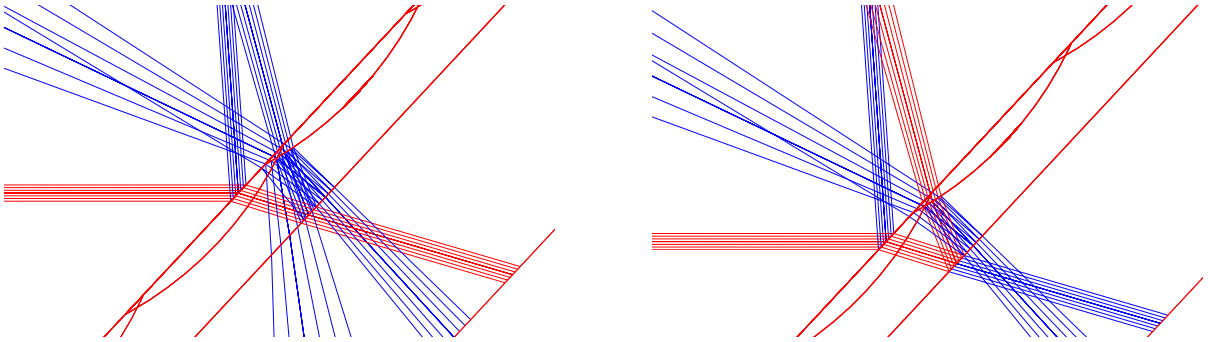

(a) (b)

Figure 6.20: Ray tracing simulation of concave microlens array on a multilayer Bragg reflector for incident light at $\theta = 35°$ with a threshold fixed at 0 % and 0.5 % of the peak flux, thickness of the intermediate layer of 70 μm and incident wavelength of: (a) 550 nm; (b) 510 nm. The diameter of the microlenses is 245 μm, the period is 250 μm and the height 20 μm. The multilayer Bragg reflector is made of 41 layers, has a reflection band centered at 550 nm with a maximum efficiency of 0.96 at normal incidence.

550 nm and 510 nm with a threshold fixed at 0 % and 0.5 % of the peak flux, respectively, for incident angle $\theta_i = 35°$. The part of the light which can be measured by the detector at 30° has the following path: The incident light is refracted in a region without lens, is reflected by the multilayer Bragg reflector and reflected again at the interface lens-air, reflected a second time by the multilayer Bragg reflector and finally refracted at the lens border. One understands easily that the part of the light reaching the detector is small. By comparing Figs. 6.20(a) and 6.20(b), ones sees that the efficiency of the first reflection on the multilayer Bragg mirror at wavelength 510 nm is larger than for the case of the wavelength 550 nm. The final intensity measured in the detector must have a stronger component at 510 nm. This effect is verified with the measurement in Fig. 6.16(b). This simple schema can also explain the threshold angle $\theta_i = 40°$ measured in Fig. 6.17(b) where the reflected intensity is decreases. This limit angle depends on the geometry of the microlenses (NA), the microlens array arrangement and the intermediate layer thickness (optical adhesive layer).

6.5 Micro prisms on multilayer Bragg reflectors

Microprism arrays (TRAF from 3M) were replicated in a UV curing material over a multilayer Bragg reflector. Figures 6.21(a) and 6.21(b) show a SEM image of a replicated microprim array. The prism array has a period of 50 μm with 25 μm height. The angle of the prism is 45°. The measurement results for a sample with a multilayer Bragg reflector as

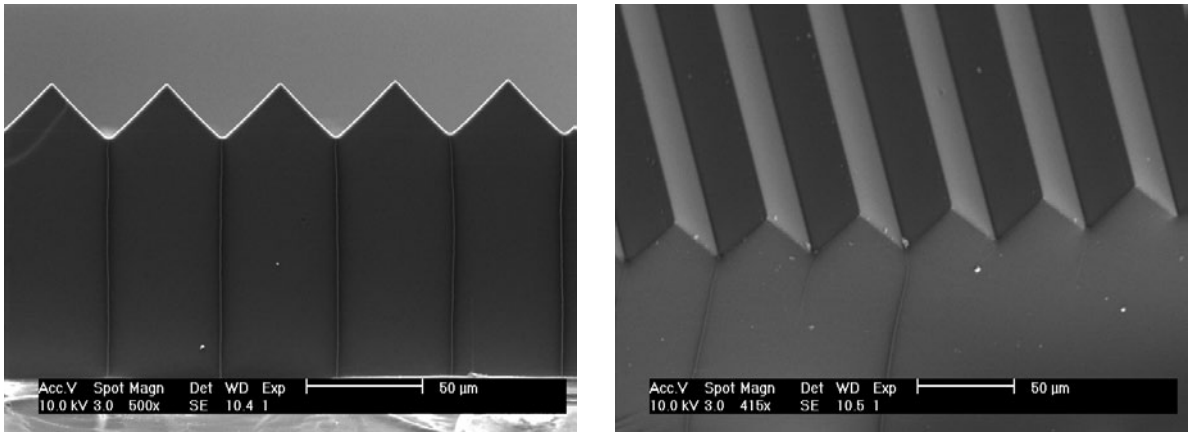

(a) (b)

Figure 6.21: SEM measurement of a replicated prism array with 50 μm period and 25 μm height: (a) side view; (b) top view.

described in Chap. 6.2 and a replicated commercial available prism array on top with 50 μm period and 25 μm height are shown in Fig. 6.22(a). For an incident angle $\theta_i = 15°$, one

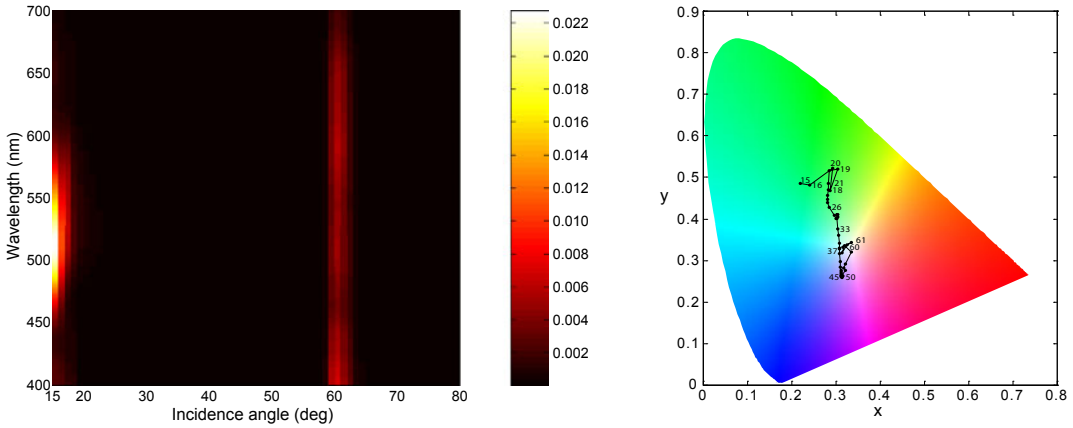

(a) (b)

Figure 6.22: (a) Reflection as a function of the angle of incidence using a fixed angle of 30° between the incident light and the direction of observation. Measurement for a multilayer Bragg reflector with replicated microprism array 50 μm period and 25 μm height on top. The multilayer Bragg reflector has a reflection band centered at $\approx$ 570 nm with 5 PVA layers and 6 PVK layers. The thicknesses are $\approx$ 90 nm (PVA) and $\approx$ 80 nm (PVK). (b) Color coordinates in the CIE chromacity diagram.

observes the maximum intensity that is the specular reflected spectrum. At this angle, the maximum of intensity is measured for wavelengths at around 520 nm. For a incident angle $\theta_i = 15°$, one has a bigger incident angle on the multilayer Bragg reflector, due to refraction at the prisms. The reflection is then shifted in the blue region compared to the sample without structured surfaces. One can see in Fig. 6.23 that the intensity drops rapidly when

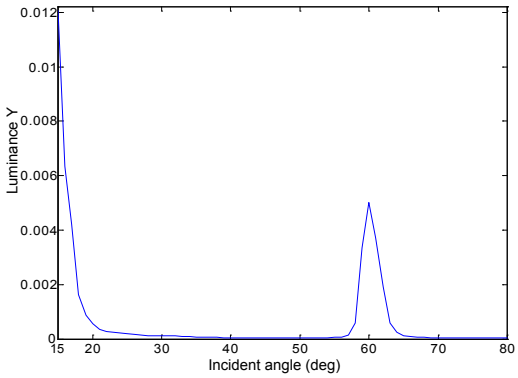

Figure 6.23: Luminance as a function of sample angle for the system given in Fig. 6.22.

the angle is different from the specular reflection angle. The interesting feature is the peak of intensity at $\theta_i = 60°$. Between $\theta_i = 20°$ and 58°, the measured intensity is very low. If we look at the sample at these angles, the sample is seen as grey. So, there is a range of angles where the sample does not reflect light. One can also see in Fig. 6.22(b) that the color of the reflected light outside the specular reflection is centered in the middle of the diagram. That means a grey sample. At $\theta_i = 60°$, we measured the specular reflection on one side of the prisms. The situation is illustrated in Fig. 6.25. For this reasons, the reflected spectrum is not dependent of the multilayer Bragg reflector and one can see in Fig. 6.22(a) that we have all the wavelengths reflected with the same intensity. The corresponding coordinate in the CIE diagram shown in Fig. 6.22(b) is in the center.
A model based on the sample geometry is simulated. To highlight the wavelength selectivity of the sample, a multilayer Bragg reflector with a total of 41 layers was chosen. The reflector is placed on a glass substrate. The thickness of the layer between the microstructure and the glass substrate is 70 μm. The micro prism array has a period of 50 μm and 25 μm height. Figures 6.24(a) and 6.24(b) show the ray trace simulation for an incidence angle $\theta_i = 15°$, for incidence wavelength of 490 nm and 550 nm, respectively. Red rays correspond to a range from 0.66 to 1 times the incident peak flux. Green corresponds to a range from 0.33 to 0.66 and blue to a range from 0 to 0.33 of the incident peak flux. One sees here the angular dependence of the multilayer Bragg reflector. Light refracted from the upper part of the prism has a smaller angle of incidence on the multilayer Bragg reflector. The light with wavelength at 550 nm is reflected with a higher efficiency (red rays in Fig. 6.24(b)). Light refracted from the lower part of the prism has a bigger angle of incidence on the multilayer Bragg reflector. The reflection efficiency of the light with wavelength at 490 nm is higher (red rays in Fig. 6.24(a)). The reflection band can be broadened or separated into distinct region, compared to the case of the multilayer Bragg reflector alone. Figure 6.25 shows the

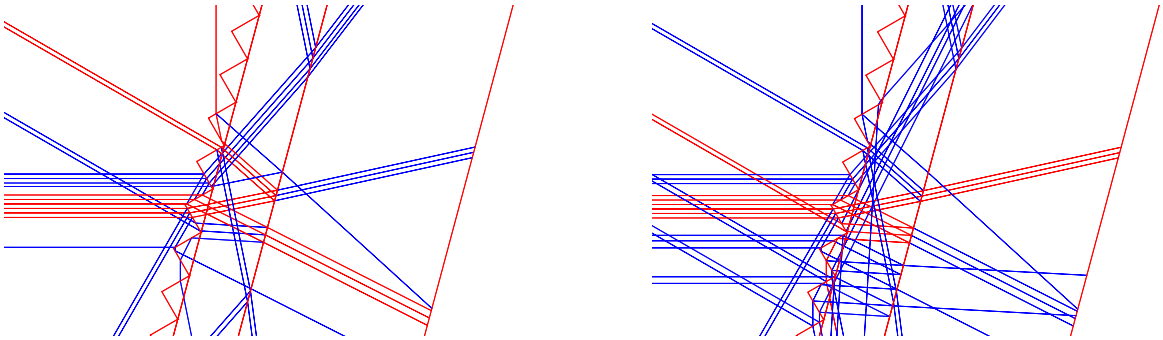

(a) (b)

Figure 6.24: Ray tracing simulation for incident angle $\theta_i = 15°$ for incident wavelength of: (a) 490 nm; (b) 550 nm. The thickness of the layer between the microstructure and the glass substrate is 70 μm. The period of the micro prism array is 50 μm and the height 25 μm. The multilayer Bragg reflector is made of 41 layers, has a reflection band centered at 550 nm with a maximum efficiency of 0.96 at normal incidence.

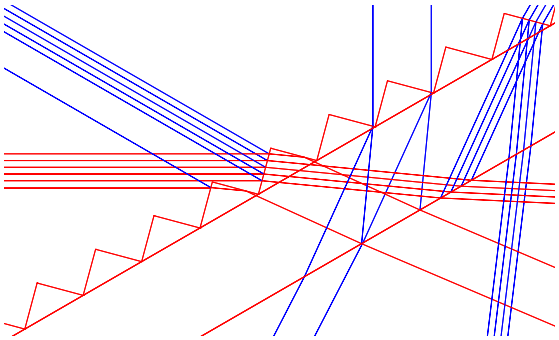

Figure 6.25: Ray tracing simulation for incident angle $\theta_i = 60°$ for incident wavelength of 550 nm. The thickness of the layer between the microstructure and the glass substrate is 70 μm. The period of the micro prism array is 50 μm and the height 25 μm. The multilayer Bragg reflector is made of 41 layers, has a reflection band centered at 550 nm with a maximum efficiency of 0.96 at normal incidence.

ray trace simulation for an incidence angle $\theta_i = 60°$, for incidence wavelength of 550 nm. One sees that the light is reflected by the lower side of the prim and do not interact with the multilayer Bragg reflector. For this reason, there is no wavelength dependence of the reflection for incident angle $\theta_i = 60°$.

6.6 Diffuser on multilayer Bragg reflectors

A commercially available diffuser (sandblasted glass from Edmund Optics) was replicated in a UV curing material over a multilayer Bragg reflector. Figure 6.26 shows the diffusing properties of the diffuser, i.e. the measurement of the diffused intensity as a function of the transmitted angle after the diffuser, when illuminated with a green laser at $\lambda = 532\,\text{nm}$. The measurement results for a sample with a multilayer Bragg reflector as described in

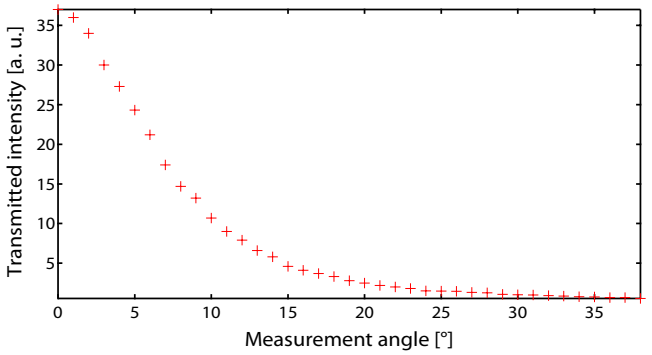

Figure 6.26: Measurement of the diffused intensity as a function of the transmitted angle after the diffuser. The light source used is a green laser at $\lambda = 532\,\text{nm}$.

Chap. 6.2 and a diffuser are shown in Fig. 6.27(a). One sees in Fig. 6.27(b) that the color

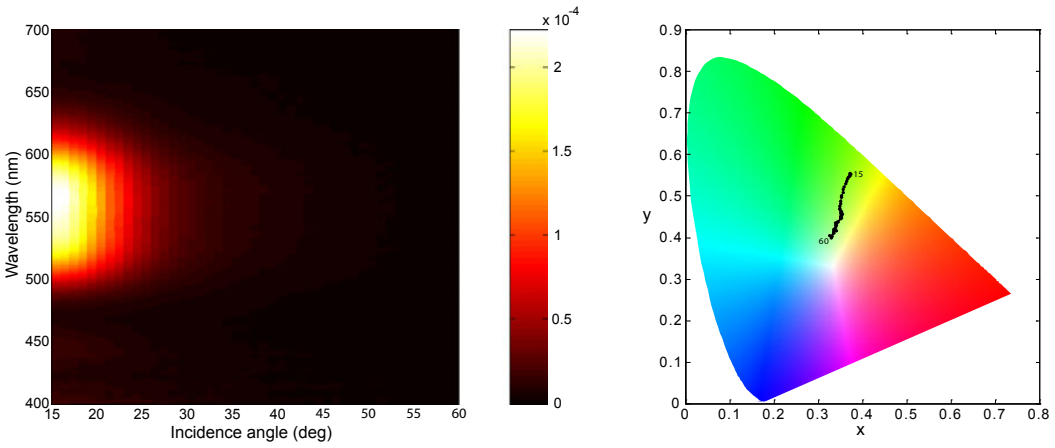

(a) (b)

Figure 6.27: (a) Reflection as a function of the angle of incidence using a fixed angle of 30° between the incident light and the direction of observation. Measurement for a multilayer Bragg reflector with replicated diffuser on top. The multilayer Bragg reflector has a reflection band centered at $\approx 570\,\text{nm}$ with 5 PVA layers and 6 PVK layers. The thicknesses are $\approx 90\,\text{nm}$ (PVA) and $\approx 80\,\text{nm}$ (PVK). (b) Color coordinates in the CIE chromacity diagram.

of the reflected light goes from the external region of the diagram for an angle of 15°, i.e. a pure color, to the middle of the diagram, that means a grey (or white) sample. For an incident angle $\theta_i = 15°$, one observes the maximum of intensity that is the specular reflected

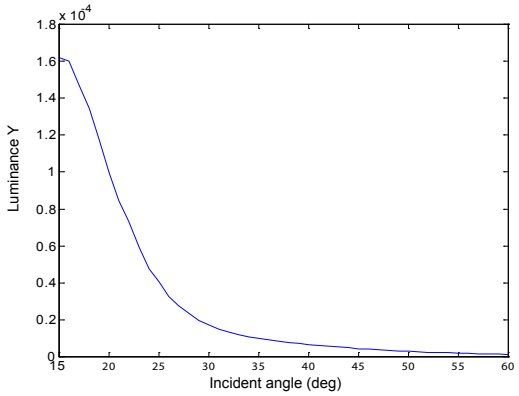

Figure 6.28: Luminance as a function of sample angle for the system given in Fig. 6.27.

spectrum. At this angle, the maximum intensity is measured for a wavelength at about 550 nm. That corresponds to the wavelength of reflection of the multilayer Bragg reflector for normal incident angle. One can see in Fig. 6.28 that the intensity decreases to 10 % of the initial value when the incident angle goes from 15° to 30°. This sample combines spectral selectivity in wavelength of the multilayer Bragg reflector with the angular selectivity of the diffuser. It is important to remark that the light is diffused twice by the diffuser. Once before reaching the reflector, and another time when reflected by the reflector.

Chapter 7

Organic light emitting diode on structured substrate

Organic materials for electronics and organic light emitting diodes (OLED) with low threshold voltage appear at the beginning of the 80', opening a wide research field in optoelectronics [12, 41, 45]. These organic materials with semiconducting and electroluminescent properties excite large perspectives. These new electroluminescent polymers can conduct electricity, exhibit optical absorption (usually in the UV/blue region) and emit throughout the visible when optically pumped or electrically supplied. Many groups published work on photo-pumped polymer lasers, none on successful electrically pumped systems. In 1963 the earliest report of electroluminescence from organic material, operating at over 400V, was published [33]. In 1987, the first electroluminescent material working at 10V in a multilayer organic device was reported [41]. In 1990 , the first electrical operation of a LED based on conjugated polymer PPV was reported [12]. This was the start of a vast research interest in the OLED technology for flat panel displays market.
The organic or polymer light emitting diode rise interests for several reasons. The principal reasons are because of the polymer being:

- Potentially cheap and easy to make
- Chemically tailored for specific applications
- Easy to handle
- Easily processable in thin layers by spin-coating on various substrate
- Moldable
- Printable (ink jet-printed polymer display matrices already achieved)

In Fig. 7.1, on can see a schematic illustration of an organic light emitting diode (OLED). The basic structure of the OLED (or PLED for polymer light emitting diode) is a stack of different layers on a transparent substrate. The first layer is a transparent conducting electrode, in our case Indium-Tin-Oxide (ITO) [20]. On this ITO layer, a hole injection layer can be added, in order to reduce the energy barrier between the ITO and the conducting

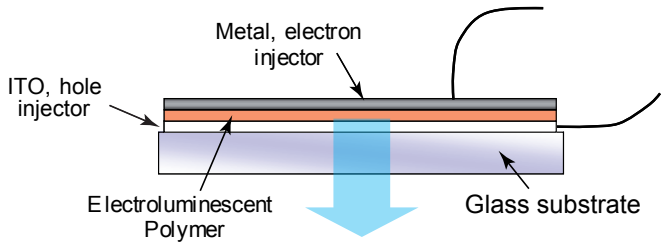

Figure 7.1: Illustration of an organic light emitting diode.

polymer. We use a well known hole injection layer called PEDOT. PEDOT is a water soluble polymer that can be deposited directly over the ITO layer by spin-coating. On the PEDOT layer, the electroluminescent polymer is then deposited, also by spin-coating. Finally, a metallic electrode is evaporated on the top. Generally, a combination of various metals is used to reduce the energy step for the electron coming from the metal to the polymer. The basic principle of electroluminescence is illustrated on Fig. 7.2(a). The general properties

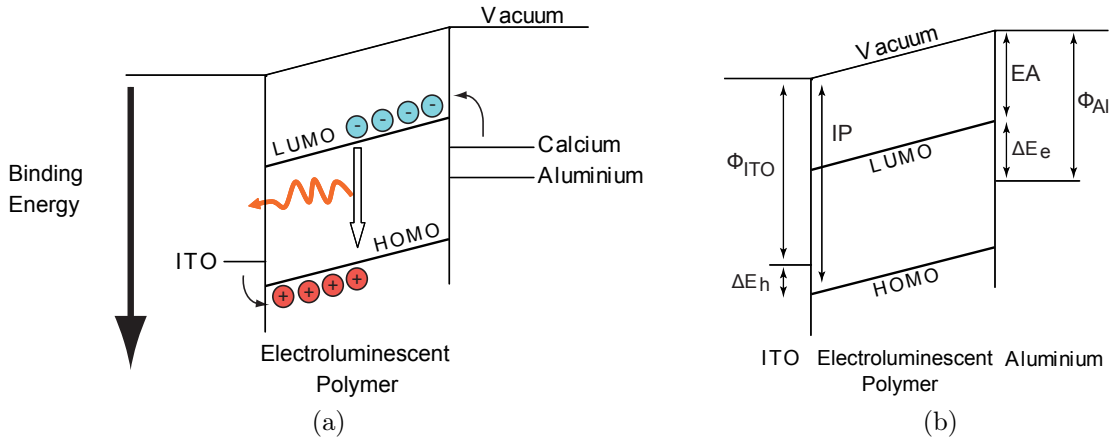

Figure 7.2: (a) Basic principle of electroluminescence in an organic light emitting diode. (b) Schematic energy level diagram for an ITO/Active Polymer/Al LED, showing the ionization potential (IP) and electron affinity (EA) of the active polymer, the work functions of ITO and Al (ϕ_{ITO} and ϕ_{Al}), and the barriers to injection of electrons and holes (ΔE_e and ΔE_h). There is a barrier for hole injection from the ITO electrode into the valence band states (or highest occupied molecular orbital, HOMO), and, with aluminium as cathode, a considerably larger barrier for electron injection into the active polymer conduction band states (or lowest unoccupied molecular orbital, LUMO). The illustrations are from Ref. [15].

of electroluminescence in conjugated polymer are exposed in [15]. The semiconducting properties of conjugated polymers come from their delocalized π-electron bonding along the polymer chain. The π and π^* orbitals, respectively bonding and antibonding orbitals, form the delocalized valence and conduction wavefunctions, which allow mobile charge carriers. Electroluminescence is induced by the recombination and the radiative decay of oppositely charged carriers called exciton (excited electron-hole state). In OLED structures, injection of electrons is made from one electrode and holes from the other. OLED is emitting light when the diode is biassed sufficiently to achieve injection and recombination of positive

and negative charge carrier within the polymer layer. The injection can be simplified if the electrodes are chosen to facilitate the transfer of charge carrier into the polymer. The hole-injecting electrode must have a relatively high work-function, like for instance, ITO. The electrons-injecting layer must have a low work-function. It is the case for metals such as Al (4.3 eV), Mg (3.7 eV) or Ca (2.9 eV). Figure 7.2(b) shows a schematic energy level diagram for a simple 3 layers OLED structure with ITO/Active Polymer/Al. The different energy levels for the charge carriers in metal electrodes layers and active polymer layers are illustrated. One sees the electron affinity (EA) and ionization potential (IP) of the active polymer, the work functions of ITO and Al (ϕ_{ITO} and ϕ_{Al}, respectively). The energy barriers ΔE_e and ΔE_h for electrons and holes injection, respectively, are also illustrated. The barrier for hole injection from the ITO electrode into the valence band states, also called highest occupied molecular orbital (HOMO), is generally small. The barrier for electron injection from aluminium cathode into the active polymer conduction band states, also called lowest unoccupied molecular orbital (LUMO), is larger.

The literature tells us that OLEDs with Al and ITO electrodes are not electrically efficient. Despite the fact that the energy barrier for holes between ITO and the active polymer is quite small, the influence of this difference in energy is to limit the transfer of the holes from the ITO electrode to the polymer. To reduce this barrier, one generally adds a layer called hole transport layer. This layer divides the initial barrier in two lower barriers. The energy needed for a hole to cross the interface is then reduced. For the hole transport layer, the water soluble PEDOT was chosen. Like for the ITO layer, PEDOT is well known as hole transport layer in OLED technology. For the metal electrode, on can use different metals with smaller work function to reduce the barriers to injection of electrons. For the cathode, it has been shown in [11, 19] that the insertion of a thin (some nm) insulating layer of LiF between the active polymer layer and the cathode results in a decreased operating voltage and an enhanced emission. This effect is principally attributed to a decrease in the effective work-function of the cathode with the presence of LiF. One explains this by the large voltage drop which is created through this thin insulating layer. This shifts the Fermi level of Al close to the lowest unoccupied molecular orbital (LUMO) of the active polymer. The electron injection is then increased because of this smaller difference between the work-function of the cathode and the LUMO of the active polymer.

The technology for fabricating OLED being well known and giving good emitting efficiency for number of visible colors, an idea is to fabricate a custom OLED on a corrugated grating to change the angular emission properties. The goal in depositing an OLED on a corrugated grating is to create a distributed feedback regime in the active polymer waveguide layer. By doing this, the light produced inside the active layer is guided in the layer and sees a modulation of the refractive index, creating a reflection in the layer. If the system is well dimensioned, the incident guided light and reflected light form a standing wave inside the active layer. The goal is here to model the all electrically supplied system, including active layer, transport and contact layer, to have a standing optical mode inside the active layer. This geometry is known as a distributed feedback (DFB) as the reflection is not depending on a specific place but distributed along the all grating. Lasing effects have already been observed in optically pumped system but never when the system is electrically supplied. This

comes from the losses in the electrically supplied configuration. For instance, the origin of optical losses come from different sources in the contact and transport layers that are:

- Metal contact absorption
- Rough interfaces
- Material impurities
- Absorption in the different layers
- Fabrication deviation from model

Another limitation comes from the fact that triplet states that are the 75% of electrical "excitations" are non-emissive due to spin conservation rule. Another problem can be the low quality of the cavity. Electrical losses are due to different sources including:

- the potential barriers between the different layers (for this reason, we add some transport layers to reduce the energy of the barriers)
- poor mobility of the electrons or holes
- different mobility between electrons and holes giving badly recombination zone
- chemical reaction between layers
- charge trapping by impurities
- complicated charge transport mechanisms
- material degradation giving rise to heating
- short circuits

The distributed feedback approach use diffraction from the grating to create a system of counter-propagating, coupled waveguide modes. It has been chosen because it lends itself well to thin film systems found in organic LEDs. An advantage of this approach is that the feedback is distributed throughout the waveguide, avoiding cavity design with "hard borders" like mirrors. This design is relatively simple and close to existing OLED to guaranty an easy fabrication process for people already knowing fabrication technique for OLED and grating structures.

7.1 Modeling

In this section, we are interested in modeling optically an OLED on a corrugated substrate to work in a distributed feedback regime (DFB). A simple illustration of the optical principle of a distributed feedback laser is shown in Fig. 7.3. A corrugated waveguide with grating period

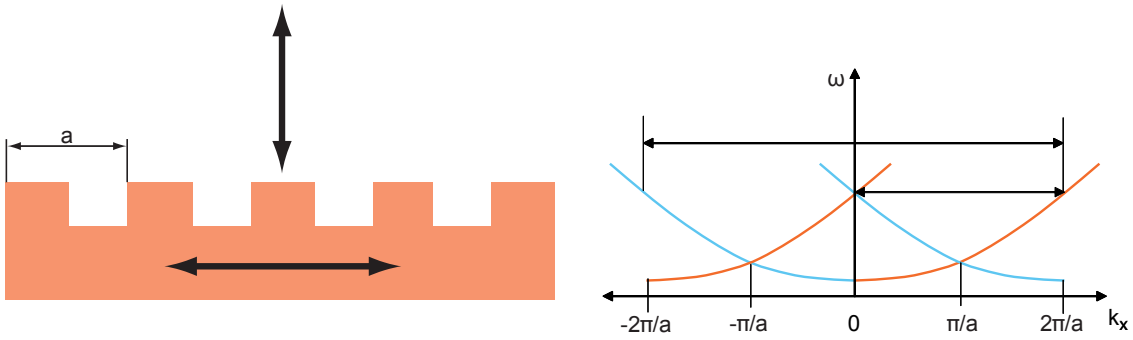

Figure 7.3: Basic principle of a distributed feedback operation.

a is illustrated. One can see in the dispersion diagram that guided light inside the corrugated waveguide with the specific value of x-component of the wave vector being $k_x = 2\pi/a$, can be diffracted by the grating (first order) to reach $k_x = 0$. The wave vector K of the grating is simply added (or subtracted) to k_x as the grating equation requires. That means the light is coupled out of the system, or can be diffracted in the second grating order to reach $k_x = -2\pi/a$. This geometry with the second order being reflected inside the waveguide is sometimes called second order grating. The first order grating case, meaning that the light diffracted in the first order is reflected inside the waveguide, is achieved if the grating period is about twice shorter. This last case was not considered since the grating fabrication with such a small period (between 120 nm and 180 nm) was not possible at IMT. The grating creates

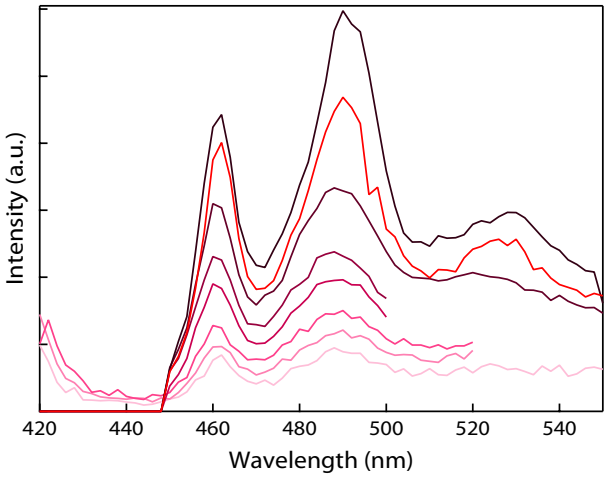

Figure 7.4: Measured spectra of a non-structured layer of Me-LPPP on a glass substrate pumped with a 405 nm wavelength laser, at various pump laser powers.

in the waveguide a guided wave in the opposite direction. The two counter propagating

waves combine to form a standing wave. The choice of the active material must be done carefully. The choice was first made for a polymer called Me-LPPP, that is a ladder-type polymer [39]. The ladder type structure leads to a better-defined molecular orientation and lower defects. This polymer is known for its good stability against oxygen and UV, has a good optical absorption at 450 nm ($\alpha > 10^5\,\mathrm{cm}^{-1}$) that falls rapidly at higher wavelengths. The emission spectrum (see Fig.7.4) extends from 460 nm up to 600 nm, peaking at 465 nm and 491 nm. The peak at 465 nm being sharper, would be preferred for a lasing experience. This polymer is also soluble in a range of common solvents.

Figure 7.5: Geometry for the simulation for coupling inside a flat waveguide by evanescent field.

The first step in modeling the structured OLED is to couple light in a flat polymer waveguide such as illustrated in Fig. 7.5. The goal is to find the thickness to have only one mode guided

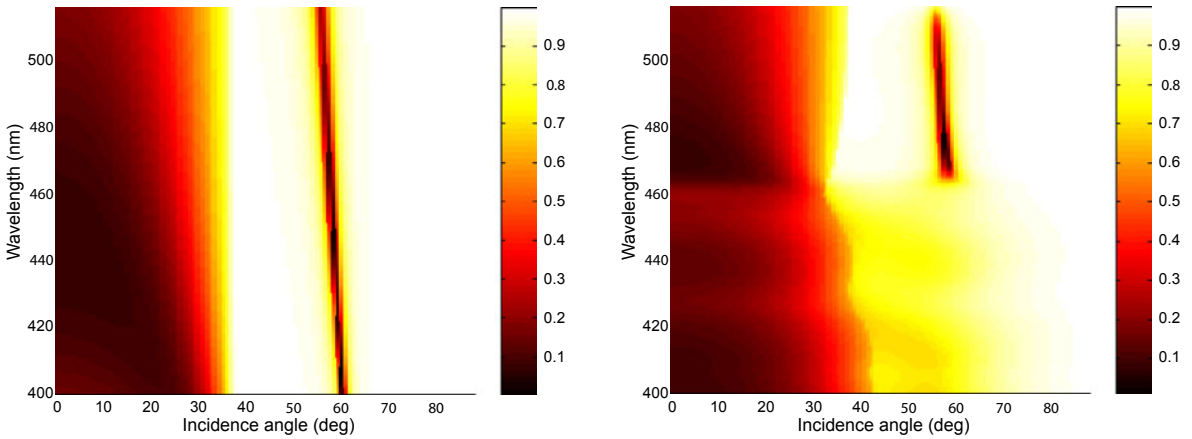

(a) (b)

Figure 7.6: (a) Simulation of the reflection efficiency as a function of the incident angle for a flat waveguide with thickness $d = 135\,\mathrm{nm}$, with fixed refractive index $n = 1.6745$ and absorption $k = 0.0073$. (b) The same simulation with the values $n = n(\lambda)$ and $k = k(\lambda)$.

in the waveguide for the wavelengths of interest. To do so, the waveguide is separated from the incident medium by a small air gap for light coupling. The refractive index of the incident medium is the same as the waveguide. This allows to couple light inside the waveguide by means of the evanescent waves. In our case the separation was around $80 - 100\,\mathrm{nm}$. This separation has no influence on the position of the guided modes in the waveguide that appear after the critical angle of incidence. It only changes the intensity of the light that couples through the air gap. This separation has a lot of influence before the critical angle is reached because it changes the reflection properties of the system. The refractive index

and absorption of the polymer were first taken at $n = 1.6745$ and $k = 0.0073$. These values correspond to the refractive index and absorption when the wavelength is $\lambda = 491\,\text{nm}$, i.e. the wavelength of the photoemission peak of the polymer [39]. The simulations were done for the angle of incidence between 0° to 90°. Figure 7.6(a) shows the dependence of the reflected spectrum with the incidence angle. One observes two distinct regions. The first region with an incidence angle between $\theta = 0°$ and the critical angle and the second region from the critical angle to $\theta = 90°$. It is in the second region that we see a coupling of light into the waveguide. The evanescent wave is created by total reflection at the interface between the incident medium and the air gap. For an incident angle close to $\theta = 60°$, the loss of reflection is due to the coupling of light into the waveguide mode. To have only one mode in the region of interest, represented here by the vertical dark line, the thickness of the waveguide was fixed at $d = 135\,\text{nm}$ in the simulation. This is close to the value $d = \lambda/4n$ with n the refractive index of the polymer. To have a more precise simulation, the wavelength dependence of the refractive index n and absorption k of the active polymer waveguide have to be taken into account. The data for the polymer Me-LPPP were taken from [39]. The refractive index n and absorption k of the active polymer is illustrated in Figs. 7.7(a) and 7.7(b). It is important to note that, at this scale, the refractive index

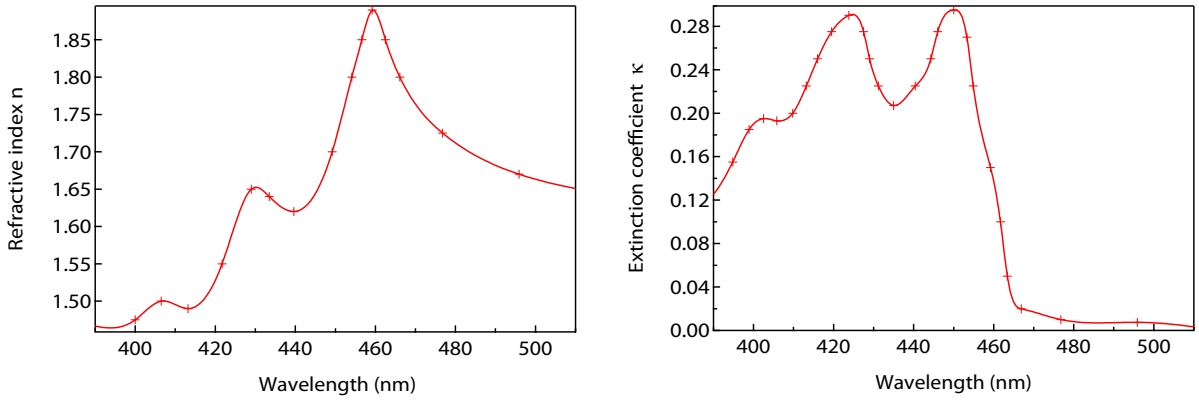

(a) (b)

Figure 7.7: (a) Refractive index dependence in function of the wavelength for the Me-LPPP active polymer, $n = n(\lambda)$. (b) Extinction coefficient dependence in function of the wavelength (absorption), $\kappa(\lambda)$. Data from [39].

and absorption are also dependent on the thickness of the polymer layer. Figure 7.6(b) shows the results of simulation for the case with the correct wavelength dependence of the refractive index n and absorption k. In this case, one observes that a part of the guided mode disappeared. The wavelengths below 460 nm are absorbed by the polymer, resulting in the vanishing of the waveguide modes for these wavelengths. As a result, the peak at $\lambda = 465\,\text{nm}$ will not be considered as an optimal lasing wavelength in a DFB structure.
The next step is to add a grating on the waveguide to create counter-propagating waves inside the system. The corrugated polymer waveguide is illustrated on Fig. 7.8. The parameters that can be varied are the grating period, the grating height and the grating shape. For the first model, a simple square grating was chosen. The grating period must be adapted to

Figure 7.8: Simulation for coupling inside a corrugated waveguide by evanescent field.

have the counter-propagating wave and a resulting stationary wave at the chosen wavelength. The grating height has an influence on the efficiency of the diffracted orders. In addition the effective thickness of the waveguide is modified depending of the grating height. With a good adaptation of the grating period and grating height, counter propagating modes at the right wavelength, that means at the wavelength of emission of the active polymer, are created. The distributed feedback modes are seen in the simulation by the crossing of the modes at incident angle $\theta = 0°$ that correspond to the x-component of the wavevector $k_x = 0$. Figure 7.3 shows this mode crossing at $k_x = 0$. It is well known that the two optical modes are coupled [49]. As a result, the dispersion curve at the crossing point changes and creates a band gap between the two modes. At this point, the group velocity reaches zero $v_g = d\omega/dk = 0$ that means, there is a stationary wave with two distinct stationary modes inside the waveguide. The two modes have a small difference in energy, corresponding to the band gap energy.
The simulation result of a corrugated waveguide with thickness $d = 135\,\text{nm}$, grating period $\Lambda = 373\,\text{nm}$, grating depth $h = 50\,\text{nm}$ with $n = n(\lambda)$ and $k = k(\lambda)$ is shown in Fig. 7.9. For an angle close to $\theta = 0°$ that corresponds to the x-component of the wavevector close to

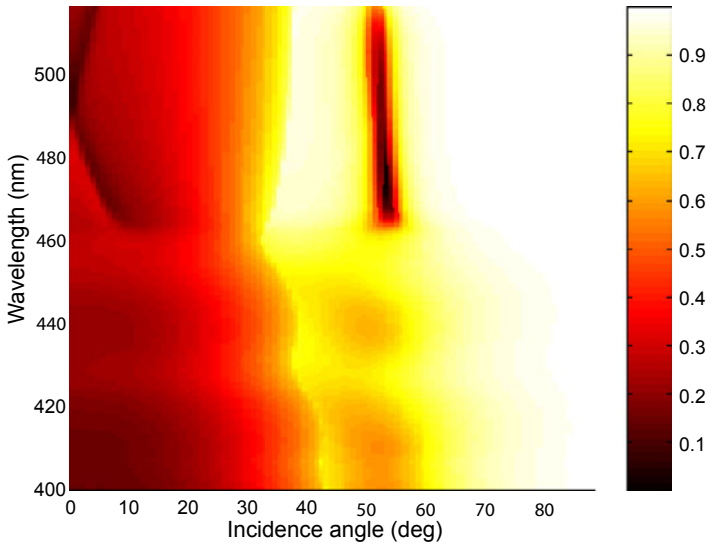

Figure 7.9: Simulation of the reflection efficiency as a function of the incident angle for a corrugated waveguide with thickness $d = 135\,\text{nm}$, grating period $\Lambda = 373\,\text{nm}$, grating depth $h = 50\,\text{nm}$ and with $n = n(\lambda)$ and $k = k(\lambda)$.

$k_x = 0$, two "reflected" modes appear.

A model of a simple polymer waveguide in air is now dimensioned for the particular case of the polymer Me-LPPP. The next step is to model a more realistic structure, by adding a substrate. This was done for a structure as illustrated in Fig. 7.10. The grating is directly

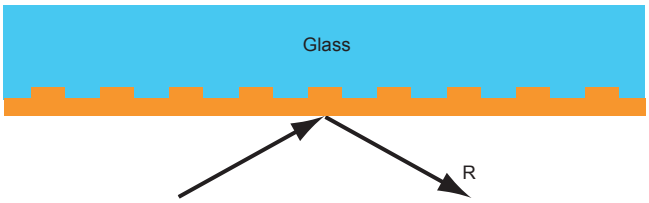

Figure 7.10: Waveguide on a corrugated substrate.

etched in a glass substrate. The refractive index contrast at the waveguide border is modified compared to the case without substrate. This modification induces some changes. It is clear that the refractive index of the glass substrate ($n_{Glass} \approx 1.5$) is closer to the polymer refractive index than air. The result is that the modes in the waveguide are less confined and the waveguide thickness has to be increased to keep a mode in the waveguide. The efficiency of the grating is also reduced due to a lower refractive index between glass and substrate. To conserve the reflectivity, the hight of the grating has to be increased. Figures 7.11(a)

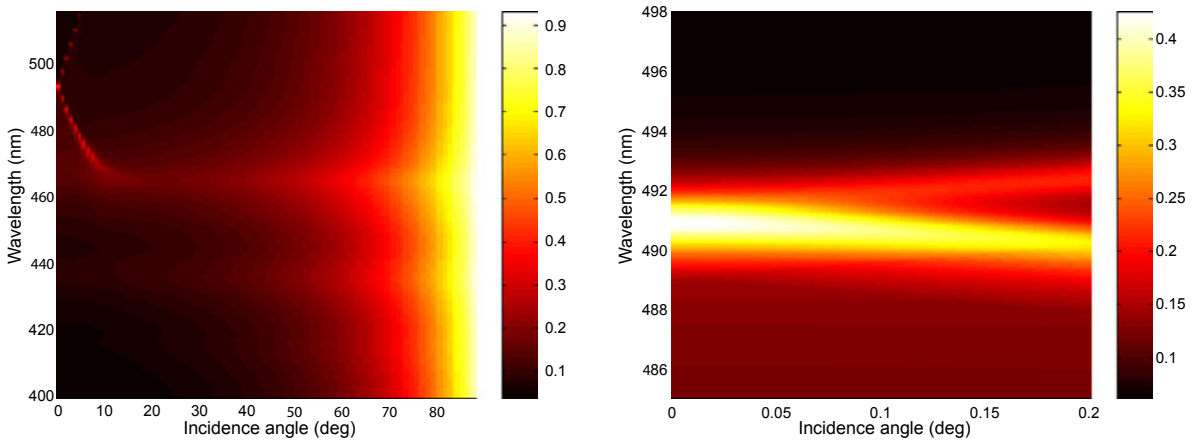

(a) (b)

Figure 7.11: (a) Simulation of a polymer waveguide with thickness $d = 190\,\text{nm}$, grating depth $h = 120\,\text{nm}$, grating period $\Lambda = 326\,\text{nm}$ and a fillfactor of 50%. (b) Detail of the same simulation close to $\theta = 0$.

and 7.11(b) show simulations for a polymer waveguide with thickness $d = 190\,\text{nm}$, grating depth $h = 120\,\text{nm}$, grating period $\Lambda = 326\,\text{nm}$ in the configuration illustrated in Fig. 7.10. For small angles and wavelengths around $\lambda = 491\,\text{nm}$, one sees the signature of the optical mode as a bright line corresponding to an enhanced reflectivity. This enhanced reflectivity is due to the fact that a part of the light is coupled into the waveguide. The guided light is then decoupled from the waveguide by the grating and increases the total reflectivity.

In order to reduce the hight of the grating, one could imagine to have the grating on the other side where the refractive index contrast is the bigger. Figure 7.12 illustrates this configuration with the grating directly stamped in the active polymer layer. The simulation

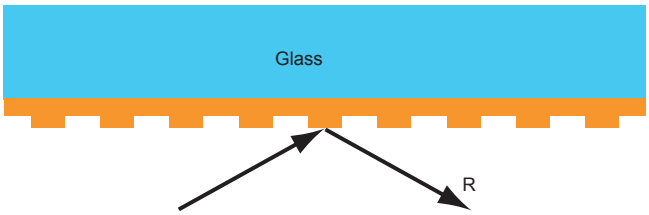

Figure 7.12: Corrugated waveguide on a flat substrate.

for a corrugated waveguide in such a configuration is shown in Figs. 7.13(a) and 7.13(b). The results are similar to the ones shown in Figures 7.11(a) and 7.11(b). For small angles and wavelengths around $\lambda = 491\,\text{nm}$, one sees the signature of the optical mode as a bright line corresponding to an enhanced reflectivity. This enhanced reflectivity is due to the fact that a part of the light is coupled into the waveguide. The guided light is then decoupled from the waveguide by the grating and increases the total reflectivity. To have a similar effect than

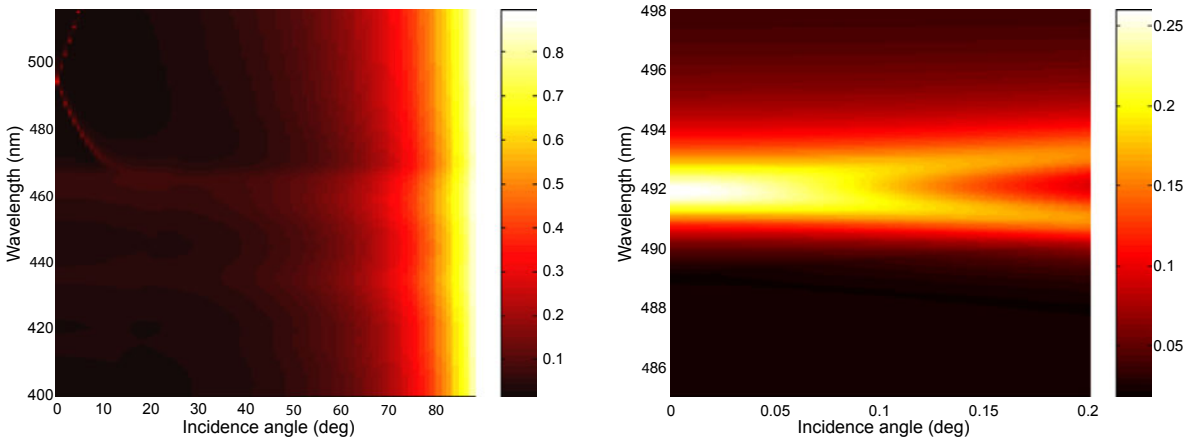

(a) (b)

Figure 7.13: (a) Dispersion diagram (reflection efficiency as a function of the incident angle) of a polymer waveguide with thickness $d = 165\,\text{nm}$, grating depth $h = 50\,\text{nm}$, grating period $\Lambda = 326\,\text{nm}$ and a fill-factor of 50%. (b) Detail of the dispersion diagram close to $\theta = 0$.

obtained in the case of a grating etched in glass (see Figs. 7.10 and 7.11), the parameters have to be modified to obtain a waveguide with thickness $d = 165\,\text{nm}$, grating depth $h = 50\,\text{nm}$ and grating period $\Lambda = 326\,\text{nm}$. The grating height and waveguide thickness are reduced from $h = 120\,\text{nm}$ to $h = 50\,\text{nm}$ and from $d = 190\,\text{nm}$ to $d = 165\,\text{nm}$, respectively. That means, the optical modes are more confined in the second case.
In order to know what were the tolerances on the fabricated samples and which dimensions were the most critical, a rigorous numerical study of the influence of the parameters like

grating period, grating height, polymer waveguide thickness and fill-factor has been done. To do this, we started from the above given parameters and changed one by one the parameters. We controlled the effects on:

- The wavelength of the guided mode in the dispersion diagram for incident angle $\theta = 0$.
- The intensity of the TE component of the reflected field, i.e. the effect on the coupling.
- The width (FWHM) of the mode at $\theta = 0$.
- The intensity of the total field.
- The variation of the position of the maximum of the field inside the structure.

It was found that the period of the grating has a particular importance. For a simple active polymer waveguide 115 nm thick with a grating period 326 nm and 50 nm height on top, deposited on a glass substrate, the position of the optical mode at $\theta = 0$ varies by 1.7 nm when the grating period varies by 1 nm. The effects of the grating height and polymer thickness on the position of the optical mode at $\theta = 0$ are more than 10 times lower. The wavelength of the guided mode for the angle $\theta = 0$ must correspond to the peak of luminescence of the polymer. As it is shown in Fig. 7.4, a small displacement induces a severe decrease of luminescence. In order to limit the shift in wavelength to $\Delta\lambda = 5$ nm, the grating period must be fabricated with a precision of $\Delta\Lambda = 3$ nm, corresponding to a variation tolerance of $\Delta\Lambda/\Lambda \approx 1\%$.
It is also important to qualify the influence of the grating geometry variation on the confined mode. In our case, due to the fabrication of the grating by laser interference in photoresist (see Chap. 3.2), the fill-factor could slightly vary. As illustrated in Fig. 7.14, we define the

Figure 7.14: Definition of the fill-factor for the grating structure.

fill-factor as the ratio between the width of one single grating dent over the grating period. Figures 7.15(a) and 7.15(b) show details of the simulations of the reflection efficiency as a function of the incident angle for a corrugated waveguide in air, for two different values of the fill-factor. The thickness is $d = 130$ nm, the grating period $\Lambda = 373$ nm and the grating depth $h = 40$ nm. One can see the influence of the fill-factor on the optical mode. The fill-factor asymmetry clearly advantages and strengthens one of the two band structures. This can be explained by looking at the position of the maximum optical field of the stationary wave inside the structure. For example, for a fill-factor smaller than 50%, the regions where the waveguide is thinner are larger (see Fig. 7.15(b)). The optical mode that has his maximum optical fields of the stationary wave in these regions will be strengthened. At the same time, the regions where the waveguide is thicker are narrower. The optical mode that has

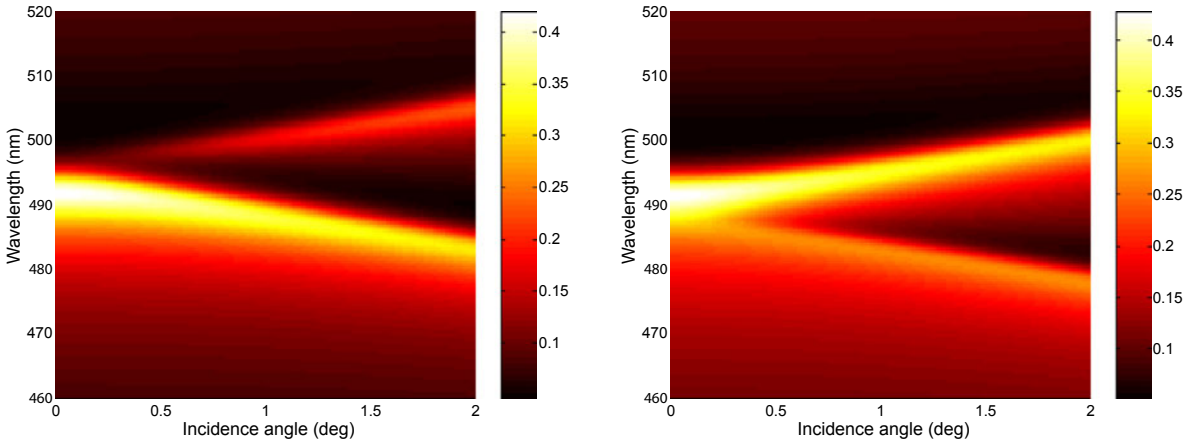

Figure 7.15: Simulation of the reflection efficiency as a function of the incident angle for a corrugated waveguide in air, varying the fill-factor ratio of the grating. The thickness is $d = 130\,\text{nm}$, the grating period $\Lambda = 373\,\text{nm}$ and the grating depth $h = 40\,\text{nm}$. (a) The fill-factor is 55%; (b) the fill-factor is 40%.

his maximum optical fields of the stationary wave in these region will be weakened.
At this point, a corrugated waveguide on a glass substrate has been modeled. This structure has been fabricated and tested with an optical pumping (see Chap. 7.2). The next step in modeling of the structure is to add the electrodes in order to supply the system electrically. Like for the polymer, the influence of the metallic electrodes can be modeled. Since metals are good conductors, they also exhibit light absorbing properties. For the first electrode, aluminium was chosen. The wavelength dependent values of the refractive index and absorption coefficient of aluminium were found in [30]. For the refractive index, the following approximation was taken $n_{Alu} = n_0 + n_1 \cdot \lambda + n_2 \cdot \lambda^2$, with the coefficient $n_0 = 0.82283$, $n_1 = -3.7746$ and $n_2 = 7.3324$. For the absorption coefficients, the fit function is $k_{Alu} = k_0 + k_1 \cdot \lambda + k_2 \cdot \lambda^2$, with the coefficients $k_0 = -0.66679$, $k_1 = 15.065$ and $k_2 = -3.1164$. For the two cases, the wavelength λ is in μm and the fit function are accurate between 400 and 500 nm. In Fig. 7.16(a), we show an illustration of one period of a system with a square metallic grating deposited on a glass substrate. The polymer waveguide is directly deposited on the metal electrode. The polymer waveguide thickness is $d = 100\,\text{nm}$, the grating depth is $h = 50\,\text{nm}$, the grating period is $\Lambda = 326\,\text{nm}$ and the aluminium thickness $l = 100\,\text{nm}$. Figure 7.16(b) shows the dispersion diagram, i.e. the dependence of the reflectivity as a function of the incidence angle. For the incident angle close to $\theta = 0°$ and wavelength $\lambda = 492\,\text{nm}$, we have the signature of the stationary wave. The electric field simulation at incident angle $\theta = 0°$ and wavelength $\lambda = 492\,\text{nm}$ is illustrated in Fig. 7.17 which shows a strong stationary field inside the polymer.
We introduce the second electrode in the system. The first order grating has a direction normal to the surface of the sample and a part of the light created and guided inside the waveguide structure will leave the structure in this direction. For this reason, the second

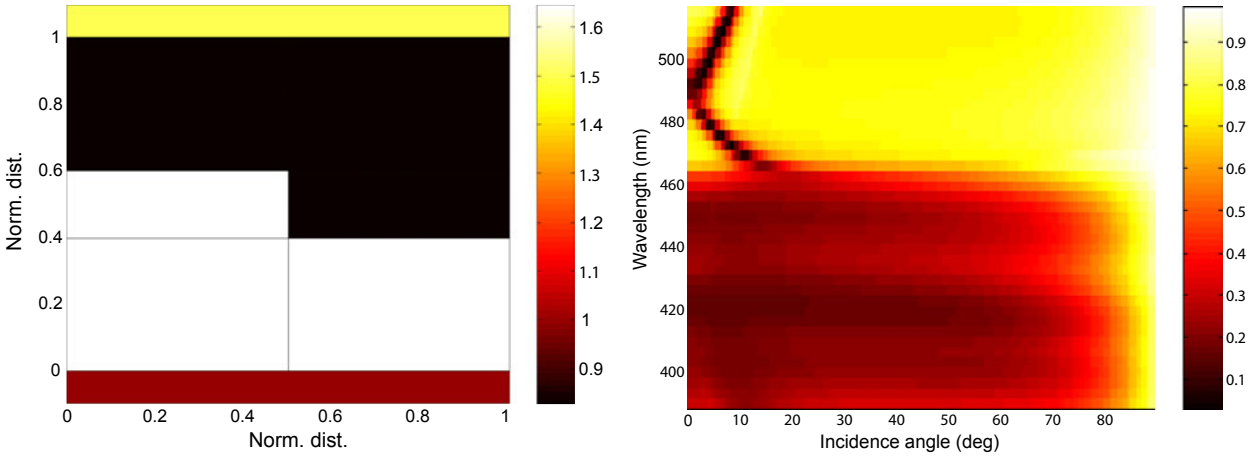

(a) (b)

Figure 7.16: (a) Illustration of one single period of a sample. The polymer corrugated waveguide is deposited on a square metallic grating electrode. (b) Dispersion diagram (reflection efficiency as a function of the incident angle) of this polymer waveguide with thickness $d = 100\,\text{nm}$, grating depth $h = 50\,\text{nm}$, grating period $\Lambda = 326\,\text{nm}$ and aluminium thickness $l = 100\,\text{nm}$.

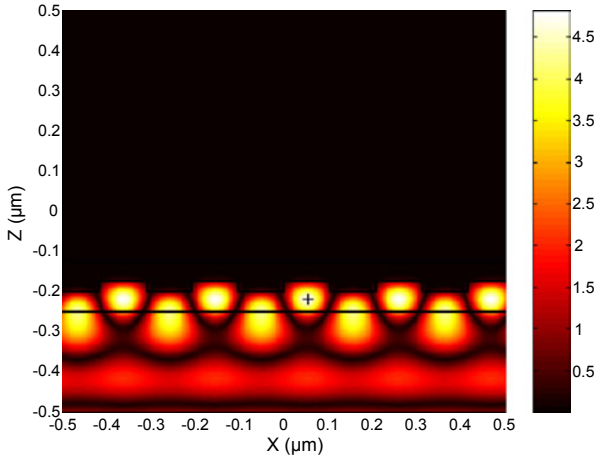

Figure 7.17: Simulation of the electric field intensity at incident angle $\theta = 0°$ and wavelength $\lambda = 492\,\text{nm}$ inside the structure described in Fig. 7.16.

electrode must be transparent. Usually, for the second electrode, the choice for a transparent conducting oxide (TCO) is made. A common transparent electrode used in OLED technology is the indium tin oxide (ITO). In the calculation , the wavelength dependent values of the refractive index and absorption coefficient of ITO as found in [20] were used. For the refractive index, the following fitting curve was taken $n_{ITO} = 2.14 - 1.1765 \cdot (\lambda - 0.390)$. The wavelength λ is in μm and the fit function is accurate to $\Delta n = 0.005$ between 400 and 550 nm. The absorption coefficient was neglected in first approximation since the absorption found in [20] is more than one hundred time smaller than the active polymer absorption for

wavelength higher than $\lambda = 400\,\text{nm}$. The ITO was deposited at the IMT Solar Cell Group,

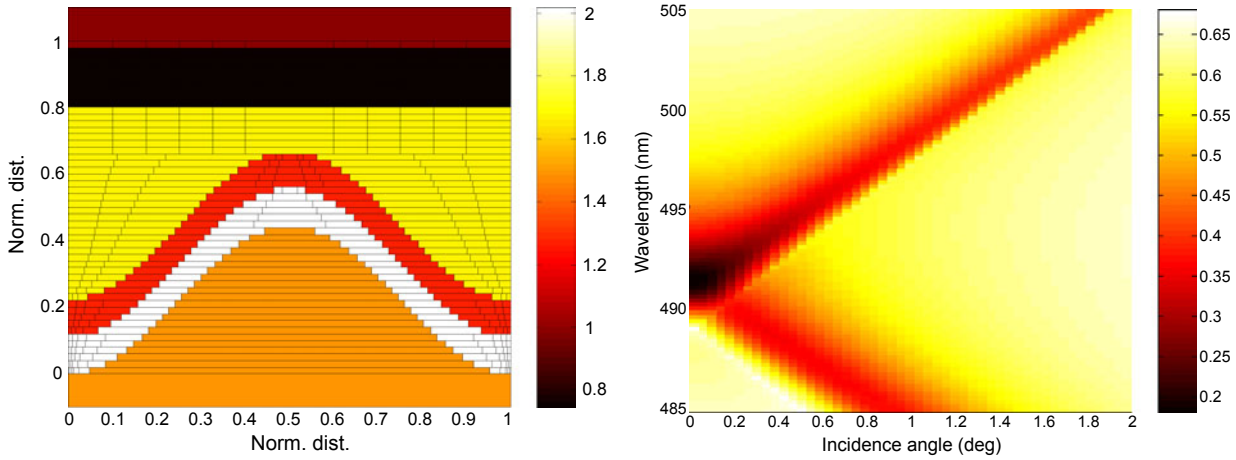

(a) (b)

Figure 7.18: (a) Geometry of a complete sample modeled including the electrodes. It consists of: a glass substrate with sinusoidal shape grating structure with period $\Lambda = 326\,\text{nm}$ and grating depth $h = 120\,\text{nm}$, an ITO and a PEDOT layers of thickness 30 nm each, an active polymer layer (Me-LPPP) of maximum and minimum thickness $h = 160\,\text{nm}$ and $h = 40\,\text{nm}$, respectively, and finally an aluminium electrode with thickness $d = 50\,\text{nm}$. (b) Dispersion diagram (reflection efficiency as a function of the incident angle) of this structure.

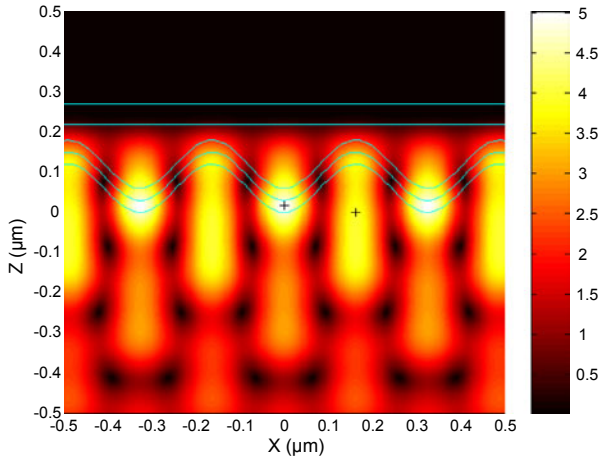

Figure 7.19: Simulation of the electric field intensity at incident angle $\theta = 0°$ and wavelength $\lambda = 492\,\text{nm}$ for the structure described in Fig. 7.18.

with specific deposition procedure. The wavelength dependent values of the refractive index and absorption were controlled and measured ellipsometrically. The obtained values were slightly different from the literature. The fitting curve for the refractive index of ITO from IMT are $n_{ITO} = y_0 + A \cdot E^p$ with $y_0 = 1.6884$, $A = 0.17662$, $p = 0.93556$. The fitting curve

for the absorption coefficient was $k_{ITO} = y_0 + A \cdot E^p$ with $y_0 = 0.058017$, $A = 0.00013608$ and $p = 5.3161$. The value E corresponds to the energy of the incident wave at wavelength λ in μm converted in electron-Volt unit (eV), i.e. $E = (1.239553 \cdot 10^{-6})/(\lambda \cdot 10^{-}6)$. At

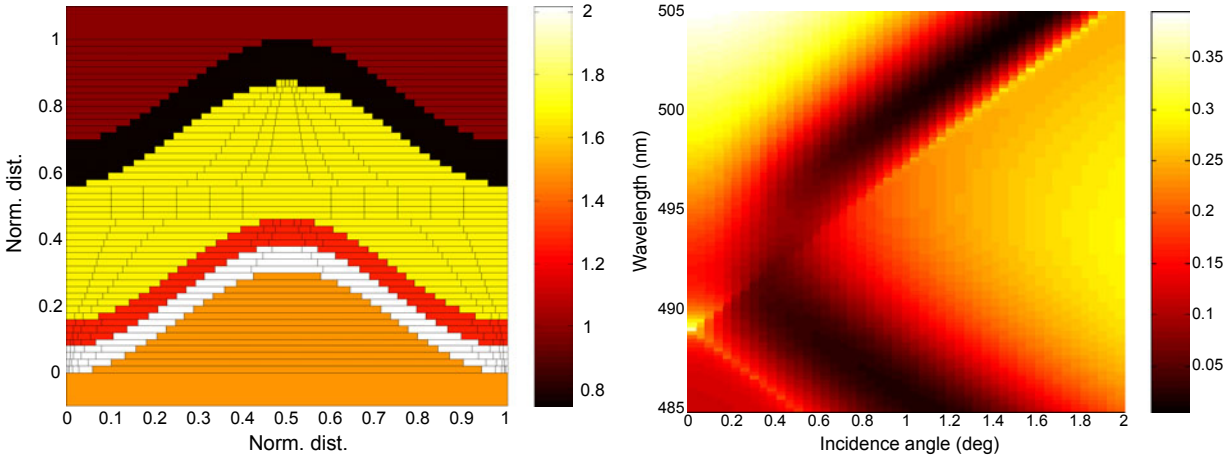

(a) (b)

Figure 7.20: (a) Geometry of a complete sample modeled including the electrodes. It consists of: a glass substrate with sinusoidal shape grating structure with period $\Lambda = 326\,\text{nm}$ and grating depth $h = 120\,\text{nm}$, an ITO and a PEDOT layers of thickness 30 nm each, an active polymer layer (Me-LPPP) of thickness $h = 160\,\text{nm}$, an finally an aluminium electrode with thickness $d = 50\,\text{nm}$. (b) Dispersion diagram (reflection efficiency as a function of the incident angle) of this structure.

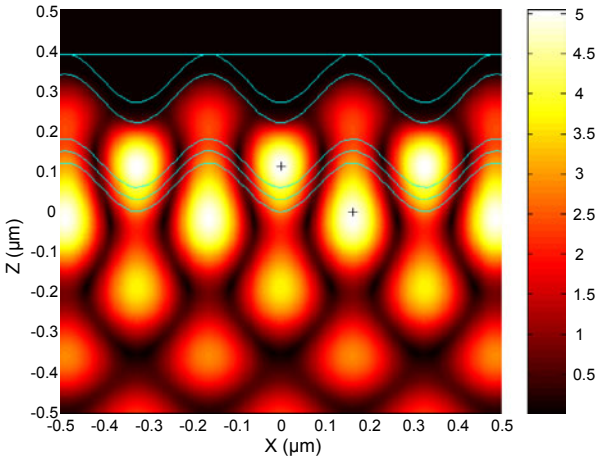

Figure 7.21: Simulation of the electric field intensity at incident angle $\theta = 0°$ and wavelength $\lambda = 492\,\text{nm}$ for the structure described in Fig. 7.20.

this stage, it is important to note here that the refractive index and absorption as well as the resistivity of ITO can be tuned during the deposition process by adjusting the different parameter like oxygen concentration, pressure and deposition rate. After the deposition, different plasma or chemical processes can also influence the absorption and the conductivity

of ITO [20]. In our case, a thermal annealing was applied in order to reduce the resistivity and increase the transparency. The wavelength dependent values of the refractive index and absorption coefficient of PEDOT were found in [32]. For the refractive index, the following fitting function was taken $n_{PEDOT} = a + b \cdot \lambda$ with $a = 1.992$ and $b = -1.4669$. For the absorption coefficient, the fit function is $k_{PEDOT} = k_0 + k_1 \cdot \lambda + k_2 \cdot \lambda^2$ with $k_0 =$, $k_1 =$ and $k_2 =$. For the two cases, the wavelength λ is in μm and the fit functions are accurate between 400 and 550 nm.

At this point, the refractive index and absorption coefficient for the layer assembly, i.e. glass substrate, ITO transparent contact, PEDOT hole transport layer, Me-LPPP active electroluminescent polymer and aluminium top electrode were modeled. The first modeled structure is illustrated in Fig. 7.18(a). It is a glass substrate with a sinusoidal grating with period $\Lambda = 326$ nm and depth $h = 120$ nm. The ITO and PEDOT layers of thickness 30 nm each are deposited onto the grating. Our first assumption is that the active polymer layer deposited by spin-coating technique will have a flat top surface. The maximum and minimum thickness of this layer are $h = 160$ nm and $h = 40$ nm, respectively. The aluminium contact with thickness $d = 50$ nm is deposited on top. This model is optimized for having the mode crossing at wavelength $\lambda = 492$ nm and incident angle $\theta = 0$ on the dispersion diagram shown in Fig. 7.18(b). An electric field simulation for the structure at incident angle $\theta = 0°$ and wavelength $\lambda = 492$ nm is shown in Fig. 7.19. In this design, the maximum of intensity of the stationary field inside the structure is not inside the active polymer material. For this reason, this design is not very effective to produce a stimulated emission inside the polymer layer.

One can also imagine a model where the active layer is thin enough to follow the shape of the grating. This modified structure is illustrated in Fig. 7.20(a). It is a glass substrate with a sinusoidal grating with period $\Lambda = 326$ nm and depth $h = 120$ nm. The ITO and PEDOT layers of thickness 30 nm each are deposited onto the grating. The active polymer layer deposited by spin-coating technique follows the grating shape. The thickness of this layer is $h = 160$ nm. The aluminium contact with thickness $d = 50$ nm is deposited on top. This model is also optimized for having the mode crossing at wavelength $\lambda = 492$ nm and incident angle $\theta = 0$ on the dispersion diagram shown in Fig. 7.20(b). An electric field simulation for the structure at incident angle $\theta = 0°$ and wavelength $\lambda = 492$ nm is shown in Fig. 7.21. As a result, the maximum of the stationary field can be inside the active layer and can produce a stimulated emission.

We can now imagine that the grating shape has not exactly a sinusoidal shape. This is illustrated in Fig. 7.22(a). The original normalized sinusoidal shape of the grating is given by $h/2 * (sin(x - \pi/2) + 1)$. Here the shape of the grating was chosen arbitrarily by the function $h/4 * (sin(x - \pi/2) + 1)^2$. Such a grating shape can happen because of the fabrication method used for the grating (see chapter 3.2). For example, if the grating is over-exposed or developed, the bottom of the sinusoidal grating becomes larger and as a result, the top becomes sharper. In this model, we have a grating with period $\Lambda = 326$ nm and depth $h = 120$ nm directly etched in the glass substrate. The ITO and PEDOT layers of thickness 30 nm each are deposited onto the grating. The active polymer layer deposited by spin-coating technique follows the grating shape. The thickness of this layer is $h = 160$ nm.

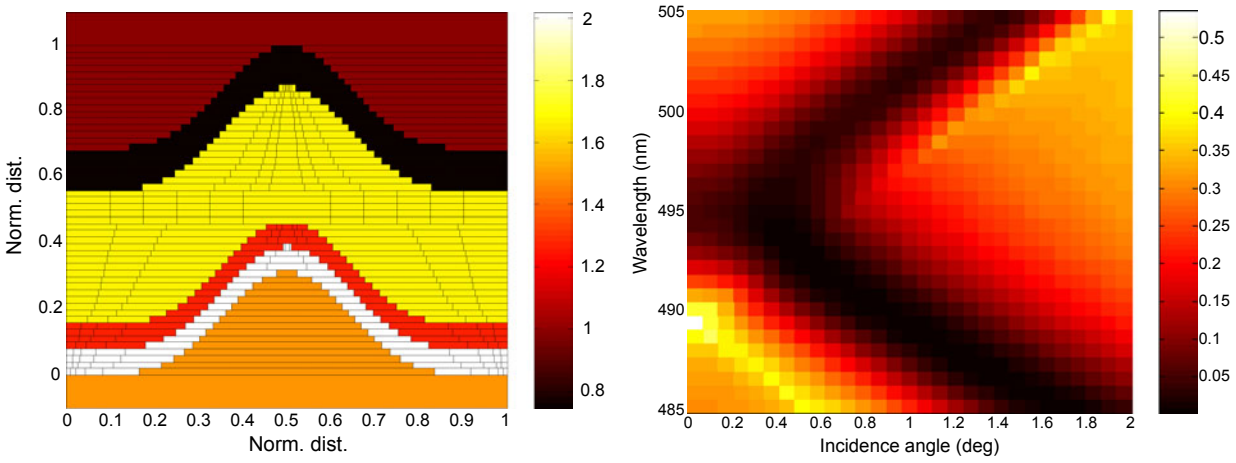

(a) (b)

Figure 7.22: (a) Geometry of a complete sample modeled including the electrodes. It consists of: a glass substrate with sinusoidal shape grating structure with period $\Lambda = 326\,\text{nm}$ and grating depth $h = 120\,\text{nm}$, an ITO and a PEDOT layers of thickness 30 nm each, an active polymer layer (Me-LPPP) of thickness $h = 160\,\text{nm}$, and finally an aluminium electrode with thickness $d = 50\,\text{nm}$. (b) Dispersion diagram (reflection efficiency as a function of the incident angle) of this structure.

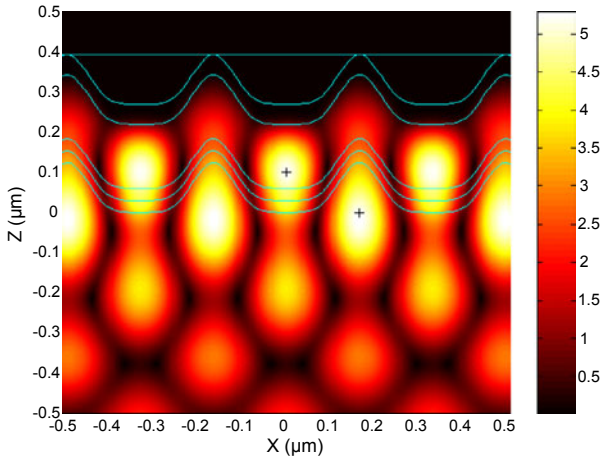

Figure 7.23: Simulation of the electric field intensity at incident angle $\theta = 0°$ and wavelength $\lambda = 492\,\text{nm}$ inside the structure.

The aluminium contact with thickness $d = 50\,\text{nm}$ is deposited on top. This model is also optimized for having the mode crossing at wavelength $\lambda = 492\,\text{nm}$ and incident angle $\theta = 0$ on the dispersion diagram. The dispersion diagram corresponding to the model illustrated in Fig. 7.22(a) is shown in Fig. 7.22(b). One sees a better definition of the optical mode at incident angle $\theta = 0°$. The electric field simulation at incident angle $\theta = 0°$ and wavelength $\lambda = 492\,\text{nm}$ is shown in Fig. 7.23. The intensity maximum of the stationary field inside the structure is inside the active polymer material. Therefore, this design is very effective to

produce a stimulated emission inside the polymer layer.

7.2 Practical work

Like for the modeling part, we follow a step by step procedure to confirm the results of the simulations. First tests were made by depositing thin layers of the active polymer with different thickness on different gratings. The samples were photo-pumped with a laser at $\lambda = 405\,\text{nm}$. We compared the fluorescence spectra with the case where the polymer was spun on a simple flat glass substrate. A flexible polycarbonate foil with hot embossed grating was tested but the solvent used to dilute the polymer dissolved the surface relief grating. This substrate was replaced by a grating etched in glass (see chapter 3.2). The results of the experiments are given in chapter 7.3.
The transparent electrodes were deposited directly on the grating that was etched into glass. Due to the small grating period needed to obtain the DFB regime, it was technically difficult to fabricate a deep grating in glass. When the grating originated in photoresist is etched into glass, the transfer rate is around 0.7, i.e. the grating height is typically reduced by 30 percent. Therefore, a replication method described in chapter 3.4 was used. The method allows to replicate precisely the grating profile from the photoresist substrate in a UV curing polymer. After replication and curing, the polymer is resistant to the solvent.

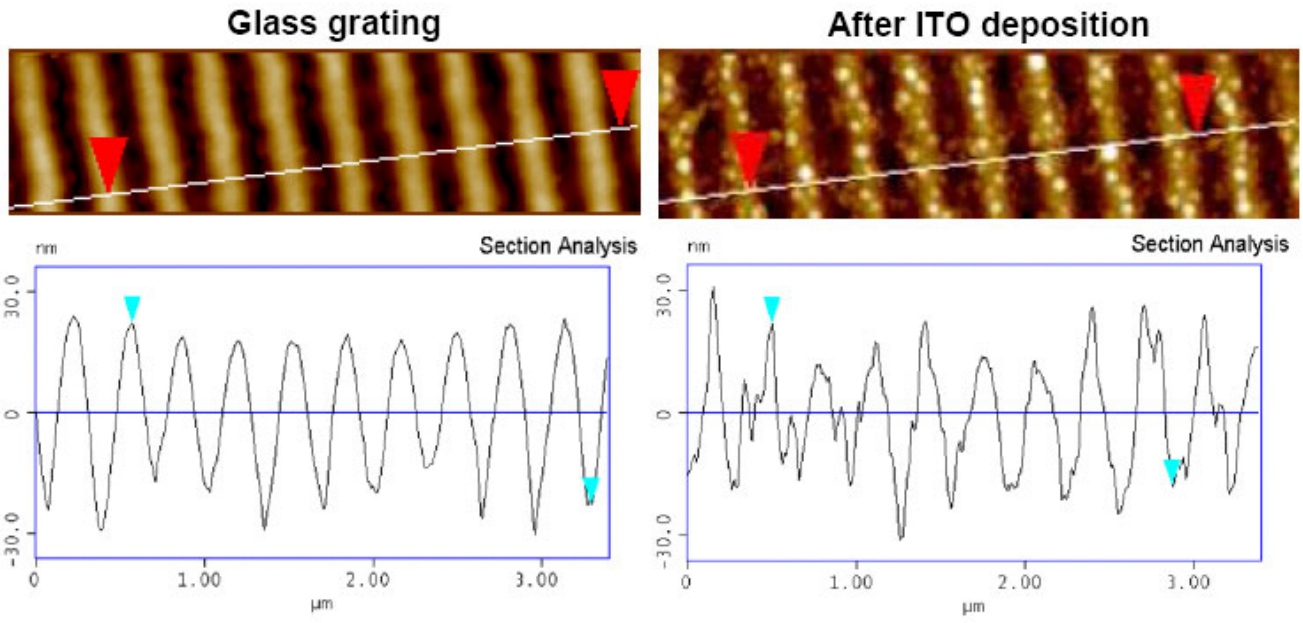

Figure 7.24: Atomic force microscope image of the surface of a glass grating before and after ITO deposition.

The ITO layer as transparent conducting electrode was chosen for its good electrical characteristics and optical properties (transparency) at the wavelength of emission of the polymer. It is very important from the optical point of view that the surface of each layer is very smooth. The roughness of the surface induces light scattering and losses. Nevertheless, some samples were found to have quite rough surfaces depending on deposition conditions. Atomic force microscope images of different surface are shown in Figs. 7.24 and 7.25. In the

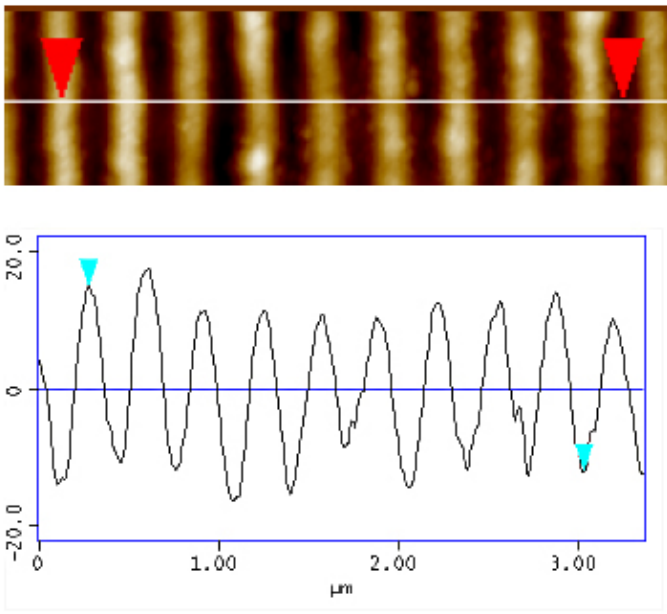

Figure 7.25: Atomic force microscope image of the surface of a glass grating after ITO deposition.

worst case, the roughness was ±5 nm. These AFM images show that the surface structure of the ITO layer can dramatically change depending of the condition of deposition.
A possible problem when fabricating OLED are short-circuits between the thin layers. For instance, if a small dust particle or a scratch induce a default or a change in the layer thickness, it can create a short circuit between the electrodes. If the electric field is too high in this region, the active polymer can not dissipate the energy and finally burn. The sample is destroyed. To overcome this problem, the sample was divided into several smaller independent OLED as illustrated in Figs. 7.26(c). The complete procedure used for the deposition

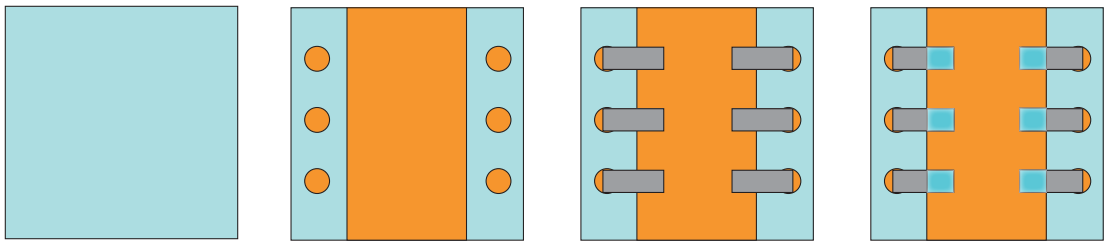

Figure 7.26: Procedure for the sample preparation: (a) cleaning of a glass substrate; (b) deposition of the ITO transparent electrode through a metallic mask; (c) spincoating of the hole conducting layer and active polymer layer and finally depositing the last metallic contact layer. (d) By applying a voltage between ITO and the metal contact, the regions where all the layers are superimposed light on.

of the OLED layers is illustrated in Figs. 7.26(a)-(d). One begins with a glass substrate cleaning (Fig. 7.26(a)). The grating is replicated in an UV curing polymer directly on the clean substrate. Afterwards the thin ITO transparent electrode is deposited over the grating

through a shadow mask (Fig. 7.26(b)). To improve the optical transparency and the electric conductivity and to permit a good adhesion with the following layer, the ITO layer must be treated with an oxygen plasma and thermally annealed with a temperature ramp. The last steps were done in controlled environment. The active polymer and metallic electrode are very sensitive to oxygen and moisture and degrade rapidly under normal conditions. It was then important to control these parameters during the fabrication process. A glove box at CSEM with controlled nitrogen atmosphere was used. The hole conducting layer and the active polymer layer were deposited by spin-coating under nitrogen atmosphere. Finally the aluminium contact layer was evaporated through a shadow mask on the top (Fig. 7.26(c)). To prevent the metal electrode to oxidize when the sample is removed from the glove box, an encapsulation was done. This encapsulation consists of a thin glass substrate glued on the top of the sample. Figures 7.27(a) and 7.27(b) show SEM pictures of a complete sample with all layers, including the contact layers and encapsulation layer. We can see that the

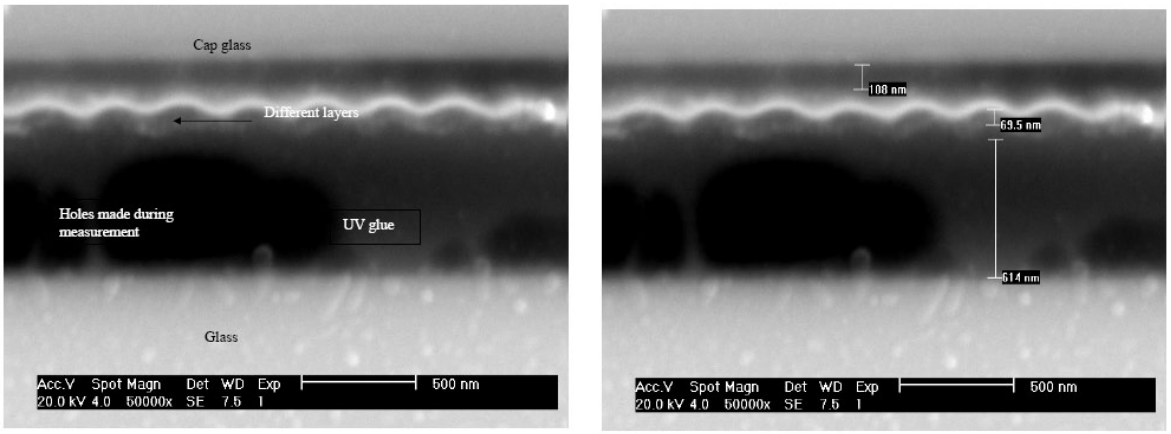

(a) (b)

Figure 7.27: (a) and (b) SEM measurement of the cut profile of an OLED deposited on grating substrate. One observes that the grating profile is conserved after the layers are deposited.

top metallic contact follows the grating shape. It means that the thin layers deposited by spin-coating over the grating do follow the grating shape.

7.3 Optical pumping

The principle of the measurement done with optical pumping is illustrated in Fig. 7.28. The

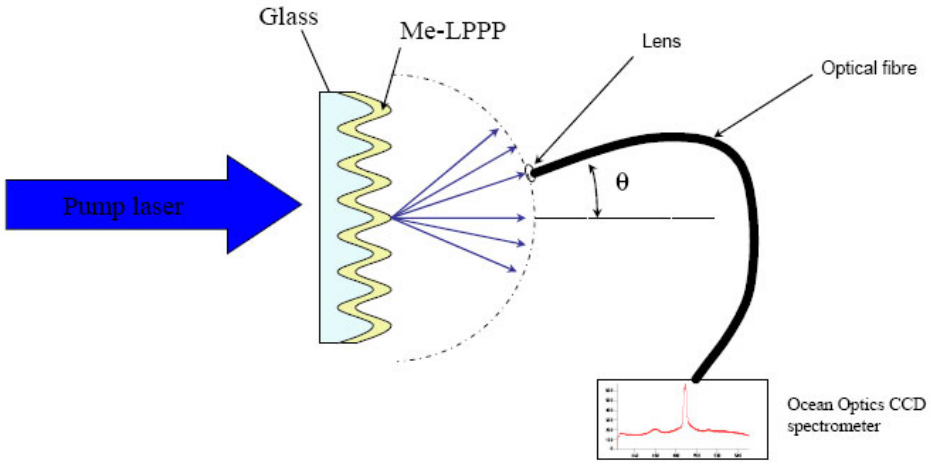

Figure 7.28: Illustration of the measurement setup for the optically pumped sample.

active optical layer deposited on the grating is optically pumped with a laser. The pump laser must have a wavelength below the emission of the active polymer. In our case, a 405 nm diode laser was used. The angular dependent emission from the sample is measured with an Ocean Optics spectrometer. It is well known that the active polymer can not hold strong light intensity without degradation and bleaching. To avoid that the active layer degenerates during the laser beam exposure, the measurement time has to be restricted. A programmable shutter was used between the laser beam and the sample. The spectrum measurement was triggered with the shutter. Figure 7.29 shows a test sample with an active polymer layer (Me-LPPP) optically pumped with the laser diode at 405 nm (violet). The photoluminescent light is green-blue. In Fig. 7.30(a) one sees the emitted spectra for

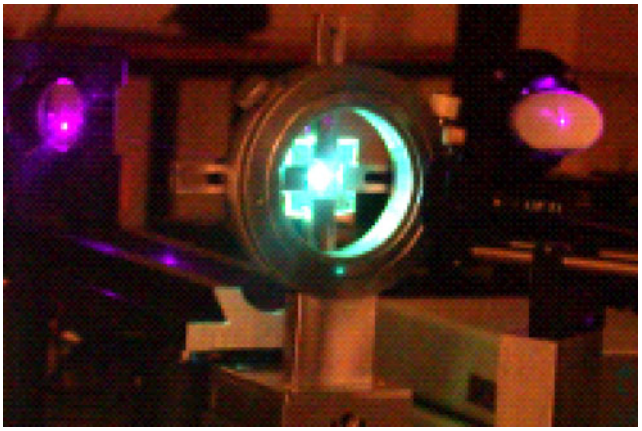

Figure 7.29: Picture of the sample optically pumped with a laser at 405 nm.

different angles. Two large peaks of electroluminescence at 465 nm and 491 nm are not dependent on the angle of observation. Induced peaks of photoluminescence are seen between

the two principal peaks. They are angular dependent. The maxima of the induced peaks are not at 491 nm as it was calculated. The grating period was controlled with an AFM and was close to the calculated value within ±5 nm. The thickness of the active layer revealed to be thinner than modeled. With a layer thickness too thin, one creates a cut-off at a given wavelength. An optical mode with a larger wavelength could not exist anymore in the waveguide. Figure 7.30(b) shows the corresponding dispersion diagram with the peak of the emitted intensity reported at each angle of the measurement. The crossing of the optical mode at angle $\theta = 0°$ and wavelength 491 nm is not obtained. To move the peak to 491 nm,

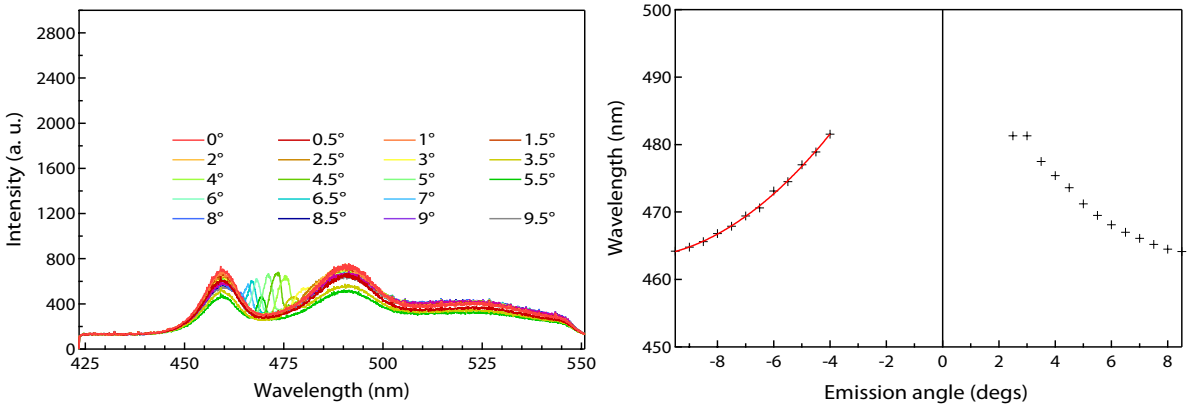

(a) (b)

Figure 7.30: (a) Intensity measurement as a function of the emission angle for a sample with an active layer that is too thin. (b) Dispersion mode for the peak intensity at each angle.

the layer thickness had to be increased. The results for an adapted layer thickness is shown in Fig. 7.31(a). In Fig. 7.31(b) one sees that the peak at $\theta = 0°$ is now around 497 nm, i.e. a bit above the desired wavelength. This can be explained by the grating period being some nanometers too large or by the layer thickness being this time slightly too thick. For

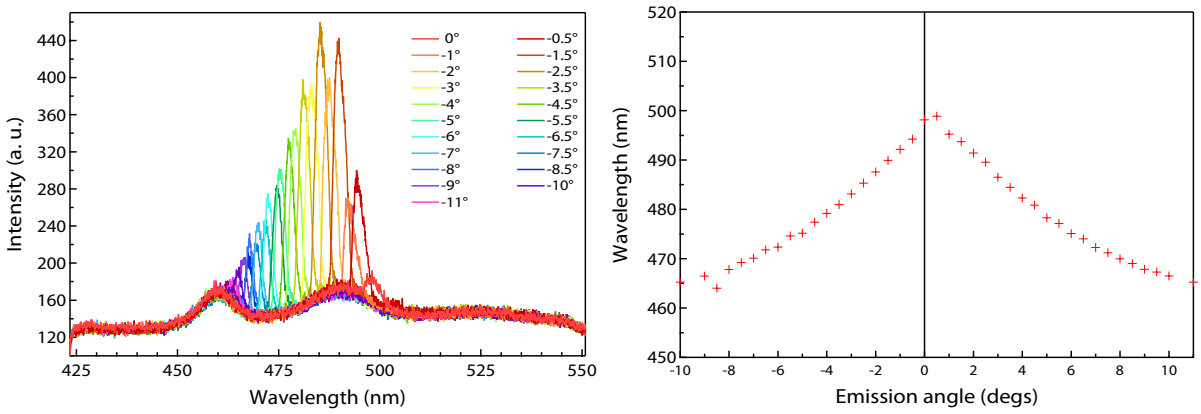

(a) (b)

Figure 7.31: (a) Intensity measurement as a function of the emission angle for a sample with an good dimensioned active layer. (b) Dispersion mode for the peak intensity at each angle.

the two sample in Figs. 7.30 and 7.31, we also measured the optical emission as a function

of the optical pump power. Figures 7.32(a) and 7.32(b) show the results. As expected, we could not see any lasing effect. If a lasing effect had occurred, the intensity in the induced peak region would have increased faster than for the photoluminescent background. To see the lasing effect, we should have used a pulsed optical source like a fs-laser. With this kind of pumping, one can increase the incident pumping power without burning the sample.

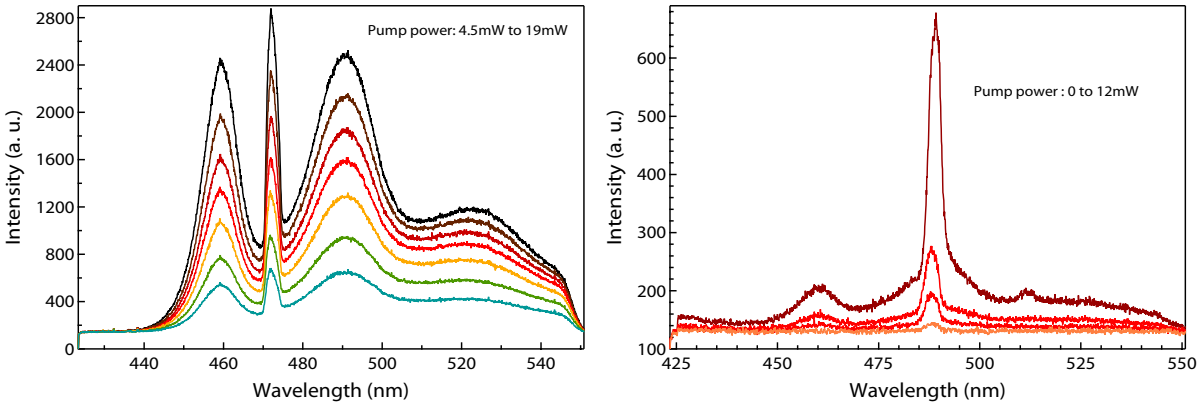

(a) (b)

Figure 7.32: Measurement of the emission intensity as a function of the pump power for the two samples at normal angle (0°). (a) The first sample has an active layer that is too thin; (b) the second sample has a correctly dimensioned active layer.

For the next part of this research, we replaced the Me-LPPP with the F8, another promising active polymer. The F8 active polymer has also different peaks of luminescence in the blue region of the spectrum. As illustrated in Fig. 7.33, the peaks for an optically pumped planar layer on a glass substrate are found at 440 nm, 465 nm and 495 nm. To

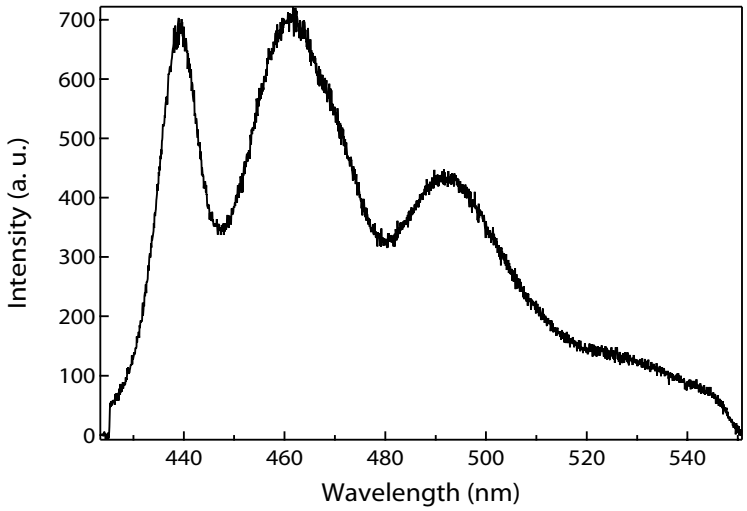

Figure 7.33: Emission measurement of a planar thick layer of active polymer F8 optically pumped. The peaks are around 440 nm, 465 nm and 495 nm.

model this active polymer, we used the data published in [46]. One gets for the refractive index $n^2 = 2.6732 - 0.10677/\lambda^2 + 0.042018/\lambda^4$ and the absorption coefficient $\alpha =$

$0.38354\exp(-9.1247\lambda) + 0.0017941$ of the active polymer F8. It must be pointed out that these values for the refractive index and absorption coefficient were measured with a layer thickness of around 1 μm. As it was underlined for the Me-LPPP, we must keep in mind that these values can change when very thin layers are used. The modeling of the DFB structure with the new active polymer had to be adapted. The main difference was the peak wavelength as seen in Fig. 7.33, and also the weaker absorption in the blue region, allowing to chose a lower wavelength of emission. The modeling gives a mode crossing in the dispersion diagram at 438 nm at $\theta = 0$ for the following sample size: ITO thickness 30 nm, PEDOT thickness 20 nm, F8 thickness 120 nm, grating period 275 nm, grating height 60 nm.To highlight the differences between the planar OLED and when the layers are deposited on a grating structure, a set of samples were fabricated at the same time either on flat substrates or on grating substrates. This guaranties that the characteristics of the fabricated samples are comparable. Four different active polymer thicknesses were chosen to see the effect on photoluminescence and electroluminescence. The layer thicknesses were 80 nm, 90 nm, 100 nm and 120 nm. Both types of samples were optically pumped as illustrated in Fig. 7.35. The pumping is done through the substrate since the aluminium contact is thick enough to block all the light. The arrangement of the different layers of the samples allows us to separate each sample in 4 different areas. The first two areas were outside the ITO contact with or without aluminium contact. The third and forth area were inside the ITO area, again with or without aluminium contact.
Figure 7.34 shows the normal emission of the optically pumped planar OLED sample. The active layer thickness is 90 nm. One sees that when the sample is pumped in an area with

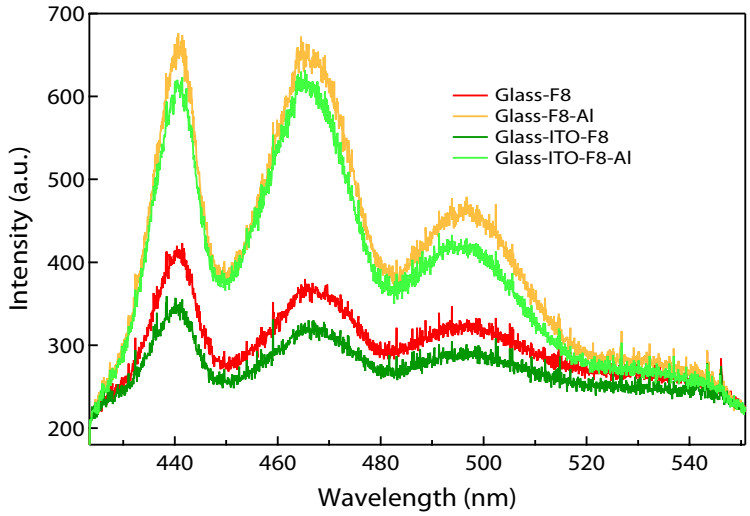

Figure 7.34: Measurement of optically pumped flat OLED sample with contacts. The active layer is a 90 nm thick F8 polymer.

an aluminium contact, the amplitude of the measured photoluminescence increases. This is easily understood because the reflection of the pump laser on the metal surface increases the pumping in the region of interest. We can also see a decrease of the measured photoluminescence when the sample is pumped where we have the ITO electrode. This can be explained by the absorption or the diffusion of the ITO electrode. Since the absorption in the ITO

should be wavelength dependent, we would expect a bigger effect in the lower wavelength range, but it is not clearly demonstrated here.
The same experiment was done with the samples with grating. Here again, the pumping had to be done as illustrated in Fig. 7.35. The grating effect was measured by recording the emitted spectrum at different angles. The results for active polymer thicknesses of 120 nm

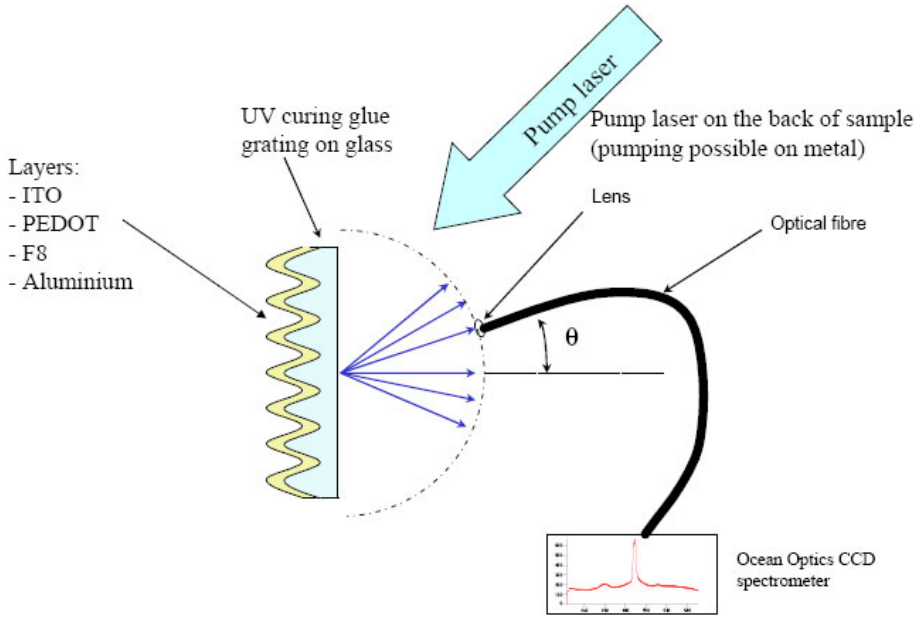

Figure 7.35: Illustration of the measurement setup for the optically pumped sample with contacts.

and 100 nm are given in Fig. 7.36. We expected that the peak for angle $\theta = 0°$ was around

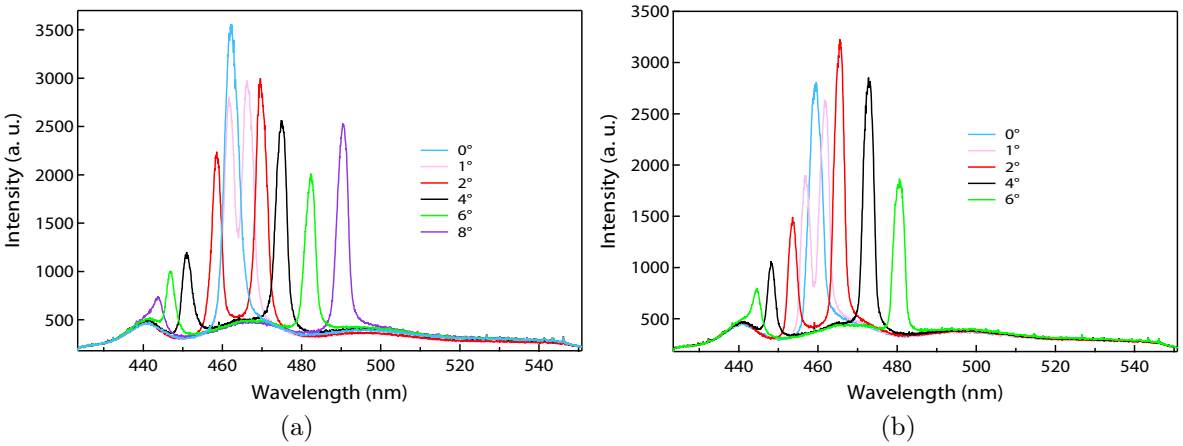

Figure 7.36: Measurement of angular dependence emission of an optically pumped sample outside the ITO area with different F8 active polymer thicknesses, (a) 120 nm and (b) 100 nm.

440 nm. However it was found at 457 nm. The problem was rapidly identified when the grating period was measured. The period was 295 nm measured with an AFM instead of the 275 nm assumed in the model. The difference between the ideal and measured period

explains the shift of the peaks. In both cases, one observes a single and larger peak for an angle $\theta = 0°$. It is the combination of the two optical modes. For the other angle, there is always a couple of peaks that represent the two branches of the guided mode. One sees the effect of the active layer thickness in the shift of the different peaks. For an active layer thickness of 120 nm, the maximum of emission for angle $\theta = 0°$ is slightly above 460 nm. The wavelength of this peak decreases below 460 nm for an active layer thickness of 100 nm. The results for the active polymer thicknesses of 90 nm and 80 nm are presented in Fig. 7.37. Here again, one observes a decrease of the wavelength of the maximum of emission for angle

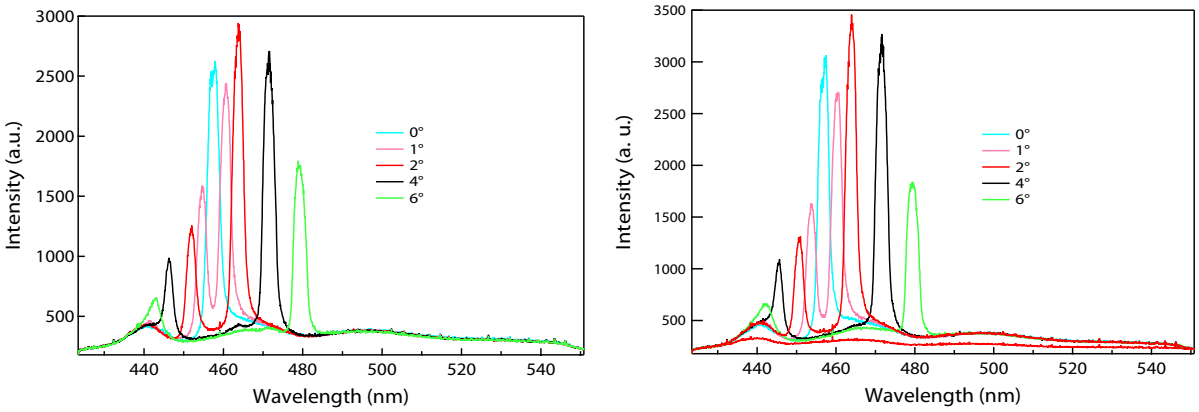

Figure 7.37: Measurement of angular dependence emission of an optically pumped sample outside the ITO region with different F8 active polymer thicknesses, (a) 90 nm and (b) 80 nm.

$\theta = 0°$.

Although the grating period does not strengthen the chosen wavelength, the comparison between the case without and with grating illustrated in Fig. 7.38 shows the strong effect created by the grating. The guided light and the DFB effect inside the structure increase strongly the active polymer emission. Figure 7.39 shows the measurement of the angular dependence emission of an optically pumped sample in region with ITO. One observes a widening of the different peaks. This widening is explained by an increase of the absorption of a layer. In our case, the introduction of the ITO layer is responsible. Here again, the problem can be the absorption of the ITO and the surface roughness of the ITO creating scattering. The scattering induces a broadening.

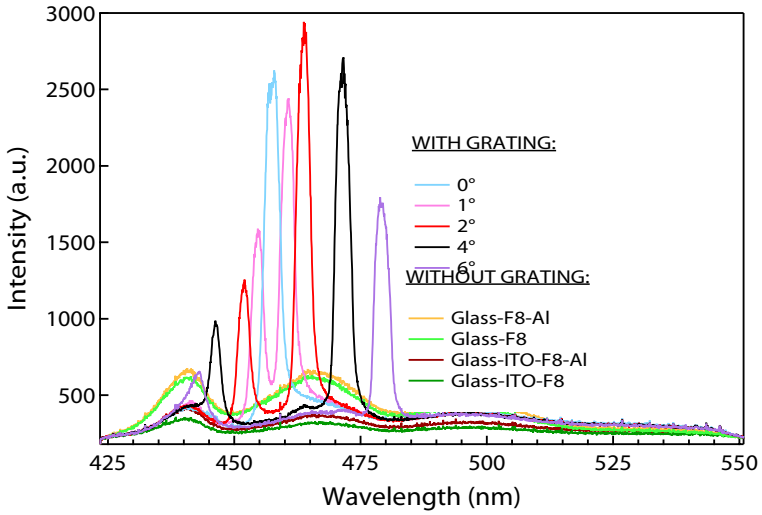

Figure 7.38: Comparison measurement of angular dependence emission of an optically pumped sample on flat substrate and grating substrate for an F8 active layer of 90 nm.

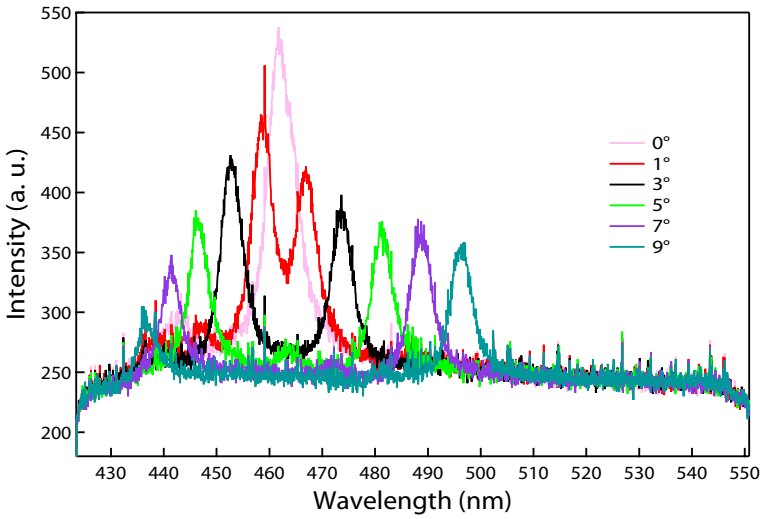

Figure 7.39: Measurement of angular dependence emission of an optically pumped sample in region with ITO.

7.4 Electrical pumping

The same range of samples, i.e. OLED on flat substrate (see Fig. 7.40) and OLED on

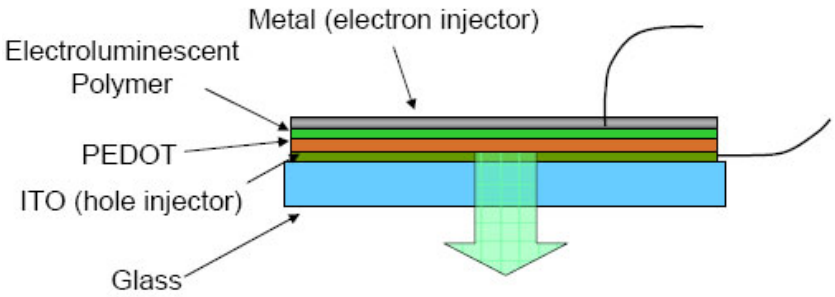

Figure 7.40: Illustration of an OLED sample.

gratings (see Fig. 7.41) with different active layer thickness were used. Instead of an optical

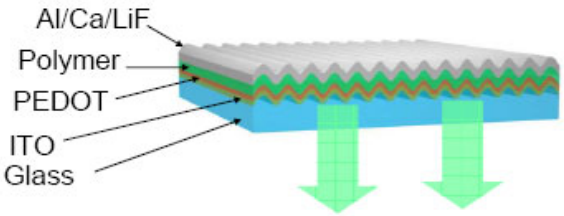

Figure 7.41: Illustration of an OLED sample.

pumping, the sample were simply switched on electrically by applying a positive voltage between the ITO layer (+) and the metal contact (-). The contact on ITO could be done with a crocodile clip while the contact on the metal contact of 100 nm thickness was more problematic. The thin metallic layer was very sensitive to scratches. Once the layer was damaged, it was rapidity oxidized and then difficult to obtain good electric contact. A zebra strip applied on the side of the sample allows to have an electric contact with the metal without damaging the sample.
We noticed that in order to have enough light from the OLED structure, we had to increase the voltage up to 10 V . As the sample were not sealed very effectively on the side, the life time of the sample was considerably reduced. The sample was degrading gradually from the side of the emissive region. To reduce this effect, a pulsed voltage was applied in order to allow the emissive region to cool down between each pulse. When reducing the pulse width, the pulse voltage could also be increased without break down of the samples. Figure 7.42 shows a comparison between optical and electrical pumping for the case of a flat OLED with active layer thickness of 120 nm. The different wavelength of emission are still present. The intensity of emission of the lower wavelengths seems to be attenuated.
Finally, the samples with a grating substrate were measured when switched on electrically. Figure 7.43 shows the measurement of angular dependent emission on electrically driven sample on grating substrate for an F8 active layer of 120 nm. The peaks are dramatically

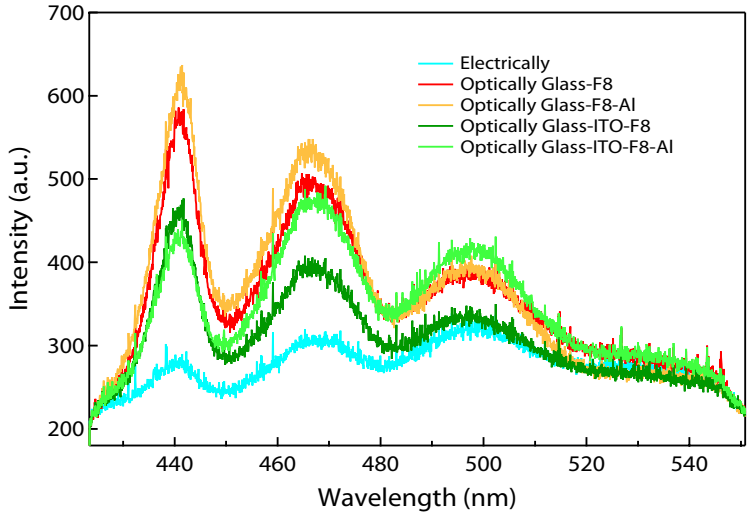

Figure 7.42: Comparison of measurement of optically and electrically driven flat OLED sample. Active layer is a 120 nm thick F8.

reduced from the case when the sample is optically pumped. Nevertheless, even if the effect is small, one sees the angular dependence of the emission. There are several reason why the sample are working badly. It seems that the transparent conductive electrode is a key

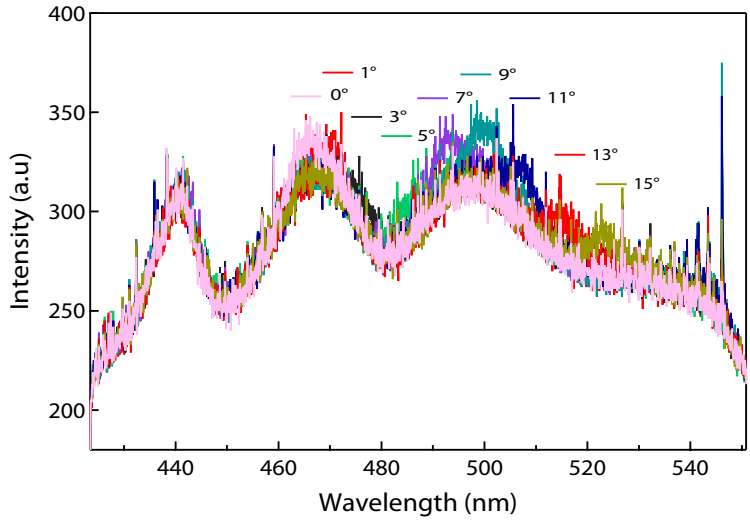

Figure 7.43: Measurement of angular dependence emission on electrically driven sample on grating substrate for an F8 active layer 120 nm.

point in the last results, some further work are proposed. Due to our use of very thin layer of ITO, it would be necessary to have a better definition of the optical refractive index and absorption of such a thin ITO layer. A detailed study of the effect of thermal annealing on ITO resistivity and absorption for thin layers would also be necessary. Finally, as seen in some AFM pictures of ITO layer, surface roughness can appear. This surface roughness is not a problem in solar cells since light diffusion can increase the efficiency. In our case, smooth surfaces must be guaranteed to allow the light to be guided and to have optimal optical properties.

Chapter 8

Conclusion

Who was not once amazed by the beautiful and iridescent color of a peacock, a butterfly or a beetle? How Nature is doing this? We were interested to understand and to reproduce some of the amazing reflection properties of animals in Nature. The SEM pictures of the structure of these animals show a frequent combination of periodic or pseudo-periodic elements such as interference filters like multilayer reflectors with micro- and nano-structures like microlenses or gratings. Interpretation of these optical effects are based on numerical simulations. Different rigorous and approximative methods like the Fourier modal method and ray tracing were used to model the structure combining micro- and nano-optical elements. While the simulations of some of these structures have already been realized, only few elements are fabricated. The standard technology to fabricate such elements revealed to be expensive and not very adapted to reproduce such effects. For instance, evaporation technique that produce interference filters or reflectors are usually using material with large refractive index difference. Periodic multilayers fabricated with such material allow a narrow range of wavelengths to be reflected. In nature, the structure usually produce larger reflected spectrum with material with smaller refractive index difference and can reach a high efficiency by using large number of layers. Structures with a higher refractive index difference also exist in Nature, for example in some butterfly were the lower refractive index material is replaced by air, giving rise to high reflection efficiency for a small number of layer. In this case, a statistical orientation of the nano-scale reflecting elements can broaden the reflecting spectra. Another difference between elements fabricated with standard technology and element found in Nature are the combination of different optical element such as multilayer reflectors and periodic micro- or nano-structures. These combination giving the possibility to have a strong optical effect for a large range of viewing angles and spectra.
For these reasons, our choice was given to polymer structures. Since fluorescent material are easily soluble in polymer solution these material could also be introduced in the structures. Cavity effects and stationary field were seeked in order to enhance or modify the emission of the polymer. In particular polymer light emitting diode in a distributed feedback regime, with the active conductive polymers me-LPPP and F8, were realized and tested.
The technology we used, i.e. fabrication of low-cost polymer multilayer reflector and replication of micro- and nano-structure allow to directly superimpose these different elements. Poly(vinyl alcohol) and poly (N-vinycarbazole) with refractive indices of 1.56 and 1.72, re-

spectively, at a wavelength of 500 nm were used to fabricate the polymer multilayer reflectors. The micro-optical elements used were: microlenses with diameter between 32 μm and 250 μm and around 20 μm height; prisms with 50 μm period and 25 μm height. These elements were replicated in an optical adhesive with refractive index $n \approx 1.56$.

With the fabricated elements, we could show the basic principles and identify the limitation of the polymer technology. We could do it but nature is still much better! The reason is that structures found in nature are more complex, less ordered at large scale and integrates different scale of periodicity. To realize samples with properties more close to such found in nature, statistical variation of optical element dimension such as the grating period and orientation, and addition of light diffuser could give some promising effects.

Acknowledgements

Thanks to:

- Prof. Herzig for giving me the opportunity to work in his group and letting me a lot of freedom in my research.
- Martin Salt for his friendship and humor, and for introducing me to the world of optics, photonics and organic LEDs.
- CSEM with C. Winnewisser and A. Stuck for projects collaborations and funding.
- Toralf Scharf for guiding me during the last two years of my thesis and helping me with important matter like publications and conference presentations.
- Prof. François Flory for accepting to be member of my thesis jury, his interest in my work and his positive feedback.
- All applied optics group members for their friendship and help. Particular thanks to Olivier, Patrick, Iwan and Wataru for their advices in general computer problems, technology and fabrication, English writing and for sharing different aspects of the life at the institute of microtechnology.
- My parents and family...

Bibliography

[1] Colour and vision research labs. "http://www.cvrl.org/".

[2] International commission on illumination website. "http://www.cie.co.at/".

[3] Nexant inc. website. "http://nexant.ecnext.com/coms2/gi_0255-222/Polyvinyl-Alcohol.html".

[4] Norland products website. "http://www.norlandprod.com/adhesives/adhindex.html".

[5] Oregon medical laser center. "http://omlc.ogi.edu/".

[6] A. L. Alvarez, J. Tito, M. B. Vaello, P. Velasquez, R. Mallavia, M. M. Sanchez-Lopez, and S. Fernandez de Avila. Polymeric multilayers for integration into photonic devices. *Thin Solid Films*, 433(1-2):277–280, 2003.

[7] P. Andrew, G. A. Turnbull, I. D. W. Samuel, and W. L. Barnes. Photonic band structure and emission characteristics of a metal-backed polymeric distributed feedback laser. *Applied Physics Letters*, 81(6):954–956, 2002.

[8] S. Berthier. *Iridescences, les couleurs physiques des insects.* Springer-Verlag, 2003.

[9] F. W. Billmeyer. *Textbook of Polymer Science.* Wiley-Interscience, 1984.

[10] P. Blattner. *Light fields emerging from periodic optical microstructures.* PhD thesis, University of Neuchâtel, 1999.

[11] T. M. Brown, R. H. Friend, I. S. Millard, D. J. Lacey, J. H. Burroughes, and F. Cacialli. Lif/al cathodes and the effect of lif thickness on the device characteristics and built-in potential of polymer light-emitting diodes. *Applied Physics Letters*, 77(19):3096–3098, 2000.

[12] J. H. Burroughes, D. D. C. Bradley, A. R. Brown, R. N. Marks, K. Mackay, R. H. Friend, P. L. Burns, and A. B. Holmes. Light-emitting diodes based on conjugated polymers. *Nature*, 347(6293):539–541, 1990.

[13] V.-E. Choong, S. Shi, J. Curless, and F. So. Bipolar transport organic light emitting diodes with enhanced reliability by lif doping. *Applied Physics Letters*, 76(8):958–960, 2000.

[14] J. J. Cowan. Aztec surface-relief volume diffractive structure. *Journal of the Optical Society of America A: Optics, Image Science, and Vision*, 7(8):1523–1538, 1990.

[15] R. H. Friend, R. W. Gymer, A. B. Holmes, J. H. Burroughes, R. N. Marks, C. Taliani, D. D. C. Bradley, D. A. D. Santos, J. L. Bredas, M. Logdlund, and W. R. Salaneck. Electroluminescence in conjugated polymers. *Nature*, 397:121–128, 1999.

[16] A. S. Glassner. *An Introduction to Ray tracing*. Morgan Kaufmann, 1989.

[17] B. Gralak, G. Tayeb, and S. Enoch. Morpho butterflies wings color modeled with lamellar grating theory. *Optics Express*, 9(11):567–578, 2001.

[18] G. Heliotis, R. Xia, D. D. C. Bradley, G. A. Turnbull, I. D. W. Samuel, P. Andrew, and W. L. Barnes. Blue, surface-emitting, distributed feedback polyfluorene lasers. *Applied Physics Letters*, 83(11):2118–2120, 2003.

[19] K. Ihm, T.-H. Kang, K.-J. Kim, C.-C. Hwang, Y.-J. Park, K.-B. Lee, B. Kim, C.-H. Jeon, C.-Y. Park, K. Kim, and Y.-H. Tak. Band bending of lif/alq[sub 3] interface in organic light-emitting diodes. *Applied Physics Letters*, 83(14):2949–2951, 2003.

[20] H. Kim, C. M. Gilmore, A. Pique, J. S. Horwitz, H. Mattoussi, H. Murata, Z. H. Kafafi, and D. B. Chrisey. Electrical, optical, and structural properties of indium–tin–oxide thin films for organic light-emitting devices. *Journal of Applied Physics*, 86(11):6451–6461, 1999.

[21] Lambda Research Corporation. *User's Manual*, 3.0 edition, 2002.

[22] L. Li. New formulation of the fourier modal method for crossed surface-relief gratings. *JOSA A*, 14(10):2758–2767, 1997.

[23] M. D. McGehee and A. J. Heeger. Semiconducting (conjugated) polymers as materials for solid-state lasers. *Advanced Materials*, 12(22):1655–1668, 2000.

[24] M. G. Moharam and T. K. Gaylord. Diffraction analysis of dielectric surface-relief gratings. *Journal of the Optical Society of America*, 72(10):1385–1392, 1982.

[25] M. G. Moharam, E. B. Grann, D. A. Pommet, and T. K. Gaylord. Formulation for stable and efficient implementation of the rigorous coupled-wave analysis of binary gratings. *Journal of the Optical Society of America A: Optics, Image Science, and Vision*, 12(5):1068–1076, 1995.

[26] M. G. Moharam, D. A. Pommet, E. B. Grann, and T. K. Gaylord. Stable implementation of the rigorous coupled-wave analysis for surface-relief gratings: enhanced transmittance matrix approach. *Journal of the Optical Society of America A: Optics, Image Science, and Vision*, 12(5):1077–1086, 1995.

[27] C. Nave. Hyperphysics (©c.r. nave, 2006). "`http://hyperphysics.phy-astr.gsu.edu`".

[28] G. Niederer. *Resonant grating filters for microsystems.* PhD thesis, University of Neuchâtel, 2004.

[29] P. Nussbaum, R. Völkel, H. P. Herzig, M. Eisner, and S. Haselbeck. Design, fabrication and testing of microlens arrays for sensors and microsystems. *Pure and Applied Optics: Journal of the European Optical Society Part A*, 6(6):617–636, 1997.

[30] E. D. Palik, editor. *Handbook of Optical Constants of Solids.* Academic Press, 1985.

[31] A. R. Parker and Z. Hegedus. Diffractive optics in spiders. *Journal of Optics A: Pure and Applied Optics*, 5(4):S111–S116, 2003.

[32] L. Pettersson, T. Johansson, F. Carlsson, H. Arwin, and O. Inganas. Anisotropic optical properties of doped poly(3,4-ethylenedioxythiophene). *Synthetic Metals*, 101(1-3):198–199, May 1999. International Conference on Science and Technology of Synthetic.

[33] M. Pope, H. P. Kallmann, and P. Magnante. Electroluminescence in organic crystals. *The Journal of Chemical Physics*, 38(8):2042–2043, 1963.

[34] L. Rocha. *Microstructures électroluminescentes organiques: applications à la gestion de l'émission lumineuse.* PhD thesis, Université Paris 6, 2002.

[35] M. G. Salt. *Photonic band gaps in waveguide modes of textured, metallic microcavities.* PhD thesis, University of Exeter, 1999.

[36] H. Shirakawa, E. J. Louis, A. G. MacDiarmid, C. K. Chiang, and A. J. Heeger. Synthesis of electrically conducting organic polymers: halogen derivatives of polyacetylene, (ch)x. *Journal of the Chemical Society, Chemical Communications*, pages 578 – 580, 1977.

[37] B. W. Shore, M. D. Perry, J. A. Britten, R. D. Boyd, M. D. Feit, H. T. Nguyen, R. Chow, G. E. Loomis, and L. Li. Design of high-efficiency dielectric reflection gratings. *Journal of the Optical Society of America A: Optics, Image Science, and Vision*, 14(5):1124–1136, 1997.

[38] J. Stehr, J. Crewett, F. Schindler, R. Sperling, G. von Plessen, U. Lemmer, J. M. Lupton, T. A. Klar, J. Feldmann, A. W. Holleitner, M. Forster, and U. Scherf. A low threshold polymer laser based on metallic nanoparticle gratings. *Advanced Materials*, 15(20):1726–1729, 2003. 10.1002/adma.200305221.

[39] J. Sturm, S. Tasch, A. Niko, G. Leising, E. Toussaere, J. Zyss, T. C. Kowalczyk, K. D. Singer, U. Scherf, and J. Huber. Optical anisotropy in thin films of a blue electroluminescent conjugated polymer. *Thin Solid Films*, 298(1-2):138–142, 1997.

[40] O. Svelto. *Principles of Lasers.* Plenum Press, 1998.

[41] C. W. Tang and S. A. VanSlyke. Organic electroluminescent diodes. *Applied Physics Letters*, 51(12):913–915, 1987.

[42] G. Tayeb, B. Gralak, and S. Enoch. Structural colors in nature and butterfly-wing modeling. *Optics & Photonics News*, 14(2):38–43, 2003.

[43] J. M. Teijido. *Conception and design of illumination light pipes*. PhD thesis, University of Neuchâtel, 2000.

[44] J. Turunen. *Micro-Optics*, chapter 2: Diffraction theory of microrelief gratings, pages 31–52. Francis & Taylor, New York, 1997.

[45] P. S. Vincett, W. A. Barlow, R. A. Hann, and G. G. Roberts. Electrical conduction and low voltage blue electroluminescence in vacuum-deposited organic films. *Thin Solid Films*, 94(2):171–183, 1982.

[46] X. H. Wang, M. Grell, P. A. Lane, and D. D. C. Bradley. Determination of the linear optical constants of poly(9,9-dioctylfluorene). *Synthetic Metals*, 119(1-3):535–536, 2001.

[47] C. Weiteneder. *Nanostructuring of surfaces for optical and visual security applications using lithography techniques*. PhD thesis, University of Neuchâtel, 2006.

[48] A. Yariv and P. Yeh. *Optical Waves in Crystals*. Wiley, 1984.

[49] A. Yariv and P. Yeh. *Photonics*. Wiley, 2007.

[50] P. Yeh. *Optical waves in layered media*. Wiley, 1998.